Theoretical Study of Voltage-driven Capture and Translocation Through a Nanopore: From Particles to Long Flexible Polymers

Le Qiao

Thesis submitted to the University of Ottawa
In partial fulfillment of the requirements
for the Ph.D. degree in Physics

Ottawa-Carleton Institute of Physics
Department of Physics
Faculty of Science
University of Ottawa

Summary

Voltage-driven translocation, the core concept of nanopore sensing for biomolecules, has been extensively studied *in silico* and *in vitro* over the past two decades. However, the theories of analyte capture are still not complete due to the complex dynamics resulting from the coupling of multiple physical processes such as diffusion, electrophoresis, and electroosmotic flow.

In this thesis, I build and design translocation simulations for analytes ranging from point-like particles to rod-like molecules and long flexible polymers. The primary goal is to test, clarify and complete the existing capture theories. For example, we revisit and revise the existing definitions of the capture radius, clarify the concept of depletion zones, and investigate the impacts of the flat field near the pore.

Earlier theories of translocation underestimate the importance of the electric field outside the nanopore. In our work, we analyze the non-equilibrium dynamics during the capture process originating from the converging field lines, *i.e.*, rod orientation and polymer deformation. We characterize the rod orientation and quantify its impact on capture time both with and without Electrohydrodynamic interactions. We investigate the polymer chain deformation and calculate the translocation time by taking the electric field outside the nanopore into account as opposed to the conventional simulation approaches.

Besides nanopore sensing, there are many undiscovered possibilities for nanopore translocation technologies. We test two proof-of-concept ideas in which we suggest to use capture and translocation to separate molecules of different physical properties. For example, we show how one could selectively capture particles sharing the same mobility but different diffusion coefficients using a pulsed field. Moreover, we demonstrate that it is possible to build a ratchet using pulsed fields and a nanopore to change the concentration ratios of a polymer mixture of different sized polyelectrolytes.

Résumé

Le concept de translocation dirigée par une tension électrique pour la détection de biomolécules à travers des nanopores été largement étudié, tant in silico que in vitro, au cours des deux dernières décennies.

Cependant, les théories sur la capture des analytes ne sont toujours pas complètes en raison de la dynamique complexe qui résulte du couplage entre de multiples processus physiques tels que la diffusion, l'électrophorèse, l'EOF, etc. Lors de cette thèse, j'ai construit et conçu des simulations reproduisant la translocation d'analytes comme des particules ponctuelles, des molécules en forme de bâtonnets ainsi que des polymères longs et flexibles. L'objectif principal est de tester, de clarifier et de compléter les théories de capture existantes. Par exemple, nous avons revisité et revu les définitions existantes du rayon de capture, clarifié le concept de zones de déplétion, et étudié les impacts du champ électrique près du pore.

Les théories antérieures sur la translocation sous-estiment l'importance du champ tension électrique en dehors du nanopore. Dans nos travaux, nous avons analysé la dynamique hors-équilibre, provenant des lignes de champ convergentes, lors du processus de capture, c'est-à-dire l'orientation des bâtonnets et la déformation du polymère. Nous avons caractérisé l'orientation des bâtonnets et quantifié son impact sur le temps de capture à la fois avec et sans les interactions électro-hydrodynamiques. Nous avons étudié la déformation de la chaîne de polymères et calculer le temps de translocation en prenant en compte le champ électrique à l'extérieur du nanopore contrairement aux approches de simulation classiques.

Outre la détection, il existe de nombreuses possibilités encore non découvertes pour les technologies de translocation utilisant des nanopores. Nous avons testé deux idées conceptuelles, utilisant la capture et la translocation, et permettant de séparer des molécules ayant propriétés physiques différentes. Par exemple, nous avons montré comment capturer sélectivement des particules partageant la même mobilité mais ayant des coefficients de diffusion différents en utilisant un champ pulsé. De plus, nous avons démontré qu'il est possible de construire un rochet utilisant des champs pulsés et un nanopore pour modifier les rapports de concentration d'un mélange de polyélectrolytes de différentes tailles.

Statement of Originality

I hereby declare the work presented in this thesis is new and original to the best of my knowledge. These are the research outcomes from my PhD training under the supervision of Prof. Gary Slater. This thesis includes three papers published in peer-reviewed journals (Chapters 4, 5 and 6), one under review (Chapter 8) and two manuscripts to be submitted soon (Chapter 7 and Appendix A).

As the first author of all six articles, all the simulation results in Chapters 4 - 8 in Sec. III of Appendix A were generated by me. I also did all the data analysis (except Appendix A Sec. IV), most of the theoretical analysis, and the writing of the manuscripts. My supervisor also substantially contributed to the thesis in many different ways including developing the theoretical ideas, providing insightful suggestions on data analysis and constructing the manuscripts, as well as revising and improving the writing.

Maxime Ignacio, as the second author of the paper in Chapter 5, invented the 1D Kinetic Monte Carlo (KMC) simulation algorithm and wrote the first version of the Python scripts for the Monte Carlo simulations. He also contributed to some of the theoretical calculations. In Chapter 4, he helped me set up the simulations and was involved in developing the initial ideas. Appendix A presents the results from a project that I took over from him when he moved to Paris. He drafted the initial manuscripts. Later on, we changed the focus of the project to propose a novel parameterized fitting function that Gary Slater designed to characterize anomalous diffusion. I carried out the simulations for the diffusion of the colloidal particle between two walls and rewrote the manuscript. We also added Sec. VI to show Monte Carlo results generated by Nicholas Ilow. All Python scripts for Langevin Dynamic (LD) and Lattice Boltzmann (LB) simulations presented in this thesis were written by me and simulated using the ESPResSo package.

Acknowledgements

Firstly and foremost, I would like to express my deepest appreciation to my supervisor, Prof. Gary Slater, who opened a new door and steered me through my PhD. This thesis would have never been accomplished without his unwavering supports, helpful advice, and full involvement in every step of my doctoral training. As a tyro in academia, I'm deeply influenced by his professional work, enthusiasm for research, and optimistic attitude towards life. Moreover, He guided me to think critically and inspired me with new ideas via his extensive knowledge and invaluable insights in the field.

I would also like to extend my gratitude to my colleagues in Gary's research group. Maxime for helping me initiate my research and translating my thesis summary to french. He is a superb collaborator in work and a trustworthy friend in life ; David for invaluable discussions ; Mehran for useful advice on living in Canada as an international student ; Hanyang for being a good lunch mate ; Neo for sharing all the funny stories ; Nick for collaborating on our joint manuscript.

Of course, my PhD study would not have been possible without the generous support from the China Scholarship Council (CSC) and the University Ottawa. I also gratefully acknowledge Gary for providing me the opportunity to attend the conferences and workshops ; Mitacs for supporting my visit to Prof. Christian Holm's group at the University of Stuttgart in Germany. Thanks to Prof. Christian Holm and Kai Zsuttor for the invaluable discussions and help during my stay.

I'm extremely grateful to my family for supporting every decision that I make, non of this would have been possible without their love and support. Last but not least, thanks should also go to all my friends who accompanied me through the good and bad days during my PhD. Thank you Wei and Yuanming for hunting tasty and authentic Chinese food with me ; Lijuan and Zichao for tolerating me being mean sometimes ; Zhengyi for being a good listener ; Guanlong for being the best tennis partner who does not beat me too often ; my roommates Haiyang and Kaiyi for not murdering each other (and me) during the quarantine in the past year ; Kun for the occasional tasty treats ; Yuan and Bingxin for hosting the dinner parties and game nights ; and all others who added joy to my life in Ottawa.

List of Abbreviations

α-HL	α-hemolysin
cis	*This side of* the nanopore where the analyte resides prior to translocation
trans	*The other side of* the nanopore where the analyte resides after translocation
ABC	Absorbing Boundary Conditions
bp	basepair
CM	Centre of Mass
dsDNA	double-stranded DNA
DPD	Dissipative Particle Dynamics
D3Q19	Three-dimensional 19 Velocity lattice models
DispD	Displacement Distribution function
EOF	Electro-Osmotic Flow
EHI	Electro-Hydrodynamic Interactions
EAF	Exact Axial Field
FENE	Finitely-Extensible-Nonlinear-Elastic
GPU	Graphics Processing Unit
KMC	Kinetic Monte Carlo
LD	Langevin Dynamic
LB	Lattice Boltzmann
LBM	Lattice Boltzmann method
LMC	Lattice Monte Carlo
LJ	Lennard-Jones potential
mRNA	messenger RNA
MspA	Mycobacterium smegmatis porin A
MSD	Mean-Square Displacement

MD	Molecular Dynamics
MC	Monte Carlo
MFPT	Mean First Passage Time
Pe	Péclet number
PCF	Point-Charge Field
P^3M	Particle-Particle-Particle-Mesh algorithm
RBC	Reflecting Boundary Conditions
SBC	Source Boundary Conditions
SRD	Stochastic Rotation Dynamics
ssDNA	single-stranded DNA
TP	Tension Propagation theory
TMV	Tobacco Mosaic Virus
WCA	Weeks-Chandler-Andersen potential
ZIFE	Zero-Integrated-Field Electrophoresis

List of Symbols

σ	effective size of a "soft" bead defined by Lennard-Jones potential ; basic unit of length for Langevin Dynamic and Lattice Boltzmann simulations
ρ	capture rate ; mass density (Chapter 3)
Θ	order parameter
Θ_E	order parameter for rod orientation with respect to the local field direction
Θ_z	order parameter for rod orientation with respect to the nanochannel axis
δ	Dirac delta function
γ	friction coefficient
ϵ	minimum energy of the Lennard-Jones potential ; basic unit of energy for Langevin Dynamic and Lattice Boltzmann simulations
ε_o	vacuum permittivity
ε_r	relative permittivity
Φ_o	electrostatic potential at a charged surface
Φ	mean field intensity (Chapter 8)
ψ_o	electrostatic energy across the nanopore system
ψ_θ	rotational electrostatic energy
ν	Flory exponent
η	fluid viscosity
μ	electrophoretic mobility
μ_l	electrophoretic mobility of the particle in the $\underline{\text{l}}$arge particle limit (Hückel limit)

μ_s	electrophoretic mobility of the particle in the small particle limit (Smoluchowski limit)
μ_e	electrophoretic mobility of the raspberry rod (Chapter 7)
μ_m	mechanical drift mobility of the raspberry rod (Chapter 7)
μ_i	i^{th} central moment of the displacement distribution function (Appendix A)
λ_e	capture radius
λ_D	Debye length
Π	stress tensor
b	bond length
b_k	effective size of a Kuhn segment
C_s	salt concentration
C_s^o	salt concentration in the bulk
C_{cis}	salt concentration on the *cis* side of the nanopore
C_{tr}	salt concentration on the *trans* side of the nanopore
C	analyte concentration
C_o	analyte concentration in the bulk
d	diameter of the rod (Chapter 7)
D	diffusion coefficient
$D_\parallel$	parallel diffusion coefficient
$D_\perp$	perpendicular diffusion coefficient
D_r	centre-of-mass diffusion coefficient for a *Rouse* polymer
D_z	centre-of-mass diffusion coefficient for a *Zimm* polymer
E_p	electric field inside the nanopore
$\boldsymbol{h}$	end-to-end vector
h	end-to-end distance
K	collision operator (Chapter 3) ; Kurtosis (Appendix A)
k_B	Boltzmann constant
ℓ_p	pore (or channel) length
ℓ_B	Bjerrum length
L	length of the rod (Chapter 6 & 7)
L_c	contour length of a polymer
L_c^*	minimal length of a polymer for which we must consider excluded volume interactions

L_p	persistence length
m	mass
N_k	number of Kuhn segments
N_t	number of monomers that have passed the mid-point of the channel (Chapter 8)
Q_{eff}, $\tilde{Q}$	effective charge
$\boldsymbol{r_m}$	position of the centre of mass vector
r_p	pore radius
r_d	depletion radius
r_e	electrostatic length for the given pore geometry
R_H	hydrodynamics radius
R_g	radius of gyration
R_{go}	equilibrium radius of gyration of a polymer in free solution
R_{ge}	radius of gyration of a polymer in the drift-dominated regime
R_{gc}	radius of gyration of a polymer when one end enters the nanopore
R^*	capture radius (Chapter 4)
R_θ	orientational capture radius
$R^*_{1/2}$	capture radius defined as the location where the probability of capture is 1/2
R^*_i	capture radius defined as the mean escape distance when the polarity is inverted
R^*_{cap}	capture radius defined using the time dependent capture rate
R^*_{90}	capture radius defined as the width of the depletion zone where the concentration is 90% of that in the bulk
R_b	radial distance between the outer boundary and the pore centre (Chapter 5) ; radial distance between the outer reflecting boundary and the pore centre (Chapter 4)
R_r	radial distance between the outer reservoir-like boundary and the pore centre (Chapter 4)

R_p	radial distance of the inner absorbing boundary (Chapter 5)
$\boldsymbol{R}$	random noise
τ_o	basic unit of time
τ_p	time needed to empty a zone of radius r_p (Chapter 4)
t_d	depletion time, time needed to empty a zone of radius r_d (Chapter 5)
τ_λ	time needed to empty a zone of radius λ_e (Chapter 4)
$t_\leftarrow$	backward-pulse duration
$t_\rightarrow$	forward-pulse duration
$t_\emptyset$	zero-pulse duration (Chapter 5)
t_c	capture time (Chapter 7)
t_t	translocation time (Chapter 7)
t_e	escape time (Chapter 7)
$\overline{\tau}$	mean DC translocation time (Chapter 8)
$\tau_\Rightarrow$	increment of the forward pulse duration (Chapter 8)
T	temperature
U_{ev}	energy contribution of the excluded volume interactions
U_F	free energy of an ideal chain
U_e	electrostatic potential energy (Chapter 5)
U_v	virtual entropic potential (Chapter 5)
U_E	external potential
U_{WCA}	Weeks-Chandler-Andersen potential
U_{Bend}	angular harmonic potential
U_{FENE}	finitely-extensible-nonlinear-elastic harmonic potential
ΔV	potential difference across the nanopore system
δV	potential drop from infinity to the nanopore entrance

Table of Contents

1

Introduction

Polymer translocation plays a crucial role in a wide variety of biological processes such as mRNA transport through a nuclear pore or a virus being injected into a cell. In the past two decades, the concept has been used in nanopore sensing to detect, recognize, verify, qualify or sequence biomolecules such as DNA/RNA, proteins, and other polyelectrolytes [**?**, 1–9]. In general, as shown in Fig 1.1, translocation usually features a nanometer-sized hole in a solid-state wall or a biological membrane that separates the system into two chambers. The analytes are placed on one side of the chamber and an electric potential is applied across the system via two electrodes to transport the analytes through the hole. This process is called translocation, during which molecules displace the solvent and block the ionic exchange through the hole. The resulting current blockages are measurable and their signatures are congruent with the properties of the analyte such as size, structure, concentration, and so on. Compared to conventional approaches, nanopore sensing is fast and inexpensive. The electric-based label-free translocation enables detection without any modification to the molecule. Moreover, single-molecule translocation allows one to focus on the properties of an individual molecule, rather than the averaged behavior of a molecular population.

At the time I started my PhD in 2016, my supervisor proposed to me several potential projects about translocation and capture. I was immediately intrigued by the simple but brilliant idea and excited by the latest progress in the field. Upon that time, most of the research efforts were spent understanding the translocation process. During the capture process (Stages I and II in fig 1.1), the charged polymers need first to diffuse into the region where the strength of the electric field is strong enough to attract them towards the nanopore entrance, and finally, one end of the polymer needs to find the pore. The dynamics of the polymers are governed by multiple coupled physical quantities such as the

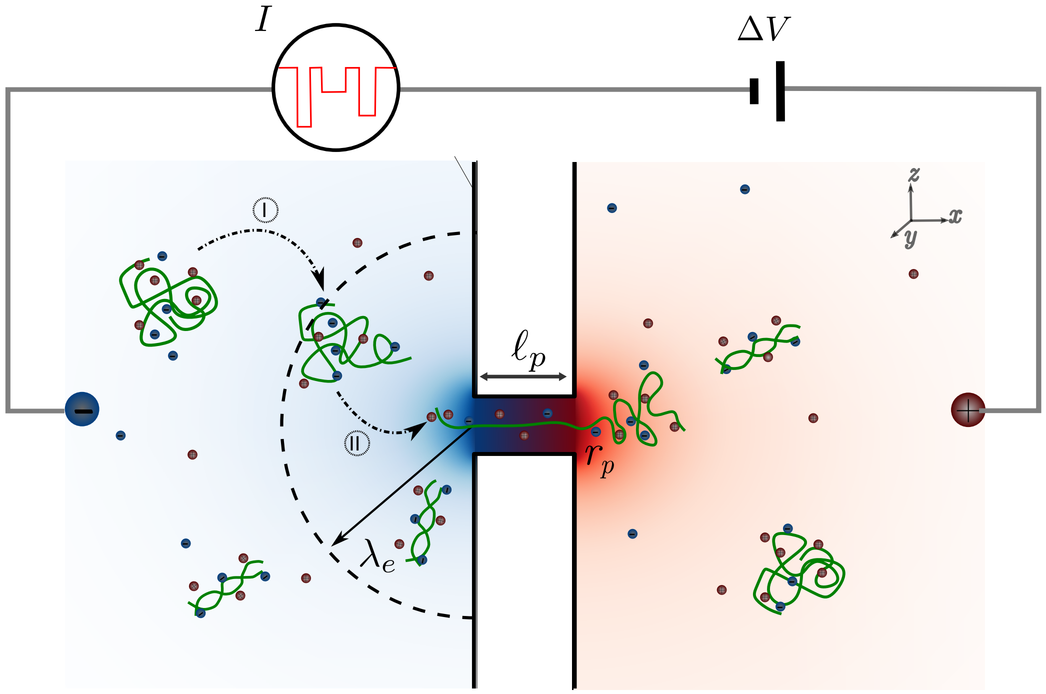

FIGURE 1.1 – Schematic plot of a voltage-driven translocation setup. Two types of molecules are shown here in green color as examples ; the surrounding charged particles are counterions (red) and coions (blue). The background colors code for the electric field strength, the darker the higher the strength. The curved line depicts the capture radius λ_e. The arc arrows indicate two stages during capture : I Analytes diffusion towards the capture radius ; II Field-driven drift towards the nanopore. ℓ_p and r_p are the length and radius of the nanopore.

electric field, diffusion, electrophoretic drift, concentration, charge, Electroosmotic flow, interaction with the nanopore and the membrane, etc, which is non-trivial and not completely understood. Therefore, we decided to focus my work on understanding the capture process using theoretical analysis and "computer experiments". This thesis will be presented as a collation of published peer-review journal articles or ongoing manuscripts of my works. Before getting into the specific research topics in later chapters, it is necessary to first present a short review of the development of nanopore sensing using translocation in the past two decades. But to avoid repetition with the more detailed and topic-specific sub-introductions in the various results chapters, this Introduction focuses on summarizing key concepts related to my work and providing a general idea of my research progress. Detailed physical description of polymer models and simulation methods will be presented in the following two Chapters.

1.1 History of nanopore translocation

Voltage-driven translocation was initially used for counting and sizing blood cells, nanoparticles, and viruses [9]. The idea of using a nanopore to sequence a single-stranded DNA molecule (ssDNA) first emerged in the 1980s [10] and then a series experiments were conducted in 1990s to test the proof-of-concept idea [11–14]. The success in determining the length and in distinguishing RNA from ssDNA using biological pores stimulated intense research on translocation. The first nucleobase-level resolution was achieved in 2007, but the ssDNA had to be kept immobile in a α-HL nanopore [15]. This is because the translocation rate driven by electric forces is too fast for nucleobase resolution detection. To slow down the translocation, Manrao *et al.* [16] bound a blocking oligomer to the DNA template and unzipped it while transporting DNA through the nanopore. By using this technique and a mutated MspA pore, they were able to successfully identify the sequence of a ssDNA from the current recorded during the translocation.

Meanwhile, the rapid development of advanced nanopore fabrication technologies enabled the use of artificial solid-state nanopores. Compared to biological pores, the sizes of the solid-state nanopores are more adjustable, and they have more stable mechanical, chemical, and thermal properties [5]. The use of solid-state nanopore accelerated the research progress in DNA sequencing using translocation.

However, other than the high translocation rate, there are still other challenges that need to be overcome to commercialize this tool for sequencing. For example, the wide conformation fluctuations induce a very broad translocation time distribution, and the capture and threading of exceptionally long molecules through individual pores is still technically challenging. Beyond the sequencing applications, new ideas are continuously proposed to use translocation for other sensing purposes such as biological screening, medical diagnosis, protein profiling [**?**, 6, 7, 17–19]. In particular, the detection and analysis of small molecules such as ions, biomarkers, aptamers, RNA, virus, or protein fragments has become another hot topic [3].

On the theoretical end, theoretical modeling provides an efficient and more controlled way to study translocation dynamics in different regimes. Besides, cheaper and more powerful computers enable simulations as a third approach in addition to theoretical analysis and experimental research. Muthukumar's book on translocation offers a good introduction to the physical background and summarizes important concepts regarding polymer translocation [20]. Earlier theoretical works focused on finding the scaling law of the translocation time *vs* polymer chain length : key results are described in several review papers [21, 22]. The translocation process is not the focus of this thesis, but the tension propagation (TP) theory has to be highlighted here because it unifies the results for the translocation time scaling law [23–26]. The key concept is that the translocation of a polymer chain is a process of tension propagation from the captured end to the free end along the conformation of the chain. As a result, the translocation time is determined by the initial conformation and the friction in the nanopore. The initially random conformations leads to a broad translocation time distribution.

1.2 Capture theory

The capture process, on the other hand, is difficult to study directly from experiments as the capture is not observed until the polymer enters the nanopore [27]. The most approachable measurement for capture is the capture rate which is defined as the inverse of the average time intervals between two successive events. The capture rates measured from α-HL pore under a weak bias were found to be exponentially dependent on the applied voltage [28] because a free energy barrier needs to be overcome to translocate through the narrow nanopore. The capture rate is simply a function of the Boltzmann factor of the difference between the applied electrostatic energy and the barrier height $\rho \sim \exp[(q\Delta V - U)/k_BT]$.

Nakane *et al.* [29] simulated the capture of DNA molecules by a cylindrical pore using Monte Carlo simulations and found the dependence of the capture rate on the applied electric potential is exponential at low field but linear at high field. They derived a theoretical prediction for the capture rate using the concept of a capture radius, which is defined as the minimum radial distance $\lambda_e(\Delta V)$, at which analytes can still escape from capture with an applied voltage ΔV. Note : I convert their notations to ours for readability reasons. At high field, the capture rate can be simply estimated as the diffusion-limited absorption rate for an absorbing hemisphere at the capture radius [30], which gives

$$\rho = 2\pi C_o D \lambda_e, \tag{1.1}$$

where C_o is the concentration of the analyte in free solution. The capture radius $\lambda_e = \frac{r_p^2}{\ell_p + 2r_p} \times \frac{\Delta V}{4D}$ is estimated by balancing the diffusion velocity $2D/r$ and the electrophoretic velocity μE at the capture radius. Here μ is the mobility of the analyte, D is its diffusion coefficient and the electric field is from a rough estimation of the electric field from a thin charged disc : for distances $r > 2r_p$,

$$E \approx \frac{\Delta V}{\ell_p + 2r_p} \times \frac{r_p^2}{2r^2} \tag{1.2}$$

which gives the linear dependence on ΔV. At weak field, the absorber is simply the pore entrance and the capture rate is $\rho \approx P(\Delta V) \times 4CDr_p$ where the probability for a molecule to overcome the entropic barrier, $P(\Delta V)$, is an exponential function of the voltage ΔV.

The linear dependence of the capture rate on voltage was later verified by Chen *et al.* [31] from an experimental measurement of the translocation of λ DNA through a solid-state nanopore under a micro-volt bias. They claimed to observe a micrometer-sized depletion zone near the pore from the snapshot picture of fluorescent DNA translocation. Using the measured capture rate they estimated the capture radius to be roughly the same size as the depletion region, and thus attributed the depletion region to the attractive electric field outside the nanopore.

Wong *et al.* [32] later revisited the problem with analytical calculations and provided an alternative explanation for the depletion of long polymers near the nanopore that Chen *et al.* observed. They assumed the electric field outside the pore is screened and ascribed the depletion near the pore to the electroosmotic flow (EOF) of counterions induced by the positively charged nanopore. Their calculations gave a depletion region roughly the size of the radius gyration of the polymer.

Chou [33] analytically solved the steady-state electrokinetic equations for the capture of charged particles by nanopores in the presence of the external electric potential and salt gradients. They pointed out that the details of the electric field outside the pore plays a key role in analyte capture. The salt gradients increase the electrostatic potential locally near the pore thus can enhance the capture rate. They also illustrated that the EOF from the charged nanopore can remove particles from the nanopore rapidly thus enhance the analyte capture rate in certain salt conditions.

Wanunu *et al.* [34] experimentally investigated the dependence of capture rates on polymer chain length and applied potential for the capture of a dsDNA into a solid-state nanopore. They derived a point-charge approximation for the electric field outside the nanopore (Fig 1.2a), $V(r) = (r_p^2/2\ell_p r)\Delta V$, and stated that the transport of the analytes toward nanopore is primarily determined by diffusion and electrophoresis. The authors defined the capture radius as the crossover between the diffusion-dominated and drift-dominated zones, which is equivalent to Nakane's definition except for a slightly different electric field approximation. They stated that for long DNAs ($> 8\,kbp$), the capture rate is dominated by the field and thus is independent of the DNA length. Otherwise, for shorter chains, the capture rate is limited by the entropic barrier. The capture rate ρ increases with the length of the DNA and has an exponential dependence on the applied voltage. They also showed that asymmetric salt concentrations on the two sides of the nanopore (C_{cis} and C_{tr}) can enhance the electric field outside the pore. As a result, the capture radius is expanded to $\lambda_e' = \lambda_e \frac{C_{tr}}{C_{cis}}$. They demonstrated that this approach can effectively increase the capture rate while maintaining the same translocation times.

Muthukumar [35] developed a general theory to describe the capture rate by incorporating both the barrier regime and the drift regime into one expression. His theory was able to recover the experimentally observed electric field and chain length-dependent capture rates in the barrier-limited regime, and the chain length independent yet electric field dependent capture rates in the field-dominated drift regime. He added the energy barrier gain from the process of the polymer chain end finding the nanopore from a coiled state in his calculation, which was missing in previous calculations. However, the capture rate is derived based on the 1D Smoluchowski equation, thus the pore size did not appear in the result. The contribution of the electric field outside the nanopore was also neglected.

Meanwhile, Grosberg *et al.* [36] focused on understanding the roles of diffusion and electrophoresis in the capture process for the translocation of DNA or other polyelectrolytes. They showed that electrophoretic mobility is not a direct result of the chemical charge on DNA. Instead, it depends on the effective charge, which can be estimated from the electrophoretic mobilities via $Q_{eff} = \frac{\mu k_B T}{D}$ using the concept of the stall force. They were able to simplify the electrophoresis of DNA to a point-like particle drift with an effective charge. Then they solved the steady-state concentration profile of DNA outside the nanopore from the generalized Smoluchowski equation. They also offered an alternative way to define the capture radius as the distance from which the time for the DNA to travel to the nanopore by sole diffusion is equal to that due to the electric field alone. The capture rate predicted by them agrees with previous experimental results.

The capture rate is influenced by numerous effects in real life experiments [37]. Subsequent research on capture has focused on refining previous theories to match experimental results by considering different experimental settings. For example, the electrohydrodynamic coupling for rod like or coil-like DNA near the nanopore [38], the electrostatic interactions between the polyelectrolyte and the nanopore [39, 40], the entropic barrier to enter the pore [41], the salt concentration [42], the osmotic pressure [43], the EOF [44, 45] and dielectrophoresis [46].

1.3 The Electric field

It is also worth mentioning that many of the previous theories treat the nanopore as a point charge and thus the electric field outside is from a point-charge field (PCF) approximation [27, 31, 34, 36, 41, 47]. Unifying all the descriptions in our notations, the electric potential outside a nanopore of radius r_p then is given by

$$V(r) = \frac{2r_p}{\pi r}\delta V = \Delta V \frac{r_e}{r}, \tag{1.3}$$

where $r_e = r_p/(\frac{2\ell_p}{r_p} + \pi)$ is an electrostatic length defined from the pore geometry and δV is the potential drop from infinity to the nanopore entrance. This gives a spherically symmetric electric field as shown Fig 1.2a,

$$\boldsymbol{E}(r) = -\Delta V \frac{r_e}{r^2}\ \hat{\boldsymbol{r}}. \tag{1.4}$$

The PCF approximation is nonphysical when $r \to 0$ as all the field lines converge to one point the magnitude diverges.

Farahpour *et al.* [48] provided an alternative form of the electric field outside the pore by solving Laplace's equation in oblate spherical coordinates based on the work done by Kowalczyk *et al.* [49] ; this gives

$$V(\zeta, \beta, \phi) = \Delta V \frac{r_e}{r_p} \arctan\left[\sinh(\zeta)\right], \tag{1.5}$$

where $\zeta \in (-\infty, +\infty)$, $\beta \in [0, \pi]$ and $\phi \in [0, 2\pi]$. The potential only depends on the oblate distance ζ (here in units of r_p). The corresponding electric field is given by

$$\boldsymbol{E}(\zeta, \beta) = -\frac{\Delta V r_e}{r_p^2 \cosh\zeta \sqrt{\sinh^2\zeta + \sin^2\beta}}\,\hat{\boldsymbol{\zeta}}, \tag{1.6}$$

as shown in Fig 1.2b. Combining the outside field with a piece-wise uniform field inside a cylinder, they were able to study the full process of capture and translocation of a polymer through a nanopore using a hybrid lattice Boltzmann-Molecular Dynamics simulation approach. They observed an extension of the polymer chain conformation due to the electric field gradient near the nanopore before the capture, and a compression after translocation. They also concluded that the electric field outside the pore helps the polymer chain end to find the nanopore.

Vollmer *et al.* [50] investigated the capture and translocation of a flexible polymer

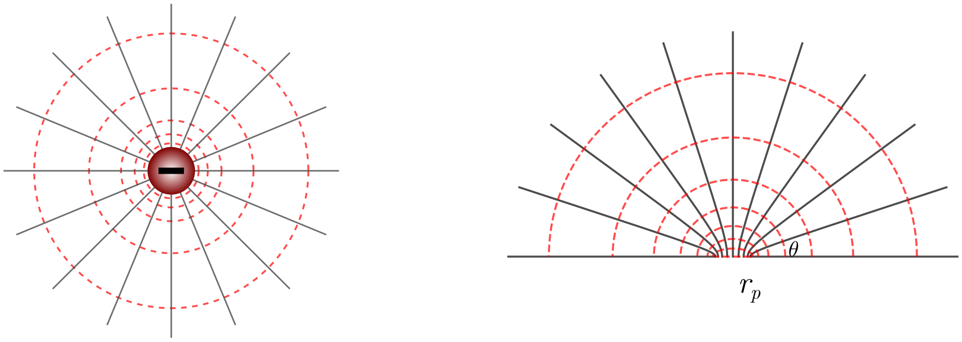

(a) Point charge field (PCF)

(b) Exact field

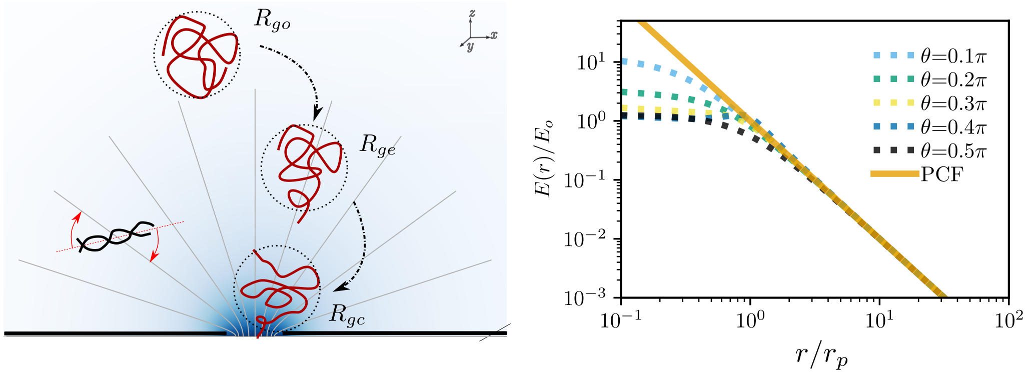

(c) Deformation & Orientation

(d) PCF *vs* Exact Field

FIGURE 1.2 – (a - b) Electric field lines and equal potential contour plots for the Point-charge field (PCF) approximation and the Exact field solved analytically ; θ is the angle between the field lines and the wall, r_p is the radius of the nanopore (c) Schematic plot of the capture of a rod-like dsDNA and of flexible polymers. $R_{go} \neq R_{ge} \neq R_{gc}$ are the radii of gyration of the flexible polymers in the diffusion-dominate zone, drift-dominated zone, and when one end enters the pore. (d) Comparison between the PCF *vs* the Exact field for different radial distances and various angles. The y-axis is scaled by the plateau value $E_o = E_{PCF}(r_p)$.

through a nanopore including electric field given by eq. 1.6 in their Langevin Dynamic (LD) simulations. They showed that the polymer chain can be either elongated, as seen by Farahpour *et al.*, or compressed, depending on the competition between diffusion and drift. They adjusted the balance by changing the temperature in the LD thermostat. For higher temperature simulations, the energy barrier at the nanopore is high, thus the polymer chain is compressed while trying to enter the nanopore ; otherwise, for lower temperatures, the electric forces dominates the capture and the field gradient stretches the polymer chain. In conclusion, the non-equilibrium conformations impacted the translocation time.

1.4 Thesis rationale

Despite the previous theories and simulations of the capture process, several questions remain. The concept of a capture radius is still ill-defined. All the existing definitions give the same length but the approximations are fairly rough. More importantly, although the nanopore is the target, its size is not included in those calculations. On the other hand, the depletion zone is experimentally reported [31] to have the same size as the capture radius, but it is rarely found in theoretical studies.

Furthermore, the PCF approximation is used in most of the existing theories. When you compare it with the exact field as shown Fig 1.2d, the two fields converge at large distances, however, at short distances, the exact field saturates toward a uniform field inside the pore, while the PCF diverges. Furthermore, the exact field presents an angular dependence near the pore ($\sim 3\,r_p$). The field strength is higher near the pore edge for small angles. Does this play a role in the capture process ? Also, the converging field lines generate a gradient $\nabla E \sim 1/r^3$. One would expect orientations for rod-like stiff molecules as well as deformations for flexible polymers when they are in the high field region shown in Fig 1.2d. Those nonequilibrium components are often not considered in previous theories.

Lastly, current applications of polymer translocation mainly focus on sensing purposes. Can we come up with new ideas and design a translocation system to serve another purpose such as polymer separation (purification) ?

1.5 Thesis Overview

Computer simulations have many advantages for the study of the capture process. They allow us to test the impact of certain theoretical approximations on a wide range of time and length scales. However, in typical translocation experiments, the capture of analytes can't be observed until they enter the nanopore, let alone observing polymer conformations and dynamics. Moreover, faster computer simulation techniques and more accurate simulation models enable us to efficiently test new proof-of-concept ideas at a low cost.

My PhD work is devoted to understanding the capture and translocation of analytes driven by an electric field using theoretical analysis and computer simulations. The investigations start with the capture of point-like particles, followed by rod-like molecules and eventually long semiflexible polymers. The final goal of this thesis is to provide insights into analytes capture and translocation. Following this general Introduction, a brief background of polymer physics and simulation techniques is given in Chapter 2 and 3. Those are tailored for readers not in, or new to, the field, to have quick access to essential information to understand the results and discussions in the results chapters.

Chapter 4 focuses on understanding how diffusion and electrophoretic drift coexist during the capture of point-like particles. We revisit the previous definitions for the capture radius and clarify some aspects of capture theory. We revise previous definitions and provide alternative ways of defining the capture radius using analytical calculations and Lattice Monte Carlo simulations. In Chapter 5, we present a new Kinetic Monte Carlo simulation algorithm to simulate the capture by mapping the 3D system onto a 1D lattice system. We compare the capture of particles under the exact field and PCF approximation. We also test a proof-of-concept idea for selectively capturing particle by using pulsed-fields.

Chapter 6 investigates the capture of a stiff rod-like polymer using LD simulations, especially the orientational effects. We define an orientational capture radius to characterize the orientation and qualify its effect on capture. In Chapter 7, we add Electrohydrodynamic to the simulations by coupling LD simulations to a Lattice Boltzmann fluid to recover the correct rod dynamics during capture. We also investigate the impacts of hydrodynamic interactions and charge screening on orientation and capture for a rod with different charge distributions.

In Chapter 8, we investigate field-induced conformational changes during the capture of semiflexible polymers using LD simulations. The impacts of the electric field outside the nanopore and of chain deformation on translocation times are also examined by comparing different simulation protocols. Most interestingly, we test the novel idea of building a low pass filter using a nanopore and a pulsed-field to selectively translocate polymers.

Chapter 9 summarizes the results from previous chapters and offers a more general discussion and some ideas for future work. Appendix A is a manuscript written in collaboration with others. It proposes an empirical method to characterize and parametrize anomalous diffusion, which is not directly related to the main theme of my thesis.

2

Background

Polymers have been playing a crucial role in our life since the early days of mankind. From naturally occurring polymers such as proteins, starch, and rubber, to synthetic polymers such as polyethylene, Teflon, and nylon, the fields of polymer research in life science and synthetic polymeric materials in industry have been thriving since the early twentieth century. This chapter covers the fundamental theories of polymer physics from polymer structures to polymer dynamics. The goal is to provide readers sufficient background information to understand the dynamics of polymer translocation and grasp the core concept of how I construct the polymer models for my simulations in later chapters. Of course in the context of nanopore sensing, our attention here is primarily on showing the physics of a single polymer chain and its dynamics in a dilute solution.

2.1 Polymer Physics

Poly-mers literally refer to molecules consisting of *many* identical *parts* connected by chemical bonds. The repeating basic units are called *monomers*, the process to form a polymer structure from N monomers is called *polymerization*, and N is called *degree of polymerization*. Polymers fall into different categories depending on their physical properties. For example, based on their architecture, polymers can be linear, cross-linked, branched, or ring-shaped. There are also copolymers made of more than one type of monomer with different orders (*e.g.* copolymers -A-B-A-B-).

In physics, coarse-grained polymer models are often used to predict the physical quantities of interests for different times and length scales, thus neglecting the detailed local chemical structure. Similar to what most polymer textbooks do, I will start with the simple ideal chain model.

2.1.1 Ideal chain (freely jointed chain)

Consider a single linear polymer of $N+1$ monomers linked by N bonds of the same length b. The instantaneous shape of a polymer chain in solution is called a *conformation* (Fig. 2.1) and the maximum possible extension of the polymer chain is called *contour length*, denoted as $L_c = Nb$. The bond vector for the i-th bond is the difference between the two position vectors of adjacent monomers $\boldsymbol{R_i}$ and $\boldsymbol{R_{i-1}}$, given by

$$\boldsymbol{r_i} = \boldsymbol{R_{i+1}} - \boldsymbol{R_i}, \tag{2.1}$$

where the subscript i is an integer $\in [1, N]$. Thus the end-to-end vector is simply

$$\boldsymbol{h} = \sum_{\boldsymbol{i=0}}^{\boldsymbol{N}} \boldsymbol{r_i} = \boldsymbol{R_N} - \boldsymbol{R_0} \tag{2.2}$$

If we assume the bonds can freely rotate in space and the beads can overlap, $\boldsymbol{r_i}$ are independent of each other, and the conformation of a polymer can be treated as the trajectory of a random walker after N steps with the step size equal to the bond length b. For sufficiently large N, the probability distribution function for the end-to-end bond vector $\boldsymbol{h}$ is Gaussian. In 3D space, one has

$$\Psi(\boldsymbol{h}, N) = \left(\frac{3}{2\pi N b^2}\right)^{3/2} \exp\left(-\frac{3\boldsymbol{h^2}}{2Nb^2}\right). \tag{2.3}$$

This gives an ensemble average of the end-to-end distance $\langle \boldsymbol{h} \rangle = 0$, and the variance $\langle \boldsymbol{h^2} \rangle = Nb^2$. Instead of the instant chain conformation or contour length, the root-mean-squared end-to-end distance $h = \sqrt{\langle \boldsymbol{h^2} \rangle} = bN^{1/2}$ can be used to describe the averaged behaviour of polymer conformations : it is more useful to characterize the size of the polymer chain.

Another useful metrics to characterize the size of a polymer is the squared **radius of gyration**, defined as

$$R_g^2 = \frac{1}{N+1} \sum_{i=0}^{N} (\boldsymbol{r_i} - \boldsymbol{r_m})^2 \tag{2.4}$$

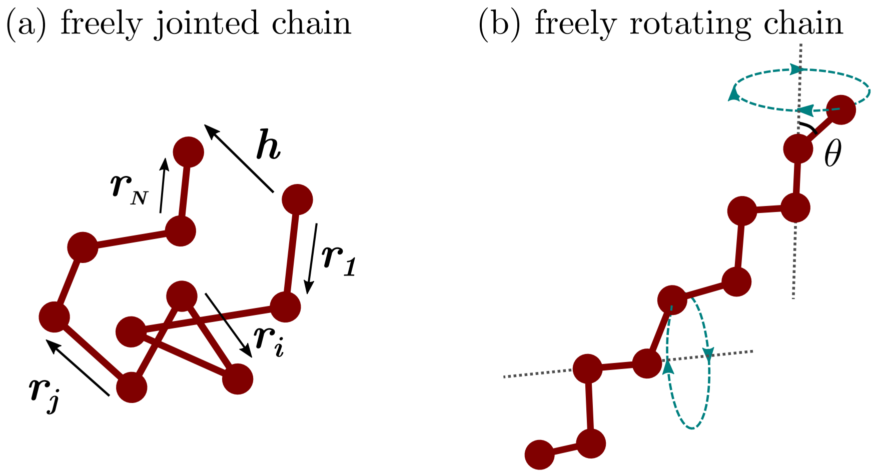

Figure 2.1 – A sketch of (a) a freely jointed chain and (b) freely rotating chain. The chain is comprised of $N+1$ beads connected by N bond vectors $\boldsymbol{r_{\{1\ldots N\}}}$, the sum of which is the end-to-end distance vector $\boldsymbol{h}$. The angle between two adjacent bonds is θ.

where $\boldsymbol{r_{cm}}$ is the position of the center of mass vector

$$\boldsymbol{r_{cm}} = \frac{1}{N+1}\sum_{i=0}^{N} \boldsymbol{R_i}. \tag{2.5}$$

The radius of gyration is sometimes preferred to characterize the chain conformation, especially when the architecture of the polymer is non-linear ; for instance, for ring or branched polymers, the end-to-end distance $\boldsymbol{h}$ is ill-defined. Another reason to choose R_g over h is that the definition of R_g considers the position of all monomers, while h depends solely on the position of two end monomers.

For an ideal linear chain, after averaging over all conformations, one gets

$$\langle R_g^2\rangle = \frac{b^2N}{6} = \frac{1}{6}\langle \boldsymbol{h^2}\rangle. \tag{2.6}$$

Please note that we assume the chain is sufficiently large that $N+1 \approx N$. Another important fact needs to be mentioned here since the name "radius of gyration" gives the impression that the shape of the chain is actually spherical. While that is certainly true if one averages over many conformations, the instantaneous shape of the conformation is more like a cigar with an aspect ratio of the three principal axes of R_g is $\approx 11.80 : 2.69 : 1$ [51].

2.1.2 Freely rotating chain

If we fix the bond angle θ but set the dihedral angle free as shown in Fig 2.1, then the freely jointed ideal chain becomes the freely rotating chain (FRC). The correlation between bonds $\boldsymbol{r_i}$ and $\boldsymbol{r_j}$ reads

$$\langle \boldsymbol{r_i} \cdot \boldsymbol{r_j} \rangle = b^2 \cos^{|j-i|} \theta = b^2 \exp\left[\frac{-b|j-i|}{L_p}\right], \tag{2.7}$$

where $L_p = -b/\ln(\cos\theta)$. The bond correlation decays rapidly with $|i-j|$. The decay length L_p is called the *persistence length*.

The mean squared end-to-end distance for the FRC now depends on the bond angle and for large N we have :

$$\langle h^2 \rangle = \frac{1+\cos(\theta)}{1-\cos(\theta)} N b^2. \tag{2.8}$$

For $\theta < \frac{\pi}{2}$, the restriction on bond angle makes the chain more stiff : as a result, $\langle \boldsymbol{h^2} \rangle > N b^2$.

2.1.3 Kratky-Porod chain

For linear polymers such as dsDNA, when $L_c \ll 100\, nm$, the rigid backbone makes the chain rod-like. Otherwise, when $L_c \gg 100\, nm$, the chain is overall flexible. In between the two regimes, the polymer is semiflexible. The famous Kratky-Porod model is used to understand the semi-rigid properties of such polymers. The idea is to constraint the bond angle of the FRC to a small value. In the limit when $\theta \to 0$, one gets

$$L_p = -\frac{b}{\ln(\cos\theta)} \approx -\frac{b}{\ln\left(1-\theta^2/2\right)} \approx \frac{2}{\theta^2} b. \tag{2.9}$$

The squared end-to-end distance can be obtained by a double integration of the bond correlation function shown in eq. 2.7, which gives [52]

$$\langle h^2 \rangle = 2 L_p L_c + 2 L_p^2 \left(\exp\left(-L_c/L_p\right) - 1\right). \tag{2.10}$$

In the long chain limit $L_p/L_c \to 0$, eq. 2.10 reduces to

$$h^2 \approx 2 L_c L_p. \tag{2.11}$$

It is natural here to introduce the concept of the Kuhn monomer, an effective monomer that contains m consecutive bond segments of length b. If we view the above polymer as a chain consisting N/m Kuhn monomers of effective size $b_k = 2L_p$, then $L_c = Nb = (N/m)b_k$ and Equation 2.11 becomes $\langle h^2 \rangle = (N/m)b_k^2$, which is simply a flexible ideal chain of $N_k = N/m$ bonds of length b_k each. This new length b_k is called the Kuhn length. In the short-chain limit, $L_c/L_p \to 0$, one simply gets $\sqrt{\langle h^2 \rangle} = L_c$: the semiflexible chain is rod-like.

Similarly, one can check the two limits for the radius of gyration,

$$R_g^2 = \frac{L_p L_c}{3} - L_p^2 + 2\frac{l_p^3}{L_c}\left(1 - \frac{L_p}{L_c}\left[1 - \exp\left(-\frac{L_c}{L_p}\right)\right]\right). \tag{2.12}$$

One gets $R_g^2 \approx L_c^2/12$ in the short-chain limit and $R_g^2 \approx L_c L_p/3 = L_c b_k/6$ in the long-chain limit.

Now let's come back to the example of dsDNA introduced at the beginning of this section. The dsDNA has a persistence length of $L_p \approx 50\,nm$, equivalent to 150 base pairs, while for a ssDNA, the persistence length reduces to $L_p \approx 2\,nm$. For theoretical analysis and simulations, although we use dimensionless units, the choice of parameters for the polymer models has to be realistic. The physical properties such as the rigidity of the polymers (*i.e.*, L_p) has to be treated carefully in our polymer models.

2.1.4 Excluded volume

In ideal chain models, monomers are allowed to overlap. In reality, monomers have finite volumes and thus interact with other monomers that come close in the same region. This is called the *excluded volume effect*. Similar to the expression for the end-to-end distance of an ideal chain in eq. 2.6, the size of a real polymer also depends on a power law of N, which can be written as

$$R_g \propto bN^{\nu}, \tag{2.13}$$

where ν is the volume exponent that takes the excluded volume effect into account. Plenty of works have been done to find the exponent ν. The best known theory is the simple argument first proposed by Paul Flory [53]. The idea is that the interaction energy from the swelling of the ideal chain due to the excluded volume interaction should be balanced by the entropic elastic energy to maintain the conformation in thermal equilibrium. When we add the excluded volume Nb^3 to the ideal chain monomers confined in a 3D space of total volume $\langle h^2 \rangle^{3/2}$, the interaction energy for the polymer is

$$U_{ev} \approx N\frac{Nb^3}{h^3}k_B T. \tag{2.14}$$

The free energy of an ideal chain with a certain end-to-end distance $\boldsymbol{h}$ is simply

$$U_F \approx k_B T \ln\left(\Psi(\boldsymbol{h}, N)\right) \approx \frac{h^2}{Nb^2}\ k_B T \tag{2.15}$$

where k_B is the Boltzmann constant and T the temperature. By minimizing the sum of the two energies $\partial(U_{ev} + U_F)/\partial h = 0$, one finds that $\nu = 3/5$, which is called the Flory exponent to honor his contribution to the field [54].

In practice, the impact of the excluded volume interactions has to depend on the polymer/monomer size. Using dsDNA as an example, in the short-chain limit ($L_c < L_p$), it is impossible for different parts of the chain to collide without breaking the bonds, otherwise when $L_c \gg L_p$, the chain is eventually a flexible polymer, thus the probability of intra-chain interactions becomes significant. On the other hand, if we assume the size of the backbone is infinitely small, then of course there will be no excluded volume interactions. In fact, the critical size of the polymer for excluded volume to kick in is given by [54]

$$L_c^* \approx b_k^3/b^2 \tag{2.16}$$

For dsDNA as an example, b is the size of the backbone, which is roughly $2\,nm$ while the Kuhn monomer size is $b_k \approx 100\,nm$; we then have a critical length $L_c^* \approx 2.5 \times 10^5\,nm$, which corresponds to $800\,kbp$. For ssDNA, $b_k \approx 3\,nm$ and $b \approx 1\,nm$, thus we get $L_c^* \approx 27\,nm \approx 60\,bp$.

2.2 Polymer Dynamics

In the previous section, we examined the static properties of polymers. Now it is time to deal with polymer dynamics in a solvent. During translocation, the motion of the polymer chain is mainly governed by diffusion and electrophoresis. In this section, we briefly review the physical principles of polymer dynamics that are required for our simulations.

2.2.1 Thermal diffusion *vs* drift

Let's first consider a group Brownian particles diffusing randomly in a fluid. The concentration $C(x, t)$ at position x and time t is governed by the conservation law

$$\frac{\partial}{\partial t} C(x, t) = -\frac{\partial}{\partial z} J(x, t), \tag{2.17}$$

where the total particle flux is $J(x,t)$. Fick's law [55] states that the diffusive flux is generated by a gradient of concentration,

$$J(x,t) = -D\frac{\partial C}{\partial x}, \tag{2.18}$$

where D is the diffusion constant. In the presence of a nonzero external force $F = -\partial U/\partial x$, with U the potential, eq. 2.18 becomes

$$J(x,t) = -D\frac{\partial C}{\partial x} + Cv, \tag{2.19}$$

where $v = F/\gamma$ is the drift velocity, $\gamma = 6\pi\eta b$ is the friction coefficient for a spherical particle of hydrodynamic radius b (Stokes' law), and η is the viscosity of the fluid. In the stationary state $\frac{\partial C}{\partial t} = 0$, one gets

$$J^s(x) = -D\frac{\partial C^s}{\partial x} - \frac{C^s}{\gamma}\frac{\mathrm{d}U}{\mathrm{d}x} = 0, \tag{2.20}$$

where the superscript s refers to stationary. From eq. 2.20, one obtains the stationary concentration proportional to the Boltzmann factor of the potential energy,

$$C^s(x) \propto \exp\left(-\frac{U(x)}{k_B T}\right). \tag{2.21}$$

Combining eq. 2.20 and eq. 2.21, one gets

$$D = \frac{k_B T}{\gamma}, \tag{2.22}$$

which links the friction coefficient γ describing the resistance to the motion in a low Reynolds number solvent to the diffusion coefficient D from the random thermal perturbations from the fluid.

Instead of tracking a population of particles, one can always follow the dynamics of a single particle. The motion of a particle moving along the x axis is governed by three forces : (i) a dissipative force F^d due to the friction with the fluid ; (ii) a conservative force F^c due to an external potential $U(x)$; and (iii) a random/Brownian force F^B originating from the thermal bath. Combining all of these forces, one gets the Langevin equation [56]

$$m\frac{\mathrm{d}^2}{\mathrm{d}t^2}x(t) = \underbrace{-\gamma\frac{\mathrm{d}}{\mathrm{d}t}x(t)}_{F^d} - \underbrace{\frac{\mathrm{d}}{\mathrm{d}x}U(x)}_{F^c} + \underbrace{\sqrt{2D}\ R(t)}_{F^B}, \tag{2.23}$$

where m is the mass of the particle, k_BT the thermal energy and $R(t)$ a random function that satisfies $\langle R(t)\rangle = 0$ and $\langle R(t)R(t')\rangle = \delta(t-t')$. In cases where the viscous timescale m/γ is much smaller than all other relevant time scales (such as the timescale over which the conservative force $F^c(t)$ changes), the inertial term (*lhs* of eq. 2.23) can be neglected. We then obtain the overdamped Langevin equation

$$\gamma \frac{\mathrm{d}}{\mathrm{d}t} x(t) = -\frac{\mathrm{d}}{\mathrm{d}x} U(x) + \sqrt{2D}\ R(t). \tag{2.24}$$

With eq. 2.22, we can rewrite the overdamped Langevin equation of motion as

$$\frac{\mathrm{d}}{\mathrm{d}t} x(t) = -\frac{D}{k_BT}\frac{\mathrm{d}}{\mathrm{d}x} U(x) + \sqrt{2D}\ R(t). \tag{2.25}$$

2.2.2 Rouse *vs* Zimm polymers

Polymer dynamics can be treated as the collective motion of many particles each described by the above Langevin Dynamics. Considering a bead-spring polymer chain without excluded volume interactions or long-range hydrodynamic interactions (HI), the resulting polymer dynamics are described by *Rouse Dynamics*. The total friction coefficient for a polymer chain of N monomers is simply $N\gamma_o$, where $\gamma_o = 6\pi\eta b$ is the friction for a single monomer of size b. Therefore the center-of-mass diffusion coefficient for the polymer is simply

$$D_r = \frac{k_BT}{N\gamma_o}. \tag{2.26}$$

The time for a Rouse chain to diffuse its own size R_g is called *Rouse time*, and is given by

$$\tau_r \approx \frac{R_g^2}{D_r} \approx \frac{\gamma_o b^2}{k_BT} N^{1+2\nu} = \tau_o N^{1+2\nu}, \tag{2.27}$$

where $\tau_o = \frac{\gamma_o b^2}{k_BT}$. For an ideal chain, $\nu = 1/2$ and $\tau_r \sim N^2$, which contradicts the exponent 3/2 (theta solvent) observed in experiments. The reason for the discrepancy is that the hydrodynamic interactions are not considered in the model. This makes the Rouse polymer model useful only in situations where the long-range hydrodynamic interactions (HI), *i.e.* the correlations between the dynamics of different parts of the chain as mediated by the fluid, are screened. However, in other cases, long-ranged HI are not negligible.

The *Zimm model* demonstrates that the fluid in the polymer coil actually moves together with the chain and they form an impenetrable sphere. The center-of-mass diffusion coefficient is then given by the normal Stokes relation

$$D_z \approx \frac{k_B T}{\eta R_g} \approx \frac{k_B T}{N^\nu \gamma_o}. \tag{2.28}$$

The *Zimm relaxation time* for the chain is given by

$$\tau_z \approx \frac{R_g^2}{D_z} \approx \frac{\gamma b^2}{k_B T} N^{3\nu} = \tau_o N^{3\nu} \tag{2.29}$$

For ideal chains, $\tau_z \sim N^{3/2}$: this exponent is exactly what is found in experiments for theta solvent. Zimm polymers diffuse faster than Rouse polymers and require less time to relax, which indicates hydrodynamic interactions accelerate the dynamics.

In *Zimm model*, the polymer chain is a sphere that impermeable to the flow, the HI decay as $1/r$, where r is the distance from the center of mass. This introduces another important length metrics to characterize the polymer chain conformation in dynamics called the *hydrodynamic radius*, which is given by

$$\frac{1}{R_H} = \left\langle \frac{1}{|\boldsymbol{r_j} - \boldsymbol{r_i}|} \right\rangle \tag{2.30}$$

For ideal polymers, $R_H^2 \approx (0.665 R_g)^2$, which is simply because the beads at short distances from the center of mass are weighed more in the above average.

2.2.3 Electrophoresis

The motion of charged macromolecules, ions, and colloidal particles in a fluid under the action of an electric field is called electrophoresis. When a charged analyte is submerged in an electrolyte solution, it attracts the ions with opposite signs (counterions) to neutralize its surface charge. The concentration of the surrounding counterions is determined by the strength of the electrostatic attraction and the entropic energy due to the thermal agitation [57]. For a negatively charged colloidal particle as an example, the equilibrium charge distribution at the interface is shown in Fig. 2.2 (a). The inner monolayer of counterions that are attracted firmly to the particle surface is called the Stern layer. The outer layer is called the *Debye layer*, where the counterions are free to move and the decay length of the counterions concentration is called *Debye length* λ_D. The Debye-Hückel approximation [58] gives

$$\lambda_D = \sqrt{\frac{\varepsilon k_B T}{\sum_i^N n_i q_i^2}}, \tag{2.31}$$

where $\varepsilon = \varepsilon_o \varepsilon_r$ is the permittivity as the product of vacuum permittivity ε_o and the relative permittivity ε_r of the medium, n_i and q_i are the number concentration and charge of the i-th species. The Debye length depends on the salt conditions and temperature. For example, it is roughly a few tens of nanometers in a monovalent-ion salt concentration of 1 μM at room temperature.

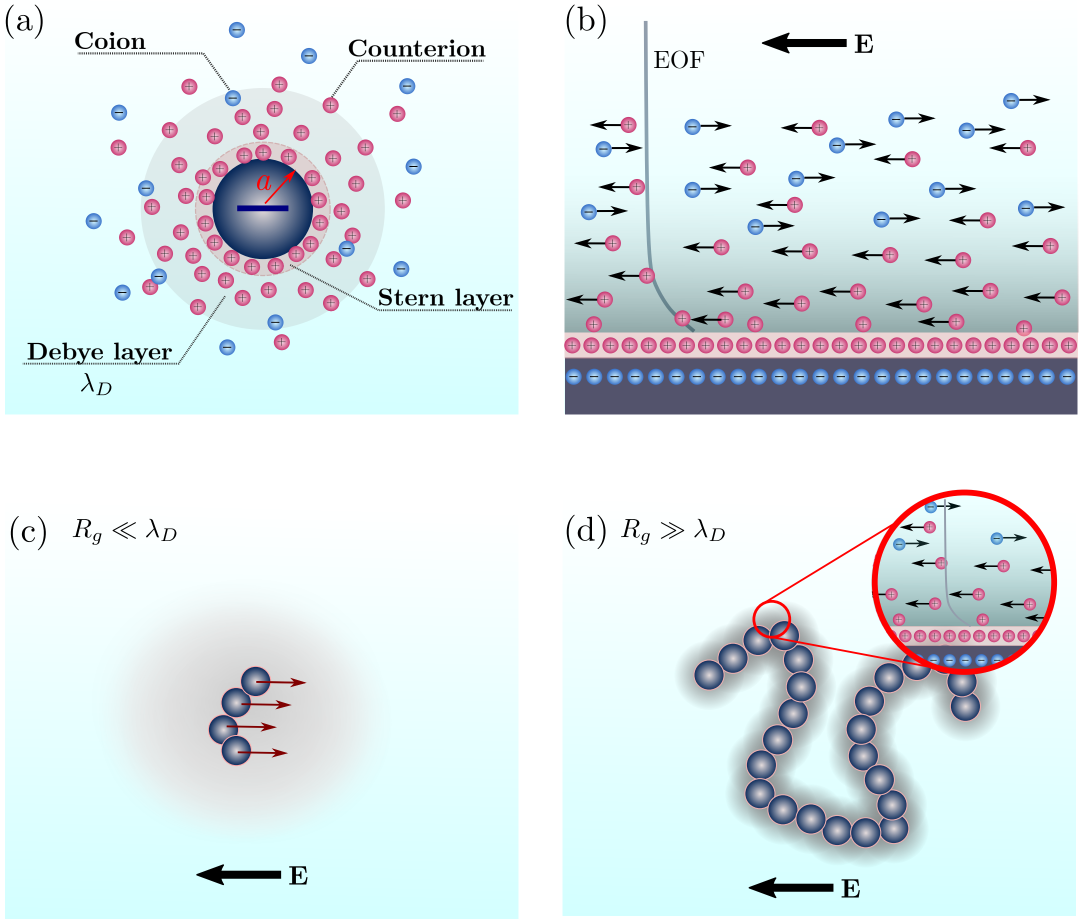

FIGURE 2.2 – (a) Schematic plot of the electric double layer for a negatively charged particle of radius a ; the charged beads colored in red and blue are counterions and coions. (b) Electroosmotic flow (EOF) near a charged flat surface under a field $\boldsymbol{E}$; the gray curve indicates the flow profile which decays rapidly to zero at the surface of the Stern layer. (c). Electrophoresis of an oligomer with a large Debye length ($R_g \ll \lambda_D$) ; the brown arrows indicate the direction of motion in the reference frame of the solvent. (d). Electrophoresis of a long polymer chain with a thin Debye length ($R_g \gg \lambda_D$) is driven by the EOF.

In the presence of an electric field, there are two different limits of interest to discuss. In the large particle limit, the Debye length is thinner than the radius of the particles

($\lambda_D \ll a$). The negatively charged particle surface can be locally treated as a flat surface as shown in Fig. 2.2b. The counterions move in the direction of the field, which transfers net momentum to the fluid and thus introduces a flow in the direction of the field, this is the so-called Electroosmotic flow (EOF). The electroosmotic velocity of the flow is uniform for distances $\gg \lambda_D$ and is given by [57,59]

$$\boldsymbol{u}(\infty) = -\frac{\varepsilon\Phi_o}{\eta}\boldsymbol{E}, \tag{2.32}$$

where Φ_o is the electrostatic potential at the charged surface (*i.e.* the Stern layer), η is the fluid viscosity and E is the electric field. The flow velocity decays within the double layer and becomes zero at the Stern layer. Therefore, using the fluid medium as the reference, the velocity of the particle is $-u(\infty)$. The electrophoretic mobility of the particle is thus given by

$$\mu_l = \frac{\boldsymbol{u}(\infty)}{\boldsymbol{E}} = \frac{\varepsilon\Phi_o}{\eta} \tag{2.33}$$

In the small particle limit, the size of the particle is smaller than the Debye length ($a \ll \lambda_D$), and the charged surface is not able to create a dense continuum double layer. The particle can thus be treated as a bare point-charge particle. The friction from the fluid due to the motion is directly balanced by the electric field

$$q\boldsymbol{E} = \gamma\boldsymbol{v} = 6\pi\eta a\boldsymbol{v}, \tag{2.34}$$

where $q = 4\Phi_o\pi\varepsilon a(1+a/\lambda_D) \approx 4\Phi_o\pi\varepsilon a$ is the net charge of the spherical particle calculated from the surface potential [59]. Therefore, the electrophoretic mobility of the particle in the small particle limit is

$$\mu_s = \frac{q}{\gamma} = \frac{2\varepsilon\Phi_o}{3\eta}. \tag{2.35}$$

As we mentioned previously, the Debye length is typically a few tens of nanometers ; therefore Å-size ions, nano-sized particles or folded proteins, and short DNA segments ($\leq 20\,bp$), are all in the small particle limit. Figure 2.2c shows the electrophoresis of a negatively charged short oligomer in this limit. The motion of the oligomer is solely due to the direct electric force on the charged site. Otherwise, for long polymers, as shown in Fig. 2.2d, the surface of the chain is locally like a charged plane with a thin Debye layer, and EOF passes through the polymer chain in the field direction. By changing the frame of reference to the fluid, the polymer is moving in the opposite direction of the field. Therefore, both polymers are moving in the same direction yet via different mechanisms.

2.2.4 Polyelectrolytes and DNAs

We previously discussed two different limits of particle electrophoresis by comparing their size to the Debye length λ_D, which is the decay length of the counterions density from the charged surface. We note that λ_D depends on the ionic concentration, the permittivity of the medium, and the temperature. Here we introduce another length scale to characterize the strength of the electrostatic interactions in a solvent and we then use it to introduce the concept of Manning condensation.

Let us first consider a simple electrolyte solution consisting of fully dissociated monovalent ions. The electrostatic energy between two ions is

$$U_e(r) = \frac{e^2}{4\pi\varepsilon r}. \tag{2.36}$$

By balancing it with the thermal energy $k_B T$, one gets the *Bjerrum length*

$$\ell_B = \frac{e^2}{4\pi\varepsilon k_B T}. \tag{2.37}$$

If the separation between two ions is smaller than ℓ_B, the interactions between two ions are strong ; otherwise, there would be only weak or no interaction. Differentiating from the Debye length we introduced previously, ℓ_B solely reflects the solvent properties, which are the permittivity ε and temperature. As a reference, $\ell_B \approx 0.7\,nm$ in water at room temperature.

Now consider a polyelectrolyte in water : the ionic groups dissociate to two opposite charged ions, one is part of the surface of the chain, and the oppositely charged ion has two options : If the charge density $\rho_e < e/ell_B$, the separation of the charges is too large for this ion to remain on the polyelectrolyte : the counterions then move away from the surface. Otherwise, if $\rho_e > e/ell_B$, the counterions accumulate near the surface to neutralize the charges. This process is called *Manning condensation*. Considering a dsDNA in water at room temperature, each basepair has a contour length of $b_c = 0.34\,nm$ and carries two charges, which corresponds to a charge density $\rho_e \approx 4\,e/ell_B > e/ell_B$. As a result of Manning condensation, $\approx 3/4$ of the total chemical charges is screened, which give an effective charge $Q_{eff} \approx \frac{1}{4}Q$. For ssDNA, $b_c = 0.43\,nm$, thus $\rho_e \approx 1.6\,e/ell_B > e/ell_B$, thus $Q_{eff} \approx 0.625\,Q$.

3

Simulation methods : from point-like particles to flexible polymers

Computational modeling and simulations are powerful tools that allow us to track the dynamics of specific systems. Those tools are widely used to study the dynamics of soft matter and fluid systems. The biggest advantage of simulations is that they can help us investigate the effects of different components such as the structure of the analytes, external perturbations, fluid dynamics, geometric constraints, *etc.*, all over interesting time- and length- scales. With that being said, the simulations are not only useful to explain the experimental results or understand the underlying mechanisms, but they also are convenient test toolkits for theoretical ideas.

In the past few decades, various simulation techniques have been developed to study polymer dynamics as summarised in this excellent review paper [60]. In general, there are three categories of simulation methods : the first category is Molecular Dynamics (MD) simulations with explicit solvent modeled by either atomistic/coarse-grained simulation or mesoscopic fluid methods such as Dissipative Particle Dynamics (DPD), Stochastic Rotation Dynamics (SRD), or Lattice Boltzmann (LB). The other category is Langevin Dynamics (LD) simulations with implicit fluid : the polymer-solvent HI are thus simplified to a frictional force opposing the motion, and random kicks arising from collisions with the solvent. The third category is Monte Carlo (MC) simulations of a coarse-grained polymer generally focused on the equilibrium properties of the system. Of course, with the development of new artificial intelligence techniques, new hybrid methods including machine learning and neural networks are continuously proposed and vigorously applied in the field.

The goal of this chapter is to give a brief overview of the simulation methods used to produce the results presented in this thesis. We will first introduce the Lattice Monte

Carlo (LMC) approach used in Chapters 4 and 5 to study the capture of point-like particles. This is followed by the LD simulations used to study the capture of rod-like and semiflexible polymers in Chapters 6 and 8. Finally, the LD simulations are coupled to a Lattice Boltzmann fluid (LD-LB) to study the capture and translocation of raspberry-like rods while taking into account electrohydrodynamics interactions (EHI) in Chapter 7 and Appendix A.

3.1 Lattice Monte Carlo for point-like particles

The LMC algorithm in general is a convenient way to study the dynamics of point-like particles with/without external bias if one can properly choose the time and lattice steps. The point-like particles can be salt ions, small globular protein particles, or even polymers if we can neglect the shape and entropic effects due to the conformational changes. Consider a particle that undergoes unbiased diffusion on a 1D lattice (Fig. 3.1a) : the probabilities to jump to the adjacent lattice site during a given time step are equal : for example we can choose

$$P_{\pm} = \frac{1}{2}. \tag{3.1}$$

The corresponding time step for the jump is then simply the mean first-passage time to arrive at the next lattice site [61] :

$$\tau = \frac{a^2}{2D}, \tag{3.2}$$

where a is the lattice step size and D is the diffusion coefficient of the particle in the medium. Ideally, the smaller the lattice step size the closer the system is to a continuum space, thus the more accurate the algorithm. However, a small lattice step is not always feasible due to the limit of computational resources. For a given lattice size, to recover the correct fourth moment of the particle displacement distribution function, one needs to choose the probability of jumping [62]

$$P_{\pm} = \frac{1}{6}. \tag{3.3}$$

This gives the new time step $\tau_s = 1/3\,\tau$. As shown in Fig. 3.1b, one has to introduce a probability to stay put as

$$P_s = 1 - P_+ - P_- = \frac{2}{3} \tag{3.4}$$

to ensure the these probabilities sum up to 1 at each time step.

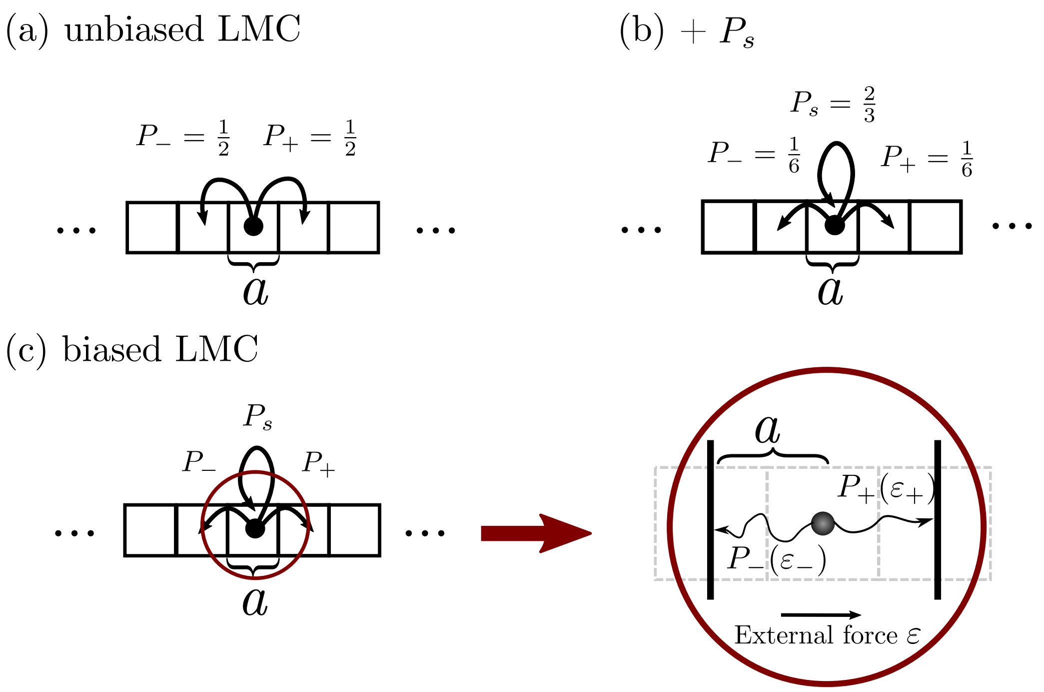

FIGURE 3.1 – Diagram of a 1D Lattice Monte Carlo (LMC) simulation algorithm. (a) Unbiased 1D LMC. (b) Unbiased 1D LMC with a probability to stay put (P_s) added. (c) Biased 1D LMC with probabilities that depend on the local external field ϵ.

3.1.1 LMC under a bias

In the presence of a bias, the probability of jumping to an adjacent site has to be impacted by the external force. The probabilities of jumping to the neighbor lattice sites can be directly calculated via a first-passage time approach as if a particle diffuses between two absorbing walls placed at the center of the two adjacent lattices sites (Fig. 3.1c) [61,63]. In absence of bias, the probabilities $P_\pm$ for the particle to be absorbed by either wall are equal, as shown in Figs. 3.1a and b. However, if there is a weak bias $\boldsymbol{\varepsilon}$, the probability for the particle to be absorbed by the right wall before the left one is $P_+(\varepsilon)$, which is a function of the bias ε. Consequently, one gets $P_-(\varepsilon) = 1 - P_+(\varepsilon) - P_s$. The time step is simply the mean time duration for the jump. Again, P_s is introduced to achieve a higher accuracy, which is particularly useful to ensure that we have correct jumps for all lattice sites when the external bias is not uniform. This approach is used in Chapter 4, with the biased first passage probabilities calculated by Hubert [63]. Here we show an alternative approach with probabilities calculated from the stationary distribution function. We first discretize eq. 2.21 onto a 1D lattice. Particles residing on lattice sites i and $i+1$ can jump between the two lattice sites with probabilities $P_{i\leftrightarrow i+1}$. To satisfy detailed balance and ensure microscopic reversibility in the stationary state, one has

$$C_i^s P_{i\to i+1} = C_{i+1}^s P_{i+1\to i} \ . \tag{3.5}$$

Using eq. 2.21, one obtains

$$\frac{P_{i\to i+1}}{P_{i+1\to i}} = \exp(\Delta\epsilon_i), \tag{3.6}$$

with $\Delta\epsilon_i = \epsilon_{i+1} - \epsilon_i$ and $\epsilon_i = U_i/k_B T$ (here U_i is the potential energy at lattice site i). As a closure relation for these equations, we assume local dynamics under a weak force is still valid, which can be written as

$$P_{i\to i+1} + P_{i+1\to i} = 2D\Delta t/a^2, \tag{3.7}$$

where Δt is the time step to be used for the simulations. The end result is

$$P_{i\to i+1} = \frac{2D}{a^2} \times \frac{1}{1+\exp\left(\Delta\epsilon_i\right)} \times \Delta t, \tag{3.8}$$

$$P_{i+1\to i} = \frac{2D}{a^2} \times \frac{1}{1+\exp\left(-\Delta\epsilon_i\right)} \times \Delta t. \tag{3.9}$$

Since the probability of not jumping during a time step, $P_{i\to i} = 1 - P_{i\to i-1} - P_{i\to i+1}$, must be $\geq 0 \ \forall i$, we must have

$$\Delta t \leq 1/\max[R_{i\to i-1} + R_{i\to i+1}], \tag{3.10}$$

where the hopping rates are $R_{i\to i\pm1} = P_{i\to i\pm1}/\Delta t$. Again, in order to achieve optimal accuracy, the time step $\Delta t = \frac{1}{3}\,\Delta t_{max}$ can be chosen to insure $P_{i\to i} \geq \frac{2}{3}$ everywhere on the lattice.

With the probabilities and time step information, the LMC algorithm can be used in two different ways :

I) To study the motion of a given particle : Using the probabilities described above, random numbers are generated at each time step to choose whether the particle will jump over a length $\pm a$ (the lattice step) in the x direction or stay put.

II) To follow a population of particles on the lattice : one can also work with the time evolution of the particle distribution instead of individual particles. The population of particles on each lattice is governed by the master equation. The concentration C_i^{j+1} at lattice site i and time step $j+1$ reads

$$C_i^{j+1} = P_{i-1\to i}C_{i-1}^j + P_{i+1\to i}C_{i+1}^j + P_{i\to i}C_i^j, \tag{3.11}$$

where i, j are integers.

3.2 Langevin Dynamics simulations

The LD simulations presented in this thesis are all performed using the software package ESPResSo 4.0 [64], which is designed for MD simulations to study the dynamics of coarse-grained soft matter ranging from colloidal particles to macromolecules.

3.2.1 Coarse-Grained Polymer

The first step of the LD simulations is to create a coarse-grained polymer model. For a linear polymer chain as an example, we first add N beads to form a self-avoiding random walk (SAW) chain configuration. Then we add excluded volume interactions between the beads to give them a finite size. The Lennard-Jones (LJ) potential is widely used to describe how particles interact in a variety of physical systems. In general, it has two components : the particles repel each other for short distances while attracting each other when they move away. Of course no interaction exists when the separation between the two particles exceeds a certain distance. Here we only need repulsive interactions ; thus, by truncating the potential at $r_c = 2^{1/6}\sigma$ and shifting upwards the LJ potential by its minimum value ϵ, one gets the purely repulsive Weeks-Chandler-Andersen (WCA) potential [65]

$$U_{\text{WCA}}(r) = \begin{cases} 4\epsilon\left[\left(\frac{\sigma}{r}\right)^{12} - \left(\frac{\sigma}{r}\right)^{6}\right] + \epsilon & \text{for } r < r_c \\ 0 & \text{for } r \geq r_c. \end{cases} \tag{3.12}$$

The WCA potential has a continuous slope which prevents an infinite force at r_c, and gives an effective size of the "soft" monomer as σ.

Secondly, to build the chain, we connect adjacent beads by a spring. The spring potential is the purely attractive Finitely-Extensible-Nonlinear-Elastic (FENE) potential

$$U_{\text{FENE}}(r) = -\frac{1}{2}K_{\text{FENE}}r_0^2 \ln\left(1 - \frac{r^2}{r_0^2}\right) \tag{3.13}$$

with a spring constant K_{FENE}. In contrast to an harmonic potential, the FENE potential has a maximum extension r_0. The combination of the WCA repulsion and FENE potential give a mean bond length is $\langle b\rangle \approx 0.96\,\sigma$ if one chooses $\epsilon = k_BT$, $r_0 = 1.5\,\sigma$ and $K_{\text{FENE}} = 30\,\epsilon/\sigma^2$.

Finally, to control the stiffness of the polymer chain an angular constraint is required. We use the angular harmonic potential given by

$$U_{\text{Bend}}(\theta) = \tfrac{1}{2}K_{\text{Bend}}\left(\theta - \pi\right)^2, \tag{3.14}$$

where θ is the angle between two consecutive bonds and K_{Bend} is the bending constant. As we saw before, the correlation between two adjacent bond vectors (eq. 2.7 in Chapter 2) decays exponentially as $e^{-\frac{b|i-j|}{L_p}}$. When associating this with the correlations evaluated using the Boltzmann factor of the constraint potential, $e^{-U_{\text{Bend}}/k_bT}$, one gets an estimated polymer persistence length $L_p/\sigma \approx K_{\text{Bend}}/k_BT$ [66], which can be used to guide the choice of the simulation parameter K_{Bend}. Please note, there are also other options available for the angular constraint, such as the cosine angle potential, the harmonic cosine potential, the tabulated angle potential. We chose the angular harmonic potential simply because it's straightforward and most commonly found in polymer simulations.

3.2.2 Langevin Equation Formalism

The LD equations for a single particle has been introduced in Chapter 1 under Sec. 2.2.1. For the sake of completeness, here I rewrite the equation and add all the bonded and non-bonded interactions of the polymer chain model. The motion of each bead is thus governed by

$$m\dot{\boldsymbol{v}} = \boldsymbol{\nabla}U(\boldsymbol{r}) - \gamma\boldsymbol{v} + \sqrt{2\gamma k_{\text{B}}T}\;\boldsymbol{R}(t), \tag{3.15}$$

where $\boldsymbol{\nabla}U(\boldsymbol{r}) = \boldsymbol{\nabla}(U_{\text{WCA}} + U_{\text{FENE}} + U_{\text{Bend}} + U_{\text{E}})$ is the sum of the conservative forces, $U_{\text{E}}(\boldsymbol{r})$ is the external potential, m is the mass of a bead, γ is the bead friction coefficient and $-\gamma\boldsymbol{v}$ is the damping force from the fluid. The last term $\boldsymbol{R}(\boldsymbol{r},t)$ is the noise that models random kicks from the solvent. The random variable $\boldsymbol{R}(\boldsymbol{r},t)$ satisfies

$$\begin{aligned}\langle \boldsymbol{R}(\boldsymbol{r},t)\rangle &= 0\\ \langle \boldsymbol{R}(\boldsymbol{r},t)\boldsymbol{R}(\boldsymbol{r'},t')\rangle &= \delta(t-t')\delta(\boldsymbol{r}-\boldsymbol{r'})\end{aligned}$$

where $\delta(t)$ is the Dirac delta function.

3.3 Langevin Dynamics coupled to a Lattice Boltzmann fluid

In order to explicitly include the hydrodynamic interactions in my models, I implemented a GPU-based Lattice-Boltzmann method (LBM) to simulate the solvent dynamics and I coupled it to the polymer LD simulations via a force scheme. The core of the method is to discretize and solve the Boltzmann transport equation on a lattice [67]. Although I use the LB solver built-in ESPRresSo package for all the simulations, it's necessary to have a look at the algorithms under the hood in order to use them sensibly.

For single particles, the Boltzmann transport equation can be written as

$$\partial_t f(\mathbf{r}(t), \mathbf{u}(t), t) = \partial_t f + \mathbf{u} \cdot \nabla_r f + \tfrac{\mathbf{F}}{m} \cdot \nabla_u f \tag{3.16}$$

with f the particle distribution function per unit phase-space volume ; $\mathbf{r}$, m and $\mathbf{u}$ the position, mass and velocity of the particles ; and $\mathbf{F}$ the external force. The term $\partial_t(\mathbf{r}(t), \mathbf{u}(t), t)$ describes the change in particle distribution due to particle interactions ; it is zero for non-interacting particles. For interacting particles, the above equation cannot be solved analytically and thus requires a statistical treatment of particle collisions.

Discretizing the *lhs* of eq. 3.16 on a lattice, one obtains

$$f_i(\mathbf{r} + \mathbf{u}_i\delta t, t + \delta t) = f_i(\mathbf{r}, t) + K_i(f_i(\mathbf{r}, t)) \tag{3.17}$$

where $f_i(\mathbf{r}, t)$ is the number of particles with velocity $\mathbf{u}_i$ at lattice site $\mathbf{r}$ at time t, δt is the time step and $K_i(f_i(\mathbf{r}, t))$ is the collision operator. Subscript i is the direction to the next lattice site connected by vector $\mathbf{u}_i\delta t$. The velocity vectors $\mathbf{u}_i$ have to be chosen such that the new position $\mathbf{r} + \mathbf{u}_i\delta t$ is always on the lattice.

The choice of the lattice is flexible. ESPResSo implements the D3Q19 lattice model for the discretized velocities in 3D systems. This includes a stationary (zero) velocity and 18 velocity vectors with 6 pointing to the nearest neighbor nodes, and 12 to next-nearest neighbor lattice nodes. The mass density ρ, the momentum density j and the stress tensor Π can be directly calculated from the distribution function :

$$\rho(\mathbf{r}, t) = \sum_{i=0}^{18} f_i(\mathbf{r}, t), \tag{3.18}$$

$$j(\mathbf{r},t) = \sum_{i=0}^{18} f_i(\mathbf{r},t)\mathbf{u}_i, \tag{3.19}$$

$$\Pi(\mathbf{r},t) = \sum_{i=0}^{18} f_i(\mathbf{r},t)\mathbf{u}_i\mathbf{u}_i. \tag{3.20}$$

The next step is to deal with the collisions between interacting particles. One of the simplest choices is the linear collision operator $K_i(f_i) = L_i(f_i^{eq} - f_i)$, which assume the collision linearly relaxes the populations to the local equilibrium f_i^{eq}, where L_i is the collision matrix. The equilibrium distribution f_i^{eq} can be written as [68]

$$f_i^{eq}(\rho,\boldsymbol{u}) = w_i\left[\rho + \frac{\boldsymbol{u}\cdot\boldsymbol{c_i}}{c_s^2}\rho + \frac{\boldsymbol{uu} : (\boldsymbol{c_i c_i} - c_s^2\mathbf{1})}{c_s^4}\rho\right] \tag{3.21}$$

where the speed of sound c_s depends on the mesh property, w_i is a weight to be tuned such that the LB model recovers the macroscopic Navier–Stokes equations. To satisfy mass and momentum conservation, $\sum_i K_i = 0$ and $\sum_i K_i\mathbf{u}_i = 0$ must satisfied, respectively.

The last step is to connect the fluid dynamics and the LD description of the analyte shown in the previous section via a force coupling method. The coupling is implemented via a friction force

$$\boldsymbol{F}_\gamma = -\gamma(\mathbf{v} - \mathbf{u}_b), \tag{3.22}$$

where γ is the friction coefficient, $\mathbf{v}$ is the bead's velocity, and $\mathbf{u}_b$ is the fluid velocity at the bead position. The key step is to replace the second term on the *rhs* of eq. 3.15 with $\boldsymbol{F}_\gamma$. To conserve the momentum of the overall system, fluctuations need to be added to both the fluid and the monomers; for the fluid, the fluctuation can be added to the stress tensor [69]. Similarly, if you apply an external force $\boldsymbol{\nabla}U(\boldsymbol{r})$ on the monomers, the opposite force $-\boldsymbol{\nabla}U(\boldsymbol{r})$ is also needed for the fluid. As a result of coupling, the hydrodynamic radius of a individual bead is given by

$$\frac{1}{R_H} = \frac{6\pi\eta}{\gamma} + \frac{6\pi g}{a} \tag{3.23}$$

where a is the lattice size and $g = 0.04$ is the constant for the interpolation scheme D3Q19 [70].

Lastly, in the simulations presented in Chapter 7, counterions and salt ions are included in the simulations. The electrostatic energy between two charges q_i and q_j separated by r is governed by the coulomb potential $U_{\mathrm{E}}(\boldsymbol{r}) = c\frac{q_i q_j}{r}$; here the prefactor is given by $c = \ell_B k_B T/e^2$ with the Bjerrum length $\ell_B = e^2/4\pi\varepsilon k_B T$, and ε is the permittivity of the media. The electrostatic interactions decay very slowly as $1/r$. If you have N interacting particles, the total electrostatic energy is challenging to compute and not well defined in the presence of periodic boundary conditions. In ESPResSo, the particle-particle-particle-mesh algorithm (P^3M) is used to deal with periodic boundary conditions for the slowly decaying long-range electrostatic interactions between charged beads. The core idea of the approach is to split the Coulomb interactions into two components and sum the short-range force on the normal coordinate and the long-range force in reciprocal space using Fourier transformation. The detailed derivation can be found in Refs. [71, 72].

4

Voltage-driven translocation : defining a capture radius

Reproduced from :
Qiao, Le, Maxime Ignacio, and Gary W. Slater,
J. Chem. Phys. 151, 244902 (2019) ;
https ://doi.org/10.1063/1.5134076,
with the permission of AIP Publishing

The Journal of Chemical Physics

ARTICLE

scitation.org/journal/jcp

Voltage-driven translocation: Defining a capture radius

Cite as: J. Chem. Phys. 151, 244902 (2019); doi: 10.1063/1.5134076
Submitted: 29 October 2019 • Accepted: 7 December 2019 •
Published Online: 24 December 2019

Le Qiao, Maxime Ignacio, and Gary W. Slater[a)]

AFFILIATIONS

Department of Physics, University of Ottawa, Ottawa, Ontario K1N 6N5, Canada

[a)]Electronic mail: gary.slater@uOttawa.ca

ABSTRACT

Analyte translocation involves three phases: (i) diffusion in the loading solution, (ii) capture by the pore, and (iii) threading. The capture process remains poorly characterized because it cannot easily be visualized or inferred from indirect measurements. The capture performance of a device is often described by a *capture radius* generally defined as the radial distance R^* at which diffusion-dominated dynamics cross over to field-induced drift. However, this definition is rather ambiguous and the related models are usually oversimplified and studied in the steady-state limit. We investigate different approaches to defining and estimating R^* for a charged particle diffusing in a liquid and attracted to the nanopore by the electric field. We present a theoretical analysis of the Péclet number as well as Monte Carlo simulations with different simulation protocols. Our analysis shows that the boundary conditions, pore size, and finite experimental times all matter in the interpretation and calculation of R^*.

I. INTRODUCTION

The field-driven translocation of a charged analyte across a nanopore[1–13] has been studied extensively over the past two decades due to its potential applications, especially for DNA detection and sequencing. Translocation involves three major steps for the analyte: (i) diffusion toward the nanopore, (ii) capture by the electric forces near the nanopore, and (iii) passage (or threading for polymers) through the nanopore. The last step, which has been the subject of numerous *in vivo* and *in silico* studies, is controlled by factors such as the electro-osmotic flow,[14] pressure and concentration gradients,[15–18] entropic effects,[19,20] and electric forces.[2,15] However, the diffusion-and-capture process remains rather ill-understood because it cannot easily be observed; moreover, in the case of polyelectrolytes, the interplay between the diffusion/drift and the polymer conformational deformations complicates modeling.[21,22]

Ideally, a translocation device should have a large capture zone and a high capture rate.[12,17,23] The former is generally described by a quantity called the capture radius, R^*, which is typically reported[24] to be ~μm. Theoretically, R^* is loosely defined as the radial distance at which diffusion-dominated dynamics (at large distances) crosses over to drift-dominated dynamics (close to the pore) in a steady-state regime.

One way to estimate R^* for a particle is thus to compare its electrostatic and thermal energies.[15,24–28] The minimal work needed to bring it from r to infinity is[27]

$$\frac{W(r)}{k_BT} = \frac{\mu}{D} V(r), \tag{1}$$

where D and μ are the particle's diffusion coefficient and electrophoretic mobility, respectively, k_BT is the thermal energy, and

$$V(r) = \Delta V \frac{r_e}{r} \tag{2}$$

is the point-charge approximation[15,27–29] for the electric potential at a distance r when a voltage difference ΔV is applied across the system. Here, $r_e = r_p/(\frac{2l}{r_p} + \pi)$ is the characteristic length of the electrostatic potential outside a pore of radius r_p and length l.[28] The capture radius is then defined as the distance R^* at which $W(R^*) = k_BT$.[15,27,29] Using Eq. (1), this condition reads $V(R^*) = D/\mu$. Given Eq. (2), the resulting capture radius is

$$R^* = \frac{\mu\Delta V}{D} r_e. \tag{3}$$

Alternatively, we can define the capture radius as the point of no return[15,25,28] (or *event horizon* to borrow an expression from general relativity), i.e., the distance below which the particle cannot escape the attraction of the pore. The field-driven flux at r is simply

$$J_E(r) = \mu(r)E(r)C(r), \tag{4}$$

where $E(r) = \mathrm{d}V(r)/\mathrm{d}r$ is the electric field and $C(r)$ is the particle density. In this approach, the hemisphere of radius R^* is treated as a perfect absorber and the electric field is neglected beyond. The diffusive flux of particles reaching this hemisphere from the bulk is[25,27]

$$J_D = -DC_o/R^*, \tag{5}$$

where $C_o \equiv C(\infty)$ is the density in the undisturbed far bulk. The capture radius R^* is then defined as the location where the two fluxes are equal: $J_D(R^*) = J_E(R^*)$. To complete the calculation, we assume that $C(R^*) = C_o$ in Eq. (4); we then recover the result in Eq. (3).

In a third approach, R^* is defined as the distance at which the times taken by a particle to find the nanopore solely by diffusion or solely by electrophoresis are equal (this is basically a Péclet number method).[27] A simple scaling argument suggests that the diffusion time is

$$\tau_D^o \approx R^{*2}/D. \tag{6}$$

The drift time over distance R^* is approximated as

$$\tau_E^o \approx R^*/\mu E(R^*). \tag{7}$$

If we use the expression for $E(r)$ given before, we again obtain Eq. (3). However, the scaling argument for τ_D^o does not include the size r_p of the target that has to be found by diffusion: τ_D^o is thus underestimated. Moreover, since the electric field decays with r, the drift time should be integrated over the field lines instead of using the field at R^* in Eq. (7)—in other words, τ_E^o is overestimated. In conclusion, Eq. (3) provides a lower bound for R^*.

In this paper, we revisit some theoretical approaches and present 2D Lattice Monte Carlo (LMC) methodologies and results with different simulation protocols and boundary conditions in order to propose and test various definitions of R^* for pointlike analytes. We also examine the impact of the field lines near the pore, especially for short times.

II. BASIC ELEMENTS AND ESTIMATES

After looking at typical experimental conditions and the field lines around a nanopore, this section presents an analysis of the key variables, time, and length scales.

A. Experimental and simulation parameters

Our theoretical and computational studies focus on the capture process in the translocation system shown in Fig. 1. Although the analyte is pointlike, its properties are chosen to match that of DNA (see below) in order to compare to available experimental data (while this is not our main goal, such comparisons can be useful).

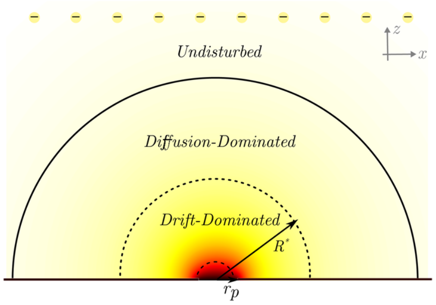

FIG. 1. A schematic view of a nanopore capture system: r_p is the pore radius and the background color codes for the electric field strength (higher fields in red). The dashed lines depict the capture radius R^* and a hemisphere of radius r_p. The solid line depicts the boundary of the region that remains undisturbed during an experiment.

We neglect DNA conformational entropic effects, analyte-analyte interactions, hydrodynamic interactions with the walls, and electroosmotic flow (EOF). Finally, the pore is treated as a perfect absorber. We use the pore radius r_p as the unit of length and $\tau_o = r_p^2/D$ as the unit of time.

The maximum electrostatic energy of a particle of charge Q is $\psi_o = Q \times \Delta V$. For a polyelectrolyte such as DNA, the relevant electrophoretic charge is $Q = k_BT\mu/D$ because the counterions, which move in the direction opposite to the DNA in an electric field, affect the local friction drag on the DNA backbone (this leads to a well-known failure of the fluctuation-dissipation theorem—see, for example, Refs. 27 and 30). Equation (3) can thus be rewritten as

$$R^* = \frac{\psi_o}{k_BT}\, r_e \equiv \lambda_e. \tag{8}$$

This basic capture radius is called the electrostatic length λ_e in this paper as it is the radial distance at which $W(r = \lambda_e) = k_BT$, and it will be used as a measure of the field intensity.

We will mostly use values for a 250 base ssDNA molecule:[31] $D \approx 17\ \mu\mathrm{m}^2/\mathrm{s}$ and $\mu \approx 4.1 \times 10^4\ \mu\mathrm{m}^2/\mathrm{V\ s}$, giving $Q \approx 60e$ ($\approx 1/4$ of the nominal charge). With a voltage $\Delta V = 800$ mV, the scaled potential energy is $\psi_o/k_BT \approx 1800$. Using a pore radius $r_p = 5$ nm and a pore length $l = 2r_p$, we have $r_e = r_p/(4 + \pi)$ and $\lambda_e \approx 250r_p \approx 1\ \mu$m. The time unit is thus $\tau_o = r_p^2/D \approx 1.5\ \mu$s here; a typical experimental duration of $t_{exp} = 0.5$ h is then $\approx 10^9\tau_o$.

B. The electric field

In most theoretical studies,[15,24–27,29] the electric field is modeled by treating the nanopore as a point charge, as described by Eq. (2), a good approximation if $r \gg r_p$. For distances comparable to r_p, though, the spherical symmetry is broken and this approximation is unreliable. Instead, one can solve Laplace's equation in oblate coordinates (ξ, η, ϕ) for the electric field outside the pore,[22,32]

$$V(\xi) = \tfrac{2}{\pi}\,\delta V\ \arctan[\sinh(\xi)], \tag{9}$$

where $\xi \in (-\infty, +\infty)$ is the oblate distance to the pore and δV is the potential drop from infinity to the pore. The prefactor can be written as

$$\frac{2}{\pi}\,\delta V = \frac{r_e}{r_p}\,\Delta V, \tag{10}$$

thus establishing a connection between δV and ΔV.

Note that close to the pore ($\xi < 1$ or, equivalently, $r < r_p$), the field is actually rather flat—see Appendix A. As $R^* \gg r_p$ for realistic cases, we will use the point-charge approximation for analytical calculations [indeed, the prefactor $\Delta V r_e/r_p^2$ in Eq. (A7) is the value predicted by Eq. (2) at $r = r_p$]. However, the flatness of the field near the pore will play a role in some cases.

C. Preliminary considerations

1. Velocity

The definition of λ_e allows us to rewrite the radial drift velocity $v(r) = \mu E(r)$ as

$$v(r) = -\lambda_e D/r^2. \tag{11}$$

Note that Eq. (5) is equivalent to a diffusive velocity

$$v_D(r) = -D/r. \tag{12}$$

As expected, these velocities are equal at $r = \lambda_e$.

2. Deterministic drift times

A useful parameter is the field-driven deterministic time to drift from position r_o to $r < r_o$ under the action of the electric field,

$$\tau_E(r_o, r) = \int_{r_o}^{r} \frac{dr'}{v_d(r')} = \frac{r_o^3 - r^3}{3\lambda_e D}. \tag{13}$$

For instance, the *cleanup time* τ_λ needed to empty the capture radius zone λ_e is then

$$\tau_\lambda = \tau_E(\lambda_e, 0) = \lambda_e^2/3D, \tag{14}$$

which is 1/3 of τ_E^o in Eq. (7). However, Eq. (13) is using the pointlike charge approximation and thus fails to take into account the fact that the field is fairly flat near the pore. The time to reach the pore from $r = r_p$ is

$$\tau_p \approx \frac{r_p}{|v(r_p)|} = \frac{r_p^3}{\lambda_e D} = 3\tau_E(r_p, 0). \tag{15}$$

Equation (13) thus underestimates (by a factor of ≈3) the time taken for the last part of the capture process. Since

$$\tau_p/\tau_\lambda = 3\,(r_p/\lambda_e)^3 \ll 1, \tag{16}$$

this has no impact in realistic cases.

3. The capture rate in 3D

The mean capture rate during the cleanup time τ_λ is

$$\bar{\rho}_\lambda \approx \tfrac{2\pi}{3}\lambda_e^3 C_o/\tau_\lambda = 2\pi D\lambda_e C_o\,, \tag{17}$$

while the initial rate (during the period required to "empty" the region of size r_p) is

$$\bar{\rho}_p \approx \tfrac{2\pi}{3} r_p^3 C_o/\tau_p = \tfrac{1}{3}\bar{\rho}_\lambda. \tag{18}$$

We thus expect the mean capture rate to initially (and rapidly) increase (by a factor ≈3) because of the special field lines near the pore [Eq. (A7)]. More generally, the total number of particles captured during a period of duration t is given by

$$N(t) \approx \tfrac{2}{3}\pi r^3(t) C_o, \tag{19}$$

where $r(t)$ is the size of the region emptied at time t. The capture rate at time t is thus

$$\rho(t) = \partial N(t)/\partial t = 2\pi C_o r^2(t)\frac{dr(t)}{dt}. \tag{20}$$

If we use Eq. (13) to estimate the size of this region, we obtain $r(t) \approx (3Dt\lambda_e)^{1/3}$ from which Eq. (20) predicts that $\rho(t) \approx \bar{\rho}_\lambda$ would be constant at long times.

4. The capture rate in 2D

Although our work is about the physics of 3D systems, our simulations will be done in 2D, for efficiency reasons (see Sec. IV for details). In this context, 2D means a slice of 3D system (as opposed to a system between two walls); therefore, a 3D electric field is used in both our analytical calculations and LMC simulations. In two dimensions, Eq. (17) must be replaced by

$$\bar{\rho}_\lambda \approx \tfrac{\pi}{2}\lambda_e^2 C_o/\tau_\lambda = \tfrac{3\pi}{2} D C_o, \tag{21}$$

where we used Eq. (14). Interestingly, the mean cleanup rate is not predicted to be a function of the field intensity in 2D. Similarly, the initial rate is now predicted to be

$$\bar{\rho}_p \approx \tfrac{\pi}{2} r_p^2 C_o/\tau_p = \tfrac{\pi\lambda_e}{2r_p} D C_o = \tfrac{\lambda_e}{3r_p}\,\bar{\rho}_\lambda. \tag{22}$$

A large drop of $\bar{\rho}$ is thus predicted in 2D (instead of the increase predicted for 3D in Sec. II C 3). Unlike the 3D case, the instantaneous capture rate does not become time-independent in 2D: for instance, using

$$N(t) = \tfrac{1}{2}\pi r^2(t) C_o, \tag{23}$$

we now find that

$$\rho(t) = \tfrac{2}{3}\bar{\rho}_\lambda \times [\tau_\lambda/t]^{1/3}, \tag{24}$$

from which we recover $\bar{\rho}_\lambda = \int_0^{\tau_\lambda} \rho(t)dt/\tau_\lambda = \rho_\lambda$, as should. From Eqs. (21) and (24), we also predict that $\rho(\tau_\lambda) = \pi D C_o$ should be field-independent.

5. Experiments

In practice, the experimental duration $t_{exp} \gg \tau_\lambda$: the λ_e zone is thus emptied $N = t_{exp}/\tau_\lambda \gg 1$ times during the experiment. If we assume that the concentration remains C_o in this zone during the experiment, the upper bound for the total number of molecules captured is $M = N \times \frac{2\pi}{3}\lambda_e^3 C_o = t_{exp} \times 2\pi D\lambda_e C_o = \bar{\rho}_\lambda t_{exp}$. Similarly, using the diffusion flux [Eq. (5)], the number of molecules that have diffused into the nominal capture zone during the experiment is also $M = 2\pi\lambda_e^2|J_D| \times t_{exp} = \bar{\rho}_\lambda t_{exp}$. Therefore, $\bar{\rho}_\lambda$ is indeed the mean capture rate predicted by the basic theory described in the Introduction; moreover, the calculation also predicts a constant capture rate past the initial jump mentioned above.

6. Numerical values

We now look at numerical estimates for the case described previously. With $\lambda_e \approx 1$ μm, Eqs. (11)–(17) give $v(r_p) \approx 1$ m/s, $v(\lambda_e) \approx 17$ μm/s, $\tau_\lambda \approx 20$ ms, and $\bar{\rho}_\lambda \approx (4.7\ \mu\text{m})^3 C_o/s = (C_o/16\ pM)/s$, which provides guidance for the concentration C_o to be used in practice.

III. THEORETICAL APPROACHES REVISITED

A. The Péclet argument with a small target

The dimensionless Péclet number (Pe) is used in Separation Science to characterize the competition between advection and diffusion.[33] Here, we define Pe as

$$Pe(r) = \tau_D(r,0)/\tau_E(r,0), \tag{25}$$

where $\tau_D(r, 0)$ is the mean time needed by a particle to find the pore (at $r = 0$) by diffusion alone when starting from a radial distance r, and $\tau_E(r, 0) = r^3/3D\lambda_e$ is the time for the same particle to travel to the pore when driven solely by the applied field—see Eq. (13).

The mean first passage time (MFPT) for a particle in Fig. 1 is analogous to a classical diffusion problem where a particle is initially located between two concentric spheres of sizes R_b and $r_D \ll R_b$, with the internal one being absorbing and the largest one being reflecting.[34–36] If the particle starts at radial position $R_b \geq r \geq r_D$, the MFPT is

$$\tau_D(r, r_D) = \frac{R_b^2}{6D}\left[\frac{2R_b}{r_D}\left(1 - \frac{r_D}{r}\right) + \left(\frac{r_D^2 - r^2}{R_b^2}\right)\right]. \tag{26}$$

The position r_D must be very close to the pore; we will use $r_D = r_p$ for simplicity. Using Eqs. (13), (25), and (26), we can calculate $Pe(r)$; since $r_p \ll R_b$ and $r_p \ll R^*$ in practice, we obtain

$$Pe(r) \approx R_b^3\lambda_e/r^3 r_p. \tag{27}$$

The Péclet capture radius is the solution of $Pe(R^*) = 1$,

$$R^* \approx R_b \times (\lambda_e/r_p)^{1/3}. \tag{28}$$

Since $\lambda_e \gg r_p$, R^* exceeds the box size R_b. However, both $\tau_E(R_b, 0)$ and $\tau_D(R_b, r_p)$ also exceed any realistic experimental time. Therefore, our Péclet result actually implies that R^* steadily increases during an experiment (i.e., the process is field-driven throughout). The time-dependent effective capture radius $R^*(t)$ is then obtained by inverting $\tau_E(r, 0) = r^3/3D\lambda_e$,

$$R^*(t) \approx (3\lambda_e Dt)^{1/3} = \lambda_e \times [t/\tau_\lambda]^{1/3}. \tag{29}$$

It increases as $\sim t^{1/3}$ and exceeds λ_e for times $t > \tau_\lambda$. For the previous example, with an experimental time $t_{exp} = 0.5$ h and a cleanup time $\tau_\lambda = 20$ ms, the final capture radius is $R^*(t_{exp}) \approx 45\lambda_e = 45$ μm, almost two orders of magnitude larger than what Eq. (8) predicts.

Interestingly, the situation is different in two dimensions since the MFPT is then

$$2D: \ \tau_D(r, r_D) = \frac{R_b^2}{4D}\left[2\ln\left(\frac{r}{r_D}\right) + \left(\frac{r_D^2 - r^2}{R_b^2}\right)\right]. \tag{30}$$

Combining this with Eq. (25), we obtain

$$2D: \ Pe(r) \approx \frac{3R_b^2\lambda_e}{2r^3}\left[\ln\left(\frac{r}{r_D}\right) - \frac{1}{2}\left(\frac{r}{R_b}\right)^2\right]. \tag{31}$$

To leading order, the solution of the Péclet condition $Pe(R^*) = 1$ thus gives a length scale

$$2D: \ R^* \approx (R_b^2\lambda_e)^{1/3}, \tag{32}$$

which means that we now have $R^* < R_b$. The time to reach the pore from this distance is $\tau_E(R^*, 0) \approx R_b^2/3D = (R_b/\lambda_e)^2 \times \tau_\lambda$. If t_{exp} is shorter than this time, Eq. (29) remains valid. Otherwise, we expect a transition to a diffusion-limited regime at long times.

B. A Péclet-inspired flux method

In the flux method used in the Introduction, the hemisphere of radius R^* is treated as an absorbing boundary [i.e., $C(R^*) = 0$] to obtain the diffusion flux [Eq. (5)]. Yet, $C(R^*) = C_o$ is used in the calculation of the field driven flux [Eq. (4)]. This inconsistency cannot easily be fixed. Moreover, since both the flux and energy methods give $R^* = \lambda_e$, the fact that $W(\lambda_e) = k_B T$ implies that the $R^* = \lambda_e$ hemisphere is *not* perfectly absorbing. One could try to get around this issue by using a hemisphere of radius r_o, with $r_p \leq r_o < \lambda_e$, as the location of the no-return point instead. As the field is extremely strong at $r_o = r_p$ [we have $W(r_p) \approx 250$ $k_B T$ for our example], this would truly be an absorbing boundary. However, any position r_o for which $W(r_o) \gg k_B T$ can also be chosen. Unfortunately, using this approach to recalculate the two sides of the equality, $J_D(R^*) = J_E(R^*)$ (the basis of the original flux method) fails to provide physically meaningful results (not shown).

An alternative approach is to use "pure adsorption fluxes" instead of the "pure" adsorption times τ_D and τ_E. We first compute the flux $J_E(r) = C(r, t)v(r)$ at a radial distance r with the initial condition $C(r, 0) = C_o$ and no diffusion. Since the molecules at position r at time t must all come from $r_o(r, t)$ at time $t = 0$, we have

$$C_E(r,t) = C(r_o, 0) \times \left(\frac{r_o}{r}\right)^2 = C_o\left(\frac{r_o}{r}\right)^2. \tag{33}$$

We can obtain the initial position directly from Eq. (13),

$$r_o(r,t) = r \times \left(1 + 3\lambda_e Dt/r^3\right)^{1/3}. \tag{34}$$

The time-dependent concentration is thus given by

$$C_E(r,t) = C_o\left(1 + 3\lambda_e Dt/r^3\right)^{2/3}, \tag{35}$$

and the zero-diffusion flux $J_E(r, t) = v(r)C_E(r, t)$ is

$$J_E(r,t) = -\frac{C_o D\lambda_e}{r^2}\left[1 + \frac{t/\tau_\lambda}{(r/\lambda_e)^3}\right]^{2/3}. \tag{36}$$

Without diffusion, there is no steady-state and $J_E(r, t)$ increases with time since the electric forces concentrate the molecules in a smaller volume closer to the pore.

To complete the calculation, we need the time-dependent solution[37] of the diffusion equation in the absence of an external field but with an absorber at $r_D = r_p$,

$$C(r,t) = C_o\left(1 - \frac{r_p}{r}\right) + \frac{r_p C_o}{r}\operatorname{erf}\left(\frac{r - r_p}{\sqrt{4Dt}}\right). \tag{37}$$

Since $J_D = -D\frac{\partial C(r,t)}{\partial r}$, the diffusive flux is

$$J_D(r,t) = -\frac{C_o D r_p}{r^2}\left[\operatorname{erfc}[\delta] + \frac{r}{\sqrt{\pi Dt}}\, e^{-\delta^2}\right], \tag{38}$$

where $\delta = \delta(r, t) \equiv (r - r_p)/\sqrt{4Dt}$.

We can now determine at which location $R^*(t)$ these two fluxes are equal by solving the relation $J_E(R^*, t) = J_D(R^*, t)$. To simplify, we define the scaled variables $\hat{r} = r/\lambda_e$ and $\hat{t} = t/\tau_\lambda$, and we drop numerical factors of order unity and neglect r_p in δ since $R^* \gg r_p$. The flux equality then reduces to

$$\lambda_e\left[1 + \frac{\hat{t}}{\hat{r}^3}\right]^{2/3} = r_p\left[\operatorname{erfc}\left(\frac{\hat{r}}{\sqrt{\hat{t}}}\right) + \frac{\hat{r}}{\sqrt{\hat{t}}}\, e^{-\hat{r}^2/\hat{t}}\right]. \tag{39}$$

In terms of these rescaled variables, the solution derived in the Introduction is simply equivalent to a capture radius $\hat{r} = 1$ with a cleanup time $\hat{t} = 1$. For long times, the solution of this equation is $\hat{r}^* = \hat{t}^{1/3}(\lambda_e/r_p)^{1/2}$. Returning to our previous variables, this becomes

$$R^*(t) \approx \lambda_e \times [t/\tau_\lambda]^{1/3} \times (\lambda_e/r_p)^{1/2}. \tag{40}$$

The additional $(\lambda_e/r_p)^{1/2}$ term increases the value found in Eq. (29) by a factor ≈16 for our numerical example. In 2D, a similar calculation gives

$$R^*_{2d} \approx \lambda_e \times [t/\tau_\lambda]^{1/6}; \tag{41}$$

the capture radius is thus predicted to increase more slowly in 2D and to reach λ_e at $t = \tau_\lambda$.

C. Reinterpreting the Péclet approach

The approach described in the Introduction [Eqs. (6) and (7)] used simple scaling arguments and compared two capture times for a single particle. In contrast, Eq. (40) gives the corresponding result when we consider particle fluxes, while Eq. (29) considers single particle dynamics but takes into account the small size of the target.

However, there is yet another way to use a Péclet approach. Given a hemispherical region of radius R^*, the time needed for the electric forces to empty it is given by Eq. (13): $\tau_E(R^*, 0) = R^{*3}/3D\lambda_e$. To refill it by diffusion requires a time $\sim R^{*2}/D$ [this is similar to the fluorescence recovery after photobleaching (FRAP) of a spherical patch[38]]. These two times are equal at distance $R^* \approx \lambda_e$ and time $\approx\tau_\lambda$. This approach does not include the size of the target, but it may be misleading since the concentration outside the capture zone decreases with time, making refilling less efficient [this is why R^* increases with time in Eq. (40)].

IV. LATTICE MONTE CARLO: METHODS

We now use two-dimensional (2D) **L**attice **M**onte **C**arlo (LMC) simulations to study the capture of particles in the system shown in Fig. 1 and to investigate different ways to defining a capture radius or length scale (we chose 2D instead of 3D in order to be able to simulate larger systems and longer times; given the symmetry around the axis normal to the plane, we can easily infer 3D dynamics from our results). Since only the capture process is of interest here, the *trans* side of the system is not part of the simulation.

A. The simulation algorithm

At each time step, the particle can move over a distance $\pm a$ (corresponding to the lattice step) in either the x or the z direction on the square lattice or can remain at its initial position. The lattice step (and thus the "size" of the pointlike particle) is $a = |z_{i\pm1} - z_i| = |x_{j\pm1} - x_j| = r_p/5$.

The trajectory of a Brownian particle can be discretized as a series of jumps on a lattice. For the current problem, building a LMC algorithm requires special care since the electric field is along a Cartesian axis and varies considerably between lattice sites. Moreover, as shown in Refs. 39, LMC algorithms often fail to give the right diffusion coefficient if the system is highly biased. Our approach will be to combine two 1D LMC algorithms (one for each Cartesian direction) into one and then select the time step so that the resulting 2D LMC is reliable. In 1D, a particle on site i (local potential energy Ψ_i) "jumps" to site $i \pm 1$ at a rate

$$R_\pm = p_\pm/\tau_\pm, \tag{42}$$

where $p_\pm$ is the probability for the particle to reach site $i \pm 1$ before site $i \mp 1$ and $\tau_\pm$ is the mean duration of this event. These probabilities and time durations are functions of the energy differences $\delta\Psi_\pm = \Psi_{i\pm1} - \Psi_i$ and are given by Eqs. (3.20)–(3.22) in Ref. 40 [note the typo: e^{u_-} must be replaced by $e^{u_\mp}$ in Eq. (3.22)] with $u_\pm = \delta\Psi_\pm/2$ and $\tau_B = a^2/2D$. The probability of jumping from site i to site $i \pm 1$ during a LMC time step δt is thus $P^i_\pm = R^i_\pm \times \delta t$. The time step must satisfy the condition $\delta t \le \delta t_c \equiv min[1/(R^i_+ + R^i_-)]_i$ to ensure that $P^i_+ + P^i_- \le 1 \ \forall i$; this implies a finite probability P^i_o of not jumping during a time step on most sites i.

Using Eq. (9), we can write the particle's dimensionless potential energy at an oblate distance ξ from the pore as

$$\Psi(\xi) = \frac{QV(\xi)}{k_B T} = \frac{\lambda_e}{r_p}\arctan[\sinh(\xi)]. \tag{43}$$

In 2D, we use the same equations for each Cartesian direction, but the constrain on the time step now reads

$$\delta t_c = min\left[\frac{1}{\sum_{4_i} R^i}\right]_i, \tag{44}$$

where 4_i means that the sum is over the 4 possible jump directions from site i.

This LMC algorithm can be used in two different ways:

(I) To study the motion of a given particle: Using the probabilities described above, random numbers are generated at each time step to choose whether the particle will jump over a length $\pm a$ (the lattice step) in either the x or z direction or stay put. This is the method used for estimates 1 and 2 in Sec. V.

(II) To follow a population of particles on the lattice: The time evolution of the particle concentration can be studied by iterating the master equation. The concentration $m_{x,z}^{j+1}$ at position x, z and time step $j+1$ reads

$$m_{x,z}^{j+1} = P_{[x,z-1\to z]} m_{x,z-1}^{j} + P_{[x,z+1\to z]} m_{x,z+1}^{j} + P_{[x-1\to x,z]} m_{x-1,z}^{j} + P_{[x+1\to x,z]} m_{x+1,z}^{j} + P_{[o]} m_{x,z}^{j}, \tag{45}$$

where x, z, j are integers and $P_{[o]}$ is the probability of not jumping. This was used in estimates 3 and 4 below.

V. SIMULATION RESULTS AND ANALYSIS

In this section, we present four different ways to analyze simulation data and define a length scale describing the capture process. The first two use single particle dynamics (allowing us to reach longer times), the third one examines the time-dependence of the capture rate, while the last one uses the concentration profile near the pore.

A. Estimate 1: 50% probability of capture

Let $P(r, t)$ be the probability for a particle initially at radial position r to reach the pore in a time $\leq t$. Obviously, $P(r, t)$ increases with t and decreases if the initial position r is further from the pore. A straightforward length scale that can characterize the capture process is the distance $r = R^*_{1/2}$ at which $P = 1/2$. Since $R^*_{1/2}$ is a function of time, we can use the solution of $P(R^*_{1/2}, t_{exp}) = 1/2$ for a given experiment of duration t_{exp}.

Figure 2 shows the time evolution of $R^*_{1/2}(t)$ in our 2D simulations for different field intensities (i.e., different electrostatic lengths λ_e) over a wide range of time scales; since there is a small angular dependence when Eq. (43) is used, all initial positions are chosen (for simplicity) to be along the vertical axis going through the pore center (this has a small effect at short times). The simulation box is of size $R_b = 10^3\ \lambda_e$, and its walls are reflecting: we thus have a finite loading box with no addition of analyte during the run. The y-axis is rescaled by the nominal capture radius λ_e and the x-axis by the time τ_λ. We first note that $R^*_{1/2}(t = \tau_\lambda) \approx \lambda_e$ (the empty circle), in agreement with both Eqs. (29) and (41). Since $R^*_{1/2}$ keeps increasing beyond that point, λ_e is not sufficient to describe the nanopore capture properties. The data collapse for $t > \tau_\lambda$ is expected from our theoretical work.

In order to investigate the various regimes, the slope of the data is given in the inset; note that the slope gives the local time exponent α if we assume a power law scaling $R^*_{1/2}(t) \sim t^\alpha$. The pore region cleanup time is given by Eq. (16); for times shorter than this, the distances are comparable to the pore size r_p itself and since the field is fairly flat near the pore, the slope α approaches unity. We then have a regime where $R^*_{1/2}(t) \sim t^{1/3}$, as predicted by Eq. (29); the width of this regime increases for higher fields and basically vanishes at a low field. There is no $t^{1/6}$ regime, which rules out Eq. (41). The exponent slowly increases toward $\alpha = 1/2$ at longer times, a value consistent with a diffusion-limited process. Equation (32) predicted that this latter regime would exist for distances larger than $R^*_{1/2}/\lambda_e \sim (R_b/\lambda_e)^{2/3} \approx 100$, consistent with our data. It is important to note that this transition is *not* expected in 3D (for these boundary conditions) because theory then predicts that $R^* > R_b$—see Eq. (27).

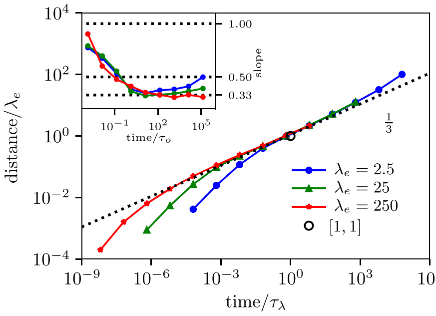

FIG. 2. Log-log plot of the capture length scale $R^*_{1/2}(t)$ (in units of λ_e) vs time t (in units of τ_λ) for three electrostatic lengths λ_e. The empty circle marks the capture radius and time defined in Eqs. (8) and (14). An ensemble of 5000 particles were placed at various distances from the pore center, and the simulation was carried out for different time durations; the y-axis shows the distance at which 50% of the particles were captured in the given time. The dashed line has a slope of 1/3. Inset: local slope vs time t (in units of τ_o). The key values of 1, 1/2, and 1/3 are marked by horizontal lines.

We conclude that $R^*_{1/2}$ provides a good estimate of the revised Péclet capture radius and that the latter increases well beyond the nominal value λ_e during a run.

B. Estimate 2: Time reversal and particle escape

One way to find a change in dynamics and estimate the corresponding length scale is to study the inverse process. Here, we reverse the polarity of the electric field and let particles move away from the center of the pore (we now use an infinite box size). It is more efficient to track particles escape trajectories since we do not have to wait for diffusion to bring them into the capture zone. The mean displacement at time t can be seen as a characteristic length scale for capture. The results shown in Fig. 3 agree with the trends seen in Fig. 2, and the data sets again collapse past the transient regime. The "inverse capture radius" R^*_i, as defined here, increases during the experiment, and $R^*_i \approx \lambda_e$ at $t = \tau_\lambda$ here as well. These results thus imply that $R^*_{1/2} \propto R^*_i$ and confirm the existence of the three temporal regimes observed with estimate 1.

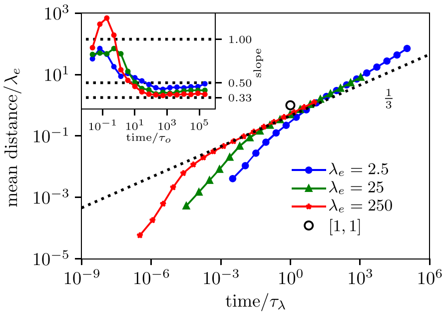

FIG. 3. Log-log plot of the mean distance R_i^* (in units of λ_e) reached by the particles at time *t* (in units of τ_λ) when the field polarity is reversed. An ensemble of 5000 particles were initially placed at the pore center, and mean displacements were computed at different times. The dashed line has a slope of 1/3. Inset: the local slope vs time *t* (in units of τ_o). The key values of 1, 1/2, and 1/3 are marked by horizontal lines.

C. Estimate 3: The capture rate

As discussed previously, the initial mean capture rate $\overline{\rho}_p$ is predicted to change with time because of the nature of the field very close to the pore (i.e., within a distance ~r_p). More precisely, it is expected to increase with *t* in 3D but to decrease with *t* in 2D. We now use a reservoirlike boundary with a radius $R_r = 10^4\ r_p \gg \lambda_e$ in order to keep the concentration constant at $C(R_r, t) = C_o$ and study how the resulting capture rate evolves with time (we chose R_r, so the region close to $r = R_r$ remains essentially undisturbed during the simulation).

Figure 4 shows the time dependence of the pore capture rate $\rho(t)$. As predicted for 2D, $\rho(t)$ decays as $t^{-1/3}$ [see Eq. (24)] after the short time plateau. The latter is predicted to be at $\overline{\rho}_p/DC_o \approx \frac{\pi}{2}\lambda_e/r_p$; our data are in decent agreement with this prediction (except at a low field) even though we did not consider angular effects. We also predicted that $\rho(\tau_\lambda)/DC_o \approx \pi$ in 2D, independent of the field intensity; this explains the collapse of the data around $t = \tau_\lambda$, and the predicted value is in decent agreement with the data (empty circle).

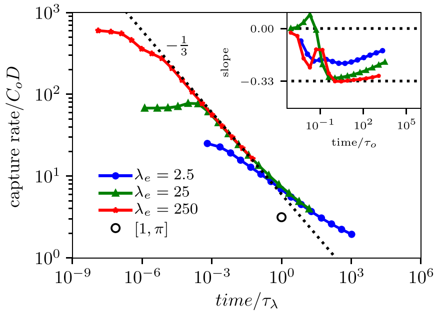

FIG. 4. Log-log plot of the capture rate $\rho(t)$ (in units of C_oD) vs time *t* (in units of τ_λ). The dashed line has a slope of −1/3. Inset: the local slope vs time *t* (in units of τ_o).

We showed in Secs. V A and V B that the $r \sim t^{1/3}$ regime evolves into a $t^{1/2}$ regime at longer time in 2D. If we use $r \sim t^{1/2}$ in Eq. (23), we obtain $N(t) \sim t$, and hence, $\rho = \partial N(t)/\partial t = cst$; the inset of Fig. 4 shows that the data are indeed (slowly) converging toward a plateau regime at long times $t \gg \tau_\lambda$ (and distances $\gg \lambda_e$).

We also predicted a 3D constant capture rate $\rho \approx \overline{\rho}_\lambda(t)$ at long times. The only difference of substance between 2D and 3D is the extra $r(t)$ term in Eq. (19) when compared to Eq. (23). We can thus infer 3D from the product $r(t) \times \rho(t)$ using 2D data. Since we obtained $r(t) \sim t^{1/3}$ and $\rho(t) \sim t^{-1/3}$ in 2D, a 3D simulation would indeed give a constant capture rate for $t > \tau_p$, as observed by Ref. 13.

A characteristic length scale can be estimated from capture rates: since $N(t) = \int_0^t \rho(t')dt'$ molecules have been captured by time *t*, we can use Eq. (23) to obtain the related length scale $R^*_{cap}(t) = \left[\frac{2}{\pi}N(t)/C_o\right]^{1/2}$. In a $\rho(t) \sim t^{-\beta}$ regime, this would give $N(t) \sim t^{1-\beta}$ and hence $R^*_{cap} \sim t^{(1-\beta)/2}$. Since β decreases from 1/3 to ≈0 past the transients in Fig. 4, R^*_{cap} will scale just like $R^*_{1/2}$ and R^*_i for longer time (shown in Figs. 2 and 3).

D. Estimate 4: Quasistatic concentration profiles

Keeping the boundary conditions used for estimate 3, we now study the evolution of 2D concentration profiles (Fig. 5). Not surprisingly, a depletion region forms near the pore (inset) and propagates outward: its width extends well beyond λ_e and continues to grow for times $t \gg \tau_\lambda$. We define the width of the depletion region as the distance between the pore and the position $r = R^*_{90}$ where $C(R^*_{90}) = 0.90\ C_o$. When the concentration profiles are plotted as a function of the rescaled distance r/R^*_{90} (main part of the figure), the curves clearly evolve toward a steady-state distribution at long times.

Figure 6 shows how the width R^*_{90} of the depletion zone, which is also a length scale describing the capture process, increases with time. We again observe a $t^{1/3}$ scaling after the initial transients; for longer times, our data are consistent with a diffusion-limited $t^{1/2}$ regime.

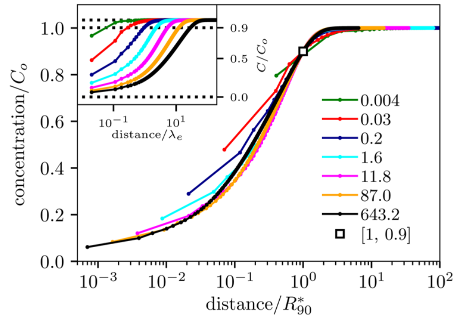

FIG. 5. Concentration vs distance from the pore (scaled by R^*_{90}, the distance at which $C = 0.9\ C_o$) at different times (in units of τ_λ) for $\lambda_e = 2.5\ r_p$. All the curves thus cross at the location of the empty square. The inset shows the concentration at different times vs distance in units of λ_e.

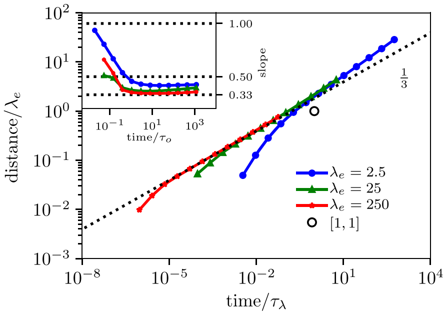

FIG. 6. Log-log plot of the depletion length scale R^*_{90} (in units of λ_e) vs time (in units of τ_λ). The dashed line has a slope of 1/3. Inset: the local slope vs time t (in units of τ_o).

VI. DISCUSSION AND CONCLUSION

The concept of a capture radius R^* that can characterize the capture process has been used in different ways in the literature. In this paper, we have revisited theoretical approaches often employed to define R^*. In particular, we did not work within the framework of a steady-state in order to see how relevant the length scale R^* might be during an experiment. For readability reasons, Table I summarizes the definition of the important length and time scales used in this paper.

Our theoretical approach has been to use the Péclet number as a way to examine the nature of the capture process, thus treating nanopore capture as a separation process. In particular, we examined how the size of the target (i.e., the radius of the nanopore, r_p) can be an integral part of the calculation.

We first calculated the "pure" diffusive and field-driven capture times for a particle in a finite size box with reflective boundary conditions. Our measure of the field intensity is the length scale λ_e, which is the capture radius predicted by previous theories [note that $\lambda_e \neq \lambda_e(r_p)$]. The resulting Péclet number predicts that $R^* \gg \lambda_e$ and even exceeds the box size. However, for realistic experimental times, R^* simply grows as $t^{1/3}$ during the entire experiment (i.e., the capture remains field-driven throughout). A similar calculation in 2D indicates that it might be possible to transition into a diffusion-limited capture regime at long times. We also investigated a flux-based Péclet number using similar arguments. This approach predicted even larger capture radii but similar time-dependence.

In short, our Péclet calculations suggest that the conditions required to reach a diffusion-dominated capture regime might not be achievable in realistic situations: consequently, R^* is simply a moving horizon ($\sim t^{1/3}$) that never reaches a steady state.

To test the various concepts of a capture radius, we introduced a new lattice Monte Carlo scheme to simulate (pointlike) particle dynamics over a wide range of time scales and in the presence of a space-dependent field. The mesh size can be changed to explore finer short-time details or long time asymptotic limits. For instance, we were able to cover up to 7 decades in time with a fine mesh in 2D. Although this methodology can easily be extended to 3D, it would restrict us to rather small systems. This LMC algorithm can be used to look at both populations of particles and single particles with various boundary conditions.

TABLE I. Definition of the different length and time scales used in this paper.

Symbol	Definition
r_p	Pore radius
r_e	Characteristic length of the electrostatic potential outside the pore
λ_e	Traditional definition of the capture radius R^*
R_b	Distance between the outer reflecting boundary and the pore center
R_r	Distance between the outer reservoirlike boundary and the pore center
$R^*_{1/2}$	Estimate no. 1 of the capture radius, defined as the location where the probability of capture is 1/2
R^*_i	Estimate no. 2 of the capture radius, defined as the mean escape distance when the polarity is inverted
R^*_{cap}	Estimate no. 3 of the capture radius, defined using the time dependent capture rate
R^*_{90}	Estimate no. 4 of the capture radius, defined as the width of the depletion zone where the concentration is 90% of bulk
τ_o	Basic unit of time: $\tau_o = r_p^2/D$
τ_{exp}	Duration of an actual experiment
τ_p	Time needed to empty a zone of radius r_p
τ_λ	Time needed to empty a zone of radius λ_e

We introduced four different ways (which were based on the probability of capture, escape trajectories, capture rate, and concentration profiles) to define a length scale related to the capture performance of a nanopore from the 2D simulation data, and we compared them to the theoretical approaches. Figure 7 shows a compact view of our LMC data for the various time-dependent length scales $R^*(t)$. The short time behavior of R^* depends on the type of measurement made and the details of the simulation protocol; nevertheless, it is clear that the fact that the field strongly deviates from the pointlike approximation for distances $r < r_p$ leads to strong (but experimentally insignificant) short-time effects. For intermediate times, all estimates of R^* increase like $t^{1/3}$ (since the time axis has been rescaled by $t^{1/3}$, this shows as a plateau on the figure). For much longer times, we observe a transition to a $t^{1/2}$ regime, an indication that we have reached the diffusion-limited regime. This latter regime is occurring for distances much larger than the nominal capture radius λ_e and for times much larger than the cleanup time τ_λ. This is all consistent with our theoretical derivations. In particular, nothing special is observed at τ_λ or when the depletion region reaches a distance λ_e. Except for the capture rate ρ, our 2D simulation results apply directly to a 3D system. The capture rate is predicted and observed to decrease very rapidly in 2D to reach a constant value only when (and if) the diffusion-limited capture regime is reached. In contrast, ρ is going to quickly increase (because of the nature of the field near the pore) and reach a time-independent value in 3D. Therefore, we must conclude that λ_e is simply a useful and natural way to measure the field intensity [for instance, the steady-state capture rate is linearly proportional to λ_e—see Eq. (17)]. Our revisited Péclet calculation indicates that one should observe a $R^*(t) \sim t^{1/3}$ scaling law well beyond λ_e. However, this is actually a fairly slow growth process: in other words, the corresponding depletion region should remain in the ~10 μm range during a typical experiment, consistent with the results of Chen *et al.*[24]

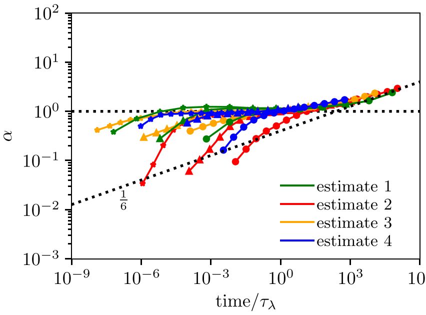

FIG. 7. The four different length scales (or capture radii R^*) introduced in Sec. V vs time (in units of τ_λ). The capture radii are rescaled by $R^*(t = \tau_\lambda, \lambda_e = 25)$ for each separate data set. Since the time evolution of the intermediate regime scales like $t^{1/3}$, the y-axis was further divided by $(t/\tau_\lambda)^{1/3}$ (hence the plateau for intermediate times). The resulting y-axis is thus $\alpha = (R^*(t)/R^*(\tau_{25}))/(t/\tau_\lambda)^{1/3}$. The dashed line with a slope $1/6 = 1/2 - 1/3$ corresponds to the $t^{1/2}$ diffusion-limited regime expected at long times. Three different field intensities are shown for each of the four definitions of R^*.

A real-life system may differ from the ideal conditions used here in different ways. For instance, we studied pointlike particles in the absence of EOF or hydrodynamic interactions with the walls. More importantly, such models assume that the system is closed, uniform, and isolated (no flux through the system or thermal gradients): diffusion and field-driven motion are not necessarily the only two components to consider in a more general situation even in the absence of EOF. However, a more complete theory that would include some of these effects for a particular system would nevertheless include the length and time scales derived here. Perhaps of more interest is the connection between the analyte transport properties (mobility and diffusivity), the local field intensity, and the analyte conformation and/or orientation. In the case of a flexible analyte such as DNA, for example, the molecule may deform in the gradient (moreover, its conformational entropy may act as a barrier). Similarly, if the analyte is not spherical, the field gradient will lead to orientation and thus to a position dependent diffusion coefficient $D(r)$; this latter case will be treated in a separate paper.

ACKNOWLEDGMENTS

G.W.S. acknowledges the support of both the University of Ottawa and the Natural Sciences and Engineering Research Council of Canada (NSERC), Funding Reference No. RGPIN/046434-2013. L.Q. was supported by the Chinese Scholarship Council and the University of Ottawa. The authors wish to thank Vincent Tabard-Cossa, David Sean, and Kyle Briggs for fruitful discussions.

APPENDIX A: THE ELECTROSTATIC FIELD

The field outside the pore is often modeled using the pointlike approximation,[15,27,28] which greatly simplifies analytical calculations; for a pore of radius r_p and length l, the corresponding potential $V(r)$ is the second equation in the Introduction. The part of the total potential gradient ΔV that is relevant for capture depends on the ratio of the access (ac) and channel (ch) resistances. The potential drop from infinity to the pore entrance is[32,41]

$$\delta V = \Delta V \times \frac{R_{ac}}{R_{ch} + 2R_{ac}} = \Delta V \times \frac{\pi r_p}{4l + 2\pi r_p}, \qquad \text{(A1)}$$

where the resistances are $R_{ac} = 1/4r_p\sigma$ and $R_{ch} = l/\pi r_p^2\sigma$ (σ is the conductivity of the solution). If we take the potential to be zero at infinity, we obtain[15,27,28]

$$V(r) = \frac{1}{2\pi\sigma r}\frac{\delta V}{R_{ac}} = \frac{2r_p}{\pi r}\delta V = \Delta V \frac{r_e}{r}, \qquad \text{(A2)}$$

where $r_e = r_p/(\frac{2l}{r_p} + \pi)$ is the characteristic length of the electrostatic potential outside the pore. The spherically symmetric electric field is then given by

$$\vec{E}(r) = -\Delta V \frac{r_e}{r^2}\hat{r}. \qquad \text{(A3)}$$

Alternatively, we can use the exact solution of Laplace's equation in oblate spherical coordinates,[22,32]

$$V(\xi,\eta,\phi) = \Delta V \frac{r_e}{r_p} \arctan[\sinh(\xi)], \tag{A4}$$

where $\xi \in (-\infty, +\infty)$, $\eta \in [0, \pi]$, and $\phi \in [0, 2\pi]$. The potential only depends on ξ (here in units of r_p). The electric field can then be written as

$$\vec{E}(\xi,\eta) = -\frac{\Delta V r_e}{r_p^2 \cosh\xi \sqrt{\sinh^2\xi + \sin^2\eta}} \hat{\xi}. \tag{A5}$$

Expanding Eq. (A5) for large oblate distances ($\xi \gg 1$) gives

$$\vec{E}^{\infty} \approx -\frac{\Delta V r_e}{r_p^2 \cosh\xi \sinh\xi} \hat{\xi} \approx -\frac{\Delta V r_e}{r^2} \hat{r}, \tag{A6}$$

in agreement with (A3).

Close to the pore ($\xi \to 0$), Eq. (A5) reduces to

$$\vec{E}^{0} \approx -\frac{\Delta V\, r_e}{r_p^2} \times |\csc(\eta)| \times \left[1 - \frac{\xi^2}{2}\left(1 + \csc^2(\eta)\right)\right] \hat{\xi}, \tag{A7}$$

where $\eta \in [0, \pi]$. The field is thus flat when $\xi < \xi^*(\eta) = \sqrt{2/(1+\csc^2(\eta))}$. The critical length is $\xi^*(\pi/2) = 1$ (or $r = r_p$) in the vertical direction and $\xi^*(0) = 0$ along the wall (the field diverges at the pore edges).

APPENDIX B: THE MEAN FIRST PASSAGE TIME

We consider a particle initially placed between a small absorbing spherical target (at $r = r_D$) and a large reflecting spherical wall (at $r = R_b$). Its mean diffusive absorption time τ_D if it starts at radial position $R_b > r > r_D$ can be obtained analytically[36] from the equation

$$\frac{D}{r^{d-1}} \frac{\mathrm{d}}{\mathrm{d}r}\left[r^{d-1} \frac{\mathrm{d}\tau_D(r, r_D)}{\mathrm{d}r}\right] = -1, \tag{B1}$$

with the boundary conditions

$$[\tau_D(r, r_D)]_{r=r_D} = 0; \ \left[\tfrac{\mathrm{d}}{\mathrm{d}r}\tau_D(r, r_D)\right]_{r=R_b} = 0, \tag{B2}$$

where d is the dimensionality. In 2D, we obtain

$$\tau_D(r, r_D) = \frac{R_b^2}{4D}\left[2\ln\left(\frac{r}{r_D}\right) + \left(\frac{r_D^2 - r^2}{R_b^2}\right)\right], \tag{B3}$$

while in 3D, we recover

$$\tau_D(r, r_D) = \frac{R_b^2}{6D}\left[\frac{2R_b}{r_D}\left(1 - \frac{r_D}{r}\right) + \left(\frac{r_D^2 - r^2}{R_b^2}\right)\right]. \tag{B4}$$

As expected, τ_D diverges in both cases if the target size $r_D \to 0$, hence the need to use a finite value for r_D, such as $r_D = r_p$.

REFERENCES

[1] J. J. Kasianowicz, E. Brandin, D. Branton, and D. W. Deamer, "Characterization of individual polynucleotide molecules using a membrane channel," Proc. Natl. Acad. Sci. U. S. A. **93**, 13770–13773 (1996).

[2] A. Meller, L. Nivon, and D. Branton, "Voltage-driven DNA translocations through a nanopore," Phys. Rev. Lett. **86**, 3435–3438 (2001).

[3] S. Lee, Y. Zhang, H. S. White, C. C. Harrell, and C. R. Martin, "Electrophoretic capture and detection of nanoparticles at the opening of a membrane pore using scanning electrochemical microscopy," Anal. Chem. **76**, 6108–6115 (2004).

[4] D. Fologea, J. Uplinger, B. Thomas, D. S. McNabb, and J. Li, "Slowing DNA translocation in a solid-state nanopore," Nano Lett. **5**, 1734–1737 (2005).

[5] Y. He, M. Tsutsui, C. Fan, M. Taniguchi, and T. Kawai, "Controlling DNA translocation through gate modulation of nanopore wall surface charges," ACS Nano **5**, 5509–5518 (2011).

[6] M. Pastoriza-Gallego, L. Rabah, G. Gibrat, B. Thiebot, F. G. van der Goot, L. Auvray, J.-M. Betton, and J. Pelta, "Dynamics of unfolded protein transport through an aerolysin pore," J. Am. Chem. Soc. **133**, 2923–2931 (2011).

[7] M. Mihovilovic, N. Hagerty, and D. Stein, "Statistics of DNA capture by a solid-state nanopore," Phys. Rev. Lett. **110**, 028102 (2013).

[8] S. Mirigian, Y. Wang, and M. Muthukumar, "Translocation of a heterogeneous polymer," J. Chem. Phys. **137**, 064904 (2012).

[9] V. V. Palyulin, T. Ala-Nissila, and R. Metzler, "Polymer translocation: The first two decades and the recent diversification," Soft Matter **10**, 9016–9037 (2014).

[10] K. Briggs, G. Madejski, M. Magill, K. Kastritis, H. W. de Haan, J. L. McGrath, and V. Tabard-Cossa, "DNA translocations through nanopores under nanoscale preconfinement," Nano Lett. **18**, 660–668 (2018).

[11] E. Beamish, V. Tabard-Cossa, and M. Godin, "Identifying structure in short DNA scaffolds using solid-state nanopores," ACS Sens. **2**, 1814–1820 (2017).

[12] D. Sean and G. W. Slater, "Langevin dynamcis simulations of driven polymer translocation into a cross-linked gel," Electrophoresis **38**, 653–658 (2017).

[13] M. Charron, K. Briggs, S. King, M. Waugh, and V. Tabard-Cossa, "Precise DNA concentration measurements with nanopores by controlled counting," Anal. Chem. **91**, 12228–12237 (2019).

[14] C. T. A. Wong and M. Muthukumar, "Polymer capture by electro-osmotic flow of oppositely charged nanopores," J. Chem. Phys. **126**, 164903 (2007).

[15] M. Wanunu, W. Morrison, Y. Rabin, A. Y. Grosberg, and A. Meller, "Electrostatic focusing of unlabelled DNA into nanoscale pores using a salt gradient," Nat. Nanotechnol. **5**, 160–165 (2010).

[16] B.-j. Jeon and M. Muthukumar, "Polymer capture by α-hemolysin pore upon salt concentration gradient," J. Chem. Phys. **140**, 015101 (2014).

[17] M. M. Hatlo, D. Panja, and R. van Roij, "Translocation of DNA molecules through nanopores with salt gradients: The role of osmotic flow," Phys. Rev. Lett. **107**, 068101 (2011).

[18] B.-j. Jeon and M. Muthukumar, "Electrostatic control of polymer translocation speed through α-hemolysin protein pore," Macromolecules **49**, 9132–9138 (2016).

[19] M. Muthukumar, "Theory of capture rate in polymer translocation," J. Chem. Phys. **132**, 195101 (2010).

[20] H. H. Katkar and M. Muthukumar, "Role of non-equilibrium conformations on driven polymer translocation," J. Chem. Phys. **148**, 024903 (2018).

[21] S. C. Vollmer and H. W. de Haan, "Translocation is a nonequilibrium process at all stages: Simulating the capture and translocation of a polymer by a nanopore," J. Chem. Phys. **145**, 154902 (2016).

[22] F. Farahpour, A. Maleknejad, F. Varnik, and M. R. Ejtehadi, "Chain deformation in translocation phenomena," Soft Matter **9**, 2750–2759 (2013).

[23] M. Waugh, A. Carlsen, D. Sean, G. W. Slater, K. Briggs, H. Kwok, and V. Tabard-Cossa, "Interfacing solid-state nanopores with gel media to slow DNA translocations," Electrophoresis **36**, 1759–1767 (2015).

[24] P. Chen, J. Gu, E. Brandin, Y.-R. Kim, Q. Wang, and D. Branton, "Probing single DNA molecule transport using fabricated nanopores," Nano Lett. **4**, 2293–2298 (2004).

[25] J. Nakane, M. Akeson, and A. Marziali, "Evaluation of nanopores as candidates for electronic analyte detection," Electrophoresis **23**, 2592–2601 (2002).

[26] M. Gershow and J. A. Golovchenko, "Recapturing and trapping single molecules with a solid-state nanopore," Nat. Nanotechnol. **2**, 775–779 (2007).

[27] A. Y. Grosberg and Y. Rabin, "DNA capture into a nanopore: Interplay of diffusion and electrohydrodynamics," J. Chem. Phys. **133**, 165102 (2010).

[28] S. K. Nomidis, J. Hooyberghs, G. Maglia, and E. Carlon, "DNA capture into the ClyA nanopore: Diffusion-limited versus reaction-limited processes," J. Phys.: Condens. Matter **30**, 304001 (2018).

[29] P. Rowghanian and A. Y. Grosberg, "Electrophoretic capture of a DNA chain into a nanopore," Phys. Rev. E **87**, 042722 (2013).

[30] D. Long, J.-L. Viovy, and A. Ajdari, "Simultaneous action of electric fields and nonelectric forces on a polyelectrolyte: Motion and deformation," Phys. Rev. Lett. **76**, 3858–3861 (1996).

[31] A. E. Nkodo, J. M. Garnier, B. Tinland, H. Ren, C. Desruisseaux, L. C. McCormick, G. Drouin, and G. W. Slater, "Diffusion coefficient of DNA molecules during free solution electrophoresis," Electrophoresis **22**, 2424–2432 (2001).

[32] S. W. Kowalczyk, A. Y. Grosberg, Y. Rabin, and C. Dekker, "Modeling the conductance and DNA blockade of solid-state nanopores," Nanotechnology **22**, 315101 (2011).

[33] B. J. Kirby, *Micro- and Nanoscale Fluid Mechanics: Transport in Microfluidic Devices* (Cambridge University Press, 2010).

[34] S. Redner, *A Guide to First-Passage Processes* (Cambridge University Press, Cambridge, 2001).

[35] H. C. Berg, *Random Walks in Biology* (Princeton University Press, Princeton, 1993).

[36] A. Szabo, K. Schulten, and Z. Schulten, "First passage time approach to diffusion controlled reactions," J. Chem. Phys. **72**, 4350–4357 (1980).

[37] P. C. Bressloff, *Stochastic Processes in Cell Biology*, Interdisciplinary Applied Mathematics Vol. 410 (Springer International Publishing, Cham, 2014).

[38] M. J. Saxton, "Anomalous subdiffusion in fluorescence photobleaching recovery: A Monte Carlo study," Biophys. J. **81**, 2226–2240 (2001).

[39] M. G. Gauthier and G. W. Slater, "Building reliable lattice Monte Carlo models for real drift and diffusion problems," Phys. Rev. E **70**, 015103 (2004).

[40] S. Hubert, "Theoretical study of polymers: Flow-induced deformation in nanochannels and reptation dynamics in heterogeneous gels," Ph.D. thesis, University of Ottawa, Canada, 2004.

[41] J. E. Hall, "Access resistance of a small circular pore," J. Gen. Physiol. **66**, 531–532 (1975).

5

An efficient Kinetic Monte Carlo to study analyte capture by a nanopore : transients, boundary conditions and time-dependent fields

Reproduced from :
Qiao, Le, Maxime Ignacio, and Gary W. Slater,
Phys. Chem. Chem. Phys., 2021, 23, 1489-1499 ;
https ://doi.org/10.1039/D0CP03638B,
with the permission of RSC Publishing

PCCP

PAPER

Cite this: *Phys. Chem. Chem. Phys.*, 2021, **23**, 1489

An efficient kinetic Monte Carlo to study analyte capture by a nanopore: transients, boundary conditions and time-dependent fields

Le Qiao, Maxime Ignacio and Gary W. Slater *

To better understand the capture process by a nanopore, we introduce an efficient Kinetic Monte Carlo (KMC) algorithm that can simulate long times and large system sizes by mapping the dynamic of a point-like particle in a 3D spherically symmetric system onto the 1D biased random walk. Our algorithm recovers the steady-state analytical solution and allows us to study time-dependent processes such as transients. Simulation results show that the steady-state depletion zone near pore is barely larger than the pore radius and narrows at higher field intensities; as a result, the time to reach steady-state is much smaller than the time required to empty a zone of the size of the capture radius λ_e. When the sample reservoir has a finite size, a second depletion region propagates inward from the outer wall, and the capture rate starts decreasing when it reaches the capture radius λ_e. We also note that the flatness of the electric field near the pore, which is often neglected, induces a traffic jam that can increase the transient time by several orders of magnitude. Finally, we propose a new proof-of-concept scheme to separate two analytes of the same mobility but different diffusion coefficients using time-varying fields.

Received 8th July 2020,
Accepted 11th December 2020

DOI: 10.1039/d0cp03638b

rsc.li/pccp

1 Introduction

Nanopore sensing based on voltage-driven translocation is a hot topic due to its potential applications for the analysis and detection of biomolecules.[1–9] In short, an electric field is applied across a nanopore to electrophoretically capture and translocate charged analytes like DNA, RNA and proteins. Useful information about the analytes (*i.e.*, structure, type, length, *etc.*) can be obtained by analyzing ionic current modulations during the threading process. With more sophisticated nanopore fabrication technologies[8–12] and growing understanding of the mechanisms controlling translocation,[13–18] numerous novel systems have been designed to enhance performance and facilitate new applications.[1–4,19–22] However, several aspects of the capture process are still poorly understood and difficult to observe directly, such as the depletion zone,[23,24] the capture radius,[24–30] non-equilibrium dynamics[30–34] and molecule–pore interactions.[35] High capture rates and large capture zones remain the most important criteria for an ideal (DC-field) translocation setup. Therefore, clarifying those aspects is essential to provide guidance for more precise control and better design of capture devices. Indeed, these goals have motivated the development of theoretical approaches and simulation models to study the interplay between diffusion and electrostatic forces during capture.[24–36] However, most of these theoretical studies focus solely on steady-state quantities while using the point-charge approximation for the field near the pore. We previously studied the time dependence of the capture process with lattice Monte Carlo simulations and discussed the nature of the capture radius for point-like particles.[25] We also examined the impact of field-driven orientation on the capture of rod-like molecules using Langevin Dynamic (LD) simulations.[33] Unfortunately, these previous algorithms and approaches do not allow us to easily study large 3D systems over long periods of time in the presence of time-varying fields and complex boundary conditions.

Our main goal is thus to introduce a new and flexible Kinetic Monte Carlo (KMC) algorithm that can efficiently study large drift-diffusion problems under a wide variety of conditions. We do this by mapping (or projecting) the dynamics of a point-like particle in d-dimensions onto a 1D biased random walk. This projection allows us to use a smaller lattice sizes and/or larger systems, in order to investigate short-time transients, the approach to steady state, the impact of time-dependent fields, and the long-time effect of finite size boundary conditions. As an example, we use this new tool to study the impact of realistic field lines near the pore as well as a novel idea to modify the relative concentration of co-migrating analytes in a mixture.

This paper is organized as follows: we first review the basic theoretical considerations of the capture problem and introduce the relevant time/length scales. Section 3 then describes the mapping from 3D to 1D including the corresponding KMC algorithm and the related boundary conditions. In the result

---

Department of Physics, University of Ottawa, Ottawa, Ontario K1N 6N5, Canada. E-mail: gslater@uottawa.ca

Section 4, we first test our algorithm with the time-dependent concentration profiles and capture rates for the classical case of diffusion-limited absorption by a sphere. We then add the electric field in order to study nanopore capture in both finite and infinite systems. We also examine the reverse process of escape under opposite polarity conditions. Finally, we propose and briefly test a new pulsed-field concept that could separate a binary mixture in Section 5. We conclude the paper in Section 6 with a discussion of our main results, especially the impact of the flat field near the pore, and the potential applications of time-varying electric fields.

2 Basic theoretical elements

As discussed in the Introduction, we assume spherical symmetry in the following. The drift-diffusion equation for the (point-like) analyte concentration $C(r,t)$ in three dimensions and in spherical coordinates is given by[24,28]

$$\frac{\partial C(r,t)}{\partial t} = \frac{D}{r^2}\frac{\partial}{\partial r}\left[r^2\left(\frac{\partial C(r,t)}{\partial r} + \frac{C(r,t)}{k_\mathrm{B}T}\frac{\partial U_\mathrm{e}}{\partial r}\right)\right], \qquad (1)$$

where D is its diffusion coefficient and $U_\mathrm{e}(r)$ is the electrostatic potential energy at radial position r.

Theoretical studies of analyte capture generally use the point-charge field (PCF) approximation for the applied field[24–30,37] because it conserves the spherical symmetry and is quite accurate for distances much larger than pore radius r_p. The potential corresponding to the PCF can be written as

$$U_\mathrm{e}(r) = U_\mathrm{PCF}(r) = \psi_\mathrm{o}\frac{r_\mathrm{e}}{r}, \qquad (2)$$

where $\psi_\mathrm{o} = Q\Delta V$ is the drop in electrostatic energy of a particle of charge Q when a voltage difference ΔV is applied across the system, and $r_\mathrm{e} = r_\mathrm{p}/(\pi + 2\ell_\mathrm{p}/r_\mathrm{p})$ is the characteristic length[25,28] of the potential outside a pore of radius r_p and length ℓ_p. The relevant electrophoretic charge is $Q = k_\mathrm{B}T\mu/D$, with μ the electrophoretic mobility of the analyte. The field obtained from an exact solution of Laplace's equation[31] will also be tested in our simulations for comparison.

The capture radius λ_e is generally defined as the radial distance at which the analyte's potential energy is equal to $k_\mathrm{B}T$ (see Fig. 1a); in our notation, it is given by

$$\lambda_\mathrm{e} = \frac{\psi_\mathrm{o}}{k_\mathrm{B}T}r_\mathrm{e}. \qquad (3)$$

We use λ_e as a measure of field intensity, the pore radius r_p as the unit of length and $\tau_\mathrm{o} = r_\mathrm{p}^2/D$ as the unit of time.

The field-driven deterministic time[25] to drift from position r_o to $r < r_\mathrm{o}$ (using the PCF) is

$$\tau_\mathrm{E}(r_\mathrm{o}, r) = \frac{r_\mathrm{o}^3 - r^3}{3\lambda_\mathrm{e}D}. \qquad (4)$$

For example, the cleanup time τ_λ needed to empty the capture radius zone λ_e is then

$$\tau_\lambda = \tau_\mathrm{E}(\lambda_\mathrm{e}, 0) = \lambda_\mathrm{e}^2/3D. \qquad (5)$$

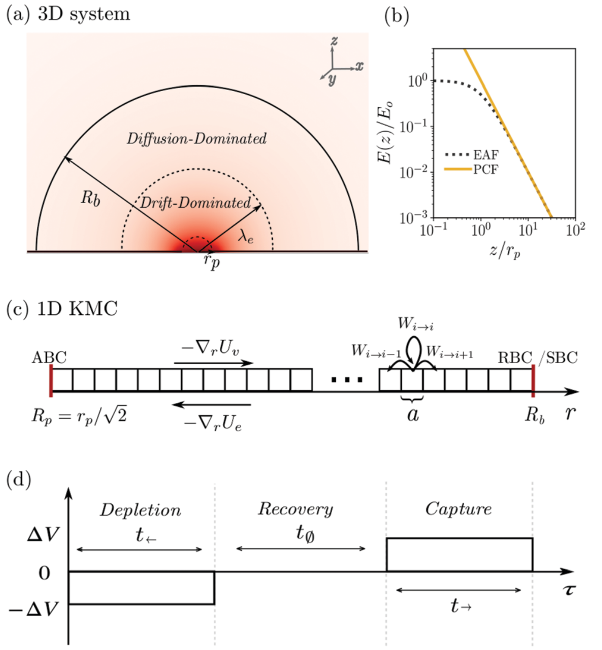

Fig. 1 (a) Schematic view of a nanopore system of size R_b: the background color codes for the electric field strength (higher intensities near the pore). The dashed lines depict a hemisphere of radius r_p (the pore size) and the capture radius λ_e. (b) Comparison between the exact axial (EAF) and point-charge (PCF) field approximations. The y-axis is scaled by the plateau value $E_\mathrm{o} = E_\mathrm{PCF}(r_\mathrm{p})$. (c) The 1D KMC model: $R_\mathrm{p} = r_\mathrm{p}/\sqrt{2}$ is the absorbing boundary; R_b is the reflecting (RBC) or source (SBC) boundary; $-\nabla_r U_\mathrm{v}$ is the entropic force; and $-\nabla_r U_\mathrm{e}$ is the electric force. The jumping probabilities W and lattice step size a are also shown. (d) A schematic description of the pulse sequence. The field is applied in the reverse direction for a duration $t_\leftarrow$ in order empty a region near the nanopore; this is followed by an off period of duration t_ϕ during which the depleted region is partially refilled; finally, the capture period is of duration $t_\rightarrow$.

The mean capture rate during the cleanup time τ_λ is

$$\bar{\rho}_\lambda \approx \frac{2\pi}{3}\lambda_\mathrm{e}^3 C_\mathrm{o}/\tau_\lambda = 2\pi D\lambda_\mathrm{e}C_\mathrm{o}. \qquad (6)$$

Although all of our results will be given in dimensionless units or as ratios, it is sometimes useful to be able to compare to actual experimental systems. In order to do that, we now look at two types of molecules: a short piece of ssDNA and a protein. Note however that this paper is not about either of these two cases: we use these numbers solely to establish the range of values that make sense for λ_e (our simulations will use values between the two limits found below, namely $\lambda_\mathrm{e} \approx 125r_\mathrm{p}$ and $\lambda_\mathrm{e} \approx 22r_\mathrm{p}$).

For a 250 base ssDNA molecule,[38] the relevant parameters are $D \approx 17\ \mu\mathrm{m}^2\ \mathrm{s}^{-1}$ and $\mu \approx 4.1 \times 10^4\ \mu\mathrm{m}^2\ \mathrm{V}^{-1}\ \mathrm{s}^{-1}$, giving $Q \approx 60e$ ($\approx$1/4 of the nominal charge). With a voltage $\Delta V = 400$ mV, the potential energy is $\psi_\mathrm{o}/k_\mathrm{B}T \approx 900$. For a pore of radius $r_\mathrm{p} = 5$ nm and length $\ell_\mathrm{p} = 2r_\mathrm{p}$, we obtain $r_\mathrm{e} = r_\mathrm{p}/(4 + \pi)$ and $\lambda_\mathrm{e} \approx 125r_\mathrm{p} \approx 1\ \mu\mathrm{m}$. The basic time unit is then $\tau_\mathrm{o} = r_\mathrm{p}^2/D \approx 1.5\ \mu\mathrm{s}$.

For a globular protein (for example Lysozyme[39]), the relevant parameters are $D \approx 100\ \mu\mathrm{m}^2\ \mathrm{s}^{-1}$, $\mu \approx 8 \times 10^3\ \mu\mathrm{m}^2\ \mathrm{V}^{-1}\ \mathrm{s}^{-1}$,

$Q \approx 10e$ and hydrodynamic radius $R_h \cong 2$ nm. With a voltage $\Delta V = 400$ mV, the potential energy is $\psi_o/k_BT \approx 160$. For a pore of radius $r_p = 5$ nm and length $\ell_p = 2r_p$, we obtain $r_e = r_p/(4 + \pi)$ and $\lambda_e \approx 22r_p$. The basic time unit is then $\tau_o = r_p^2/D \approx 0.25$ µs.

The stationary solution $\partial C(r,t)/\partial t = 0$ of eqn (1) and (2) with an absorbing boundary $C(R_p,t) = 0$ in an infinite system with $C(r \to \infty,t) = C_o$ is given by[24,28]

$$C(r) = C_o \times \frac{1 - \exp\left(-\lambda_e\left(1/R_p - 1/r\right)\right)}{1 - \exp\left(-\lambda_e/R_p\right)}. \tag{7}$$

The location of the absorbing boundary R_p is somewhat arbitrary since the pore has a finite width, unlike what eqn (2) suggests. Previous papers used $R_p = r_p$, but this overestimates the surface area for capture since an hemisphere of radius r_p has a surface area $2\pi r_p^2$ which is larger than that of the pore, πr_p^2. Instead, we use $R_p = r_p/\sqrt{2}$ to conserve the surface area.

The stationary concentration $C(r)$ rapidly increases from 0 at $r = R_p$ to C_o since we generally have $\lambda_e \gg R_p$. A characteristic length can then be defined from eqn (7): the depletion distance r_d at which $C(r_d)/C_o = 1 - 1/e$ is

$$r_d \approx \frac{R_p}{1 - R_p/\lambda_e}, \quad \lambda_e \gg R_p. \tag{8}$$

The width of the depletion region is thus of order $\sim R_p$. Using eqn (4), the depletion time $\tau_d = \tau_E(r_d,R_p)$ needed to establish the depletion zone r_d is

$$\tau_d \approxeq \frac{R_p{}^4}{\lambda_e{}^2 D} = \frac{1}{4}\left(\frac{r_p}{\lambda_e}\right)^2 \tau_o = \frac{3}{4}\left(\frac{r_p}{\lambda_e}\right)^4 \tau_\lambda. \tag{9}$$

The depletion region is much smaller than λ_e, and its relaxation time is small compared to both τ_λ and τ_o.

3 Simulation methodology

Simulating the capture process in $d = 3$ dimensions would limit us to small systems and short times. In this section, we first show how to transform the 3D problem into a 1D one by replacing volume effects by an entropic force. We then design the corresponding lattice Kinetic Monte Carlo (KMC) algorithm for a point-like particle, and describe the boundary conditions. The mapping process is shown in Fig. 1a and c.

3.1 Fokker–Planck equation

Building a KMC algorithm from a Fokker–Planck equation is simple due to the equivalence with the Master equation formulation. However, the drift-diffusion equation in spherical coordinates in d-dimensions

$$\frac{\partial C(r,t)}{\partial t} = \frac{D}{r^{d-1}}\frac{\partial}{\partial r}\left[r^{d-1}\left(\frac{\partial C(r,t)}{\partial r} + \frac{C(r,t)}{k_B T}\frac{\partial U_e}{\partial r}\right)\right] \tag{10}$$

is not strictly speaking a Fokker Planck equation[40] for $d \neq 1$ as it cannot be written as a conservation equation of the form

$$\frac{\partial C(r,t)}{\partial t} = -\frac{\partial}{\partial r}\left[g(r;d)C(r,t) - D\frac{\partial C(r,t)}{\partial r}\right], \tag{11}$$

where $g(r;d)$ would then be a drift term. This is due to the "centrifugal" term[41] $\frac{D(d-1)}{r}\frac{\partial}{\partial r}C(r,t)$ which appears when we expand the first term of the rhs of eqn (10). Nonetheless, if use the radial concentration

$$\tilde{C}(r,t) = S(r;d)C(r,t), \tag{12}$$

with $S(r;d) = \frac{2\pi^{d/2}}{\Gamma(d/2)}r^{d-1}$ the surface of a d-dimensional sphere, eqn (10) directly reduces to

$$\frac{\partial \tilde{C}(r,t)}{\partial t} = -\frac{\partial J(r,t)}{\partial r}, \tag{13}$$

where the radial flux $J(r,t)$ is given by

$$J(r,t) = -\underbrace{\frac{D}{k_B T}\tilde{C}(r,t)\frac{\mathrm{d}U_v}{\mathrm{d}r}}_{J_V\text{:volume drift}} - \underbrace{\frac{D}{k_B T}\tilde{C}(r,t)\frac{\mathrm{d}U_e}{\mathrm{d}r}}_{J_e\text{:electrostatic drift}} - \underbrace{D\frac{\partial \tilde{C}(r,t)}{\partial r}}_{J_F\text{:Fick's law}}, \tag{14}$$

with $U_v(r) = (1 - d)k_BT\ln(r)$. We thus mapped a spherically symmetric "$d > 1$" drift-diffusion problem onto a 1D process. The 1D projection greatly reduces the amount of memory needed to simulate large $d > 1$ systems. This added a virtual entropic potential $U_v(r)$ and a "volume" drift J_v pushing the particles away from $r = 0$ due to the fact that there is more volume far from the origin. The electrostatic drift J_e attracts the particles toward the center at $r = 0$. Given eqn (14), the stationary distribution $J(r,t) = 0$ satisfies

$$\tilde{C}^s(r) \propto \exp[-U(r)/k_BT], \tag{15}$$

where the effective potential energy is $U = U_v + U_e$.

3.2 Kinetic lattice Monte Carlo algorithm

We consider a 1D system where particles can jump between adjacent lattice sites i and $i + 1$ with probabilities $W_{i\leftrightarrow i+1}$ as shown in Fig. 1c. The latter must satisfy detailed balance in order to insure microscopic reversibility:

$$\tilde{C}^s_i W_{i\to i+1} = \tilde{C}^s_{i+1} W_{i+1\to i}. \tag{16}$$

Using eqn (15), we obtain

$$\frac{W_{i\to i+1}}{W_{i+1\to i}} = \exp(\Delta\varepsilon_i), \tag{17}$$

with $\Delta\varepsilon_i = \varepsilon_{i+1} - \varepsilon_i$ and $\varepsilon_i = U_i/k_BT$. To link these parameters to local dynamics, we use the closure relation

$$W_{i\to i+1} + W_{i+1\to i} = 2D\Delta t/a^2, \tag{18}$$

where a is the lattice step size and Δt is the time step to be used for the simulations. The end result is

$$W_{i\to i+1} = \frac{2D}{a^2} \times \frac{1}{1 + \exp(\Delta\varepsilon_i)} \times \Delta t, \tag{19}$$

$$W_{i+1\to i} = \frac{2D}{a^2} \times \frac{1}{1 + \exp(-\Delta\varepsilon_i)} \times \Delta t. \tag{20}$$

Since the probability of not jumping during a time step, $W_{i\to i} = 1 - W_{i\to i-1} - W_{i\to i+1}$, must be $\geq 0\ \forall i$, we have

$$\Delta t \leq 1/\max[R_{i\to i-1} + R_{i\to i+1}], \tag{21}$$

where the hopping rates are $R_{i\to i\pm1} = W_{i\to i\pm1}/\Delta t$. In order to achieve optimal accuracy, we use a time step $\Delta t = 1/3\Delta t_{\max}$ in our simulations to insure $W_{i\to i} \approx \frac{2}{3}$ everywhere on the lattice, so that the local bias does not affect the diffusion coefficient of the particle.[42–44]

This KMC algorithm can be used in two different ways:

(I) To study the motion of a single particle: as usual, a random number is then generated at each time step to select the next move that will be attempted.

(II) To follow a population of particles: the time evolution of $\tilde{C}$ can be studied by iterating the master equation. The concentration $\tilde{C}_i^{j+1}$ at lattice i and time step $j + 1$ reads

$$\tilde{C}_i^{j+1} = W_{i-1\to i}\tilde{C}_{i-1}^{j} + W_{i+1\to i}\tilde{C}_{i+1}^{j} + W_{i\to i}\tilde{C}_i^{j}, \qquad (22)$$

where i, j are integers.

3.3 Boundary conditions

We use three different types of boundary conditions, as shown in Fig. 1c:

Absorbing boundary conditions to model the capture by the nanopore (ABC): we consider that the ABC is in the center of the lattice site at a distance R_p from the origin; the boundary condition then reads $C(p - 1) = 0$, where $p = R_p/a$. The corresponding master equation is

$$\tilde{C}_p^{j+1} = W_{p+1\to p}\tilde{C}_{p+1}^{j} + W_{p\to p}\tilde{C}_p^{j}. \qquad (23)$$

Reflecting boundary conditions (RBC): in one series of simulations, the walls of the cavity of size R_b are replaced by a RBC placed in the center of the last lattice site, $b = R_b/a$; jumps from $i = b$ to $b + 1$ are rejected (there is no particle flux across the boundary). The corresponding master equation is

$$\tilde{C}_b^{j+1} = W_{b-1\to b}\tilde{C}_{b-1}^{j} + W_{b\to b}\tilde{C}_b^{j} + W_{b\to b+1}\tilde{C}_b^{j}. \qquad (24)$$

Source boundary conditions (SBC): in some simulations, the cavity walls are replaced by a source that mimics an infinite system (or reservoir) at fixed concentration $\tilde{C}(j \geq b) = \tilde{C}_o$. The corresponding master equation is

$$\tilde{C}_b^{j+1} = W_{b-1\to b}\tilde{C}_{b-1}^{j} + W_{b\to b}\tilde{C}_b^{j} + W_{b+1\to b}\tilde{C}_o. \qquad (25)$$

We use a lattice step size $a = R_p/10$ for the simulations in Sections 4.1 and 4.2, and $a = r_p/100$ for the rest of the paper. The simulation time required to achieve steady-state depends on system size, the level of discretization (lattice step size and choice of time step) and field intensity. Let us illustrate this using Test 1 presented in Section 4.1 as an example: the simulations are carried out using Python 3.7 with NumPy 1.19; the typical simulation time for a system described in Section 4.1 is $\approx$30 minutes for 10^5 iterations on a single core processor (2.6 GHz Intel Core i7), corresponding to $t = 636\tau_t$. The figures are plotted using the Matplotlib 3.2.2 package.

3.4 The electric field

We use two different electric field approximations in our simulations: the spherically symmetric field from the point-charge field (PCF) approximation is given by

$$E_{\mathrm{PCF}}(r) = -\Delta V\frac{r_{\mathrm{e}}}{r^2}. \qquad (26)$$

As discussed previously,[25,31,45] the actual electric field is identical to the PCF at large distance ($r > 2r_{\mathrm{p}}$) but flat and not spherically symmetric near the pore (the differences are basically found at small polar angles θ when $r < 2r_{\mathrm{p}}$). Our 1D model is a projection of a spherically symmetric 3D capture system. In order to investigate the impact of the flat field in our 1D KMC simulations, we neglect the small angular dependence of the field near the pore and use the exact field[31] in the vertical direction right above the pore ($\hat{z}$ in Fig. 1b). We call this the Exact Axial Field (EAF) approximation. In 1D simulations, the electric potential at distance r then reads

$$V_{\mathrm{EAF}}(r) = \frac{r_{\mathrm{e}}}{r_p}\Delta V \arctan\left(\frac{r}{r_p}\right), \qquad (27)$$

and the corresponding electric field is

$$E_{\mathrm{EAF}}(r) = -\Delta V\frac{r_{\mathrm{e}}}{{r_p}^2 + r^2}. \qquad (28)$$

Note that $E_{\mathrm{EAF}}(r \gg r_{\mathrm{p}}) \approx E_{\mathrm{PCF}}(r)$, in agreement with the PCF approximation, eqn (26). The field plateaus at $E_{\mathrm{o}} = E_{\mathrm{PCF}}(r_{\mathrm{p}})$ close to the pore, as shown in Fig. 1b.

4 Results

We first test our KMC algorithm for diffusion-limited (no field) absorption by a sphere, both in finite and infinite systems. We then add the electric field to study capture by the nanopore, again in both finite and infinite systems, and simulation results with the PCF and AEF field approximations are compared. We also examine how a particle escapes from the nanopore when the polarity of the electric field is reversed.

4.1 Test 1: diffusion-limited absorption by a sphere with a source boundary

The solution of the diffusion equation with $U_{\mathrm{e}} = 0$ (no external field), an absorbing sphere of radius R_p and the boundary conditions $C(R_p,t) = 0$ and $C(\infty,t) = C_{\mathrm{o}}$ is[41,46]

$$C(r,t) = C_{\mathrm{o}}\left(1 - \frac{R_{\mathrm{p}}}{r}\right) + \frac{R_{\mathrm{p}}C_{\mathrm{o}}}{r}\mathrm{erf}\left[\frac{r - R_{\mathrm{p}}}{\sqrt{4Dt}}\right]. \qquad (29)$$

The last term is negligible in the steady state, $t \to \infty$; the result is then identical to the $\lambda_{\mathrm{e}} \to 0$ limit of eqn (7), as it should. The time dependent capture rate is

$$\rho\left(R_p, t\right) = 4\pi {R_p}^2 D\left.\frac{\partial C}{\partial r}\right|_{R_p} = \rho_{\mathrm{s}}^{\mathrm{o}}\left(1 + \frac{R_p}{\sqrt{\pi D t}}\right). \qquad (30)$$

The capture rate decays to the steady state value $\rho_{\mathrm{s}}^{\mathrm{o}} = \rho(R_p,\infty) = 4\pi D R_p C_{\mathrm{o}}$ with a relaxation time $\tau_t = {R_p}^2/D\pi$. Interestingly, if we replace R_p by λ_{e} in the expression for $\rho_{\mathrm{s}}^{\mathrm{o}}$, we recover the capture rate for a nanopore, eqn (6) (to within a factor of 2 because eqn (6) is for a half-space); the field thus pushes the capture radius from R_p to λ_{e}.

The simulation system of size $R_b = 150R_p$ has a uniform loading $C(r,0) = C_{\mathrm{o}}$ for $R_p < r < R_b$, an absorbing boundary $C(R_p,t) = 0$ and a source boundary $C(R_b,t) = C_{\mathrm{o}}$ (in order to mimic

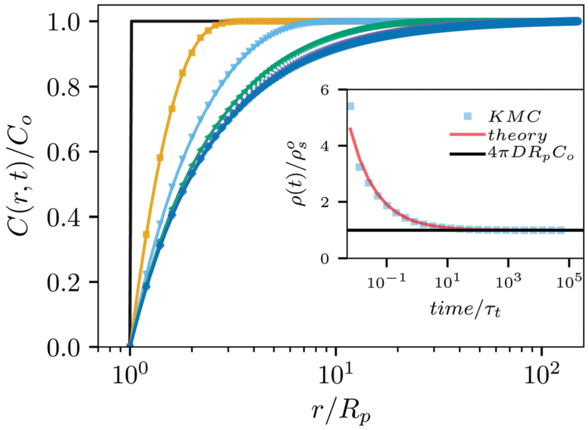

Fig. 2 Scaled concentration $C(r,t)/C_o$ *vs.* r/R_p at different times t (from left to right: t = 0, 0.1, 2, 26, 420 and $6700\tau_t$) for diffusion-limited absorption by a sphere of radius R_p with a source boundary at $R_b = 150R_p$. The data points are from simulations and the solid lines are from the exact solution, eqn (29). Inset: Scaled capture rate $\rho(t)/\rho_s^o$ *vs.* time; the data points (■) are from simulations, the red line is from eqn (30) and the horizontal line is the predicted steady-state.

an infinite system). Fig. 2 shows the radial dependence of $C(r,t)$ at different times t while the inset shows the time-dependent capture rate: the results agree with theory.

4.2 Test 2: diffusion-limited absorption by a sphere in the presence of an outer reflecting boundary

We now replace the SBC at R_b by a reflecting boundary (the total number of particles thus decreases with time), and we compare our results to those of Section 4.1, still in absence of an external field. Here, the concentration is given by (Appendix A)

$$C(r,t) = C_o \sum_{n=1}^{\infty} B_n \frac{\sin\left(k_n\left(r - R_p\right)\right)}{r/R_p} \exp\left(-tDk_n^2\right) \tag{31}$$

where the wavenumbers k_n are the roots of

$$\tan(k_n(R_b - R_p)) = R_b k_n \tag{32}$$

and the weight of the nth decay mode is given by

$$\begin{aligned} B_n &= \frac{\int_0^{R_b-R_p}\left(r + R_p\right)\sin(\lambda_n r)\mathrm{d}r}{R_p\int_0^{R_b-R_p}\sin^2(\lambda_n r)\mathrm{d}r} \\ &= \frac{\sin\left(k_n\left(R_b - R_p\right)\right) - k_n R_b \cos\left(k_n\left(R_b - R_p\right)\right) + k_n R_p}{R_p k_n^2\left(\dfrac{R_b - R_p}{2} - \dfrac{\sin\left(2k_n\left(R_b - R_p\right)\right)}{4k_n}\right)}. \end{aligned} \tag{33}$$

The time dependent capture rate is

$$\rho\left(R_p, t\right) = 4\pi D C_o R_p \sum_{n=1}^{\infty} B_n k_n R_p \exp\left(-tDk_n^2\right). \tag{34}$$

At long times $t \gg R_b^2/D$, the concentration reduces to

$$\frac{C(r,t)}{C_o} \approx B_1 \frac{\sin\left(k_1\left(r - R_p\right)\right)}{r/R_p} \exp\left(-tDk_1^2\right), \tag{35}$$

while the capture rate decays as

$$\rho(R_p, t \to \infty) \approx \rho_s^o \times R_p k_1 B_1 \exp(-tDk_1^2), \tag{36}$$

where k_1 and B_1 are the wavenumber and weight of the longest mode, respectively. The final decay time is thus

$$\tau_1 = 1/Dk_1^2. \tag{37}$$

In the large box limit $R_b \gg R_p$, we obtain $k_1R_b \approx 1.571$, $\tau_1 \approx 0.405\ R_b^2/D$ and $B_1 \approx 0.811R_b/R_p$. Eqn (36) then predicts that $\rho(t)$ becomes smaller than the infinite system plateau rate ρ_s^o when $t > \tau_c \approx 0.2416\tau_1$. In other words, $\tau_1 \sim R_b^2/D$ is the time required to measurably deplete the box as a whole.

We use the simulation setup of Section 4.1 but replace the source boundary by a reflecting one (at $R_b = 60R_p$). Fig. 3 shows the radial dependence of $C(r,t)$ at different times while the inset gives the time-dependent capture rate: the data agree with the theory. The rough estimate above gives a critical time $\tau_c \approx 10^3\tau_t$ here, in agreement with the inset data.

4.3 Field-driven capture rate with a source boundary

In this section, we use a source boundary at $r = R_b = 2\lambda_e$ and an absorbing one at $R_p = r_p/\sqrt{2}$ (the nanopore). Fig. 4 shows the time dependence of the capture rate $\rho(t)$ for different field intensities λ_e, for both the PCF and EAF approximations. The curves collapse remarkably well when the time axis is rescaled by the theoretical PCF transient time $\tau_d(\lambda_e)$. The PCF capture rate rapidly decays to the predicted value at roughly $t \approx \tau_d$. When we use the EAF instead, the curves overlap up to $t \approx \tau_d$, followed by a deep undershoot, and finally the same final rate is

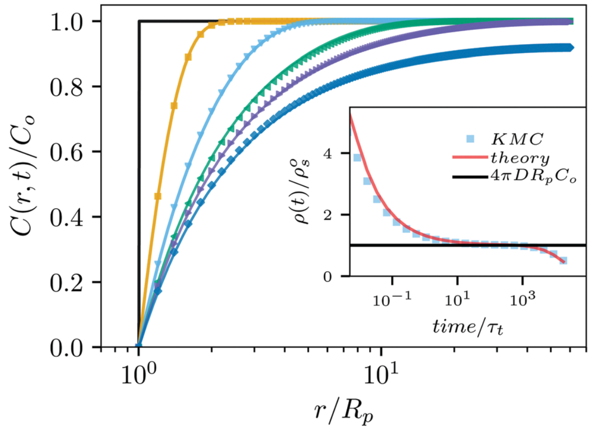

Fig. 3 Scaled concentration $C(r,t)/C_o$ *vs.* r/R_p at different times t (= 0, 0.03, 0.5, 9, 140 and $2300\tau_t$) for diffusion-limited absorption by a sphere of radius R_p with a reflecting boundary at $R_b = 60R_p$. The data points are from simulations while the solid lines show the analytical solution, eqn (31). Inset: Scaled capture rate *vs.* time; the data points (■) are from simulations, the red line is from eqn (34) and the horizontal line is the steady-state value for an infinite system.

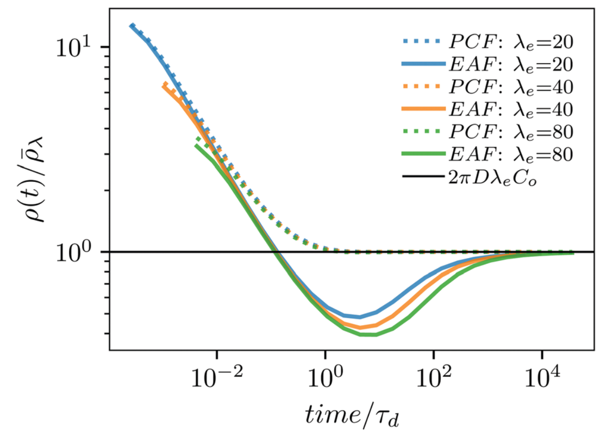

Fig. 4 Capture rate $\rho(t)$ *vs.* time for field intensities λ_e = 20, 40 and 80r_p. The pore (absorbing) boundary is located at $R_p = r_p/\sqrt{2}$ while the source boundary is at R_b = 2λ_e. The horizontal line is the steady state capture rate predicted by eqn (6). The dotted lines are from simulations done using the PCF, eqn (2), while the solid lines give the simulation results when the EAF is used, eqn (28). The time axis is rescaled by the steady-state time $\tau_d(\lambda_e)$ while the capture rates are rescaled by the steady-state theoretical value $\bar{\rho}_\lambda$ = 2$\pi D C_o \lambda_e$.

reached for times $t \gtrsim 10^4\tau_d$. The fact that the EAF field is lower than the PCF field near the pore has two effects: (1) the time required to reach the steady-state is increased; (2) the width r_d of the region where $C(r)$ is not flat is broader (see Fig. 5b for example). Both of these effects contribute to the large increase in the transient time.

Fig. 5 shows several steady-state concentration profiles $C(r,t \gg \tau_d)$ for both PCF and EAF. The $C(r,t \gg \tau_d)$ PCF curves, Fig. 5a, agree perfectly with the analytical solution, eqn (7); in particular, the depletion zones are barely larger than R_p and get narrower at higher field. However, in the EAF case (Fig. 5b), there is a peak near the pore due to the locally flat field, and its position shifts closer to the pore when the field increases. Time-dependent concentration profiles are shown in the insets for λ_e = 80r_p. A depletion zone quickly forms in the PCF case, as expected. However, the EAF concentration increases near pore due to the slower capture rate caused by the flat field; the increasing local concentration results in a higher capture rate; for times $t \gtrsim 10^4\tau_d$, however, these two effects balance each other and the steady-state is reached.

4.4 Field-driven capture rate with a reflecting boundary

We now replace the SBC used in Section 4.3 with an RBC to investigate the impact of finite system size on capture. Fig. 6 shows the concentration profile at three different times for a field intensity λ_e = 20r_p and different box sizes $R_b > \lambda_e$. We observe similar long-time behavior for both the PCF and EAF fields: the concentration near the outer, reflecting wall decreases with time since no new particles arrive from infinity in this case. Unsurprisingly, these effects happen earlier and are more severe for smaller system sizes R_b.

The rate at which the outer depletion zone propagates inward can be estimated as follows. If we assume that the concentration profile is a step function with $C \approx C_o$ up to the beginning of the depletion zone and zero beyond, the equation for the location $r(t)$ of the front is simply

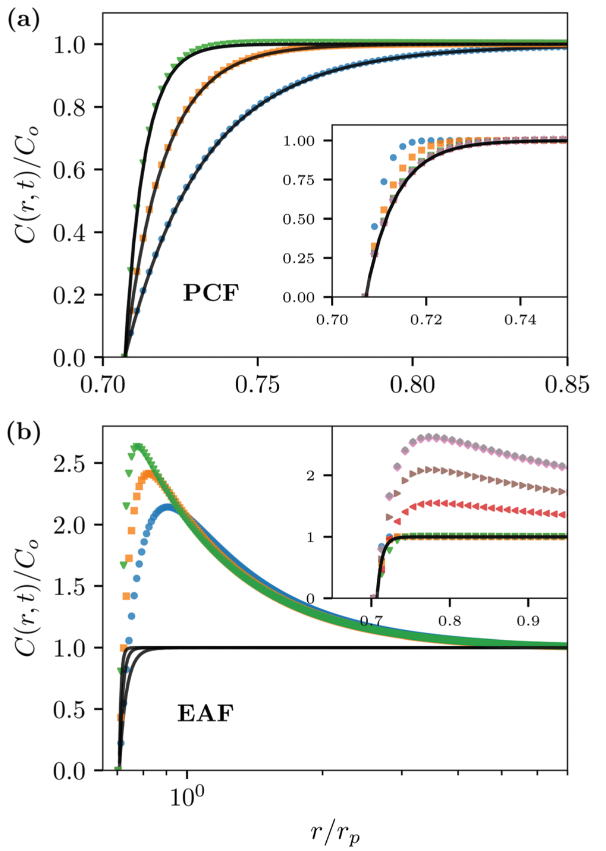

Fig. 5 Scaled concentration $C(r,t)/C_o$ *vs.* r/r_p for field intensities λ_e = 20 (●), 40 (■) and 80 r_p (▼). The pore is located at $R_p = r_p/\sqrt{2}$ while the source boundary is at R_b = 2λ_e. (a) Simulation results at time t = 10τ_d obtained using the PCF. (b) Simulation results at time t = 10 000τ_d obtained using the EAF. In both cases, the solid lines show the PCF prediction, eqn (7). Insets: Simulation data at times 0.07, 0.3, 1, 70, 300, 9000 and 20 000τ_d, with λ_e = 80r_p.

$$2\pi r(t)^2 C_o \mathrm{d}r = -\rho_s^o \mathrm{d}t = -2\pi D C_o \lambda_e \mathrm{d}t, \qquad (38)$$

with $r(0) = R_b$. The solution is

$$r(t) = R_b \times (1 - 3\lambda_e Dt/R_b^3)^{1/3}. \qquad (39)$$

The time taken by this second depletion region to reach the pore is thus $\tau_b \approx R_b^3/3\lambda_e D = \tau_E(R_b,0)$. However, we expect that the capture rate will start being affected roughly when the depletion region reaches the capture radius at $r = \lambda_e$, *i.e.* at time $\tau_\rho \approx [1 - (\lambda_e/R_b)^3]\tau_b$. The inset of Fig. 6a shows the time dependence of the capture rates for the PCF case. The size of the box plays no role at short times, but $\rho(t)$ decreases at longer times – similar to the field-free results in Fig. 3. The rough theory described above overestimates the time at which this happens by a factor of 10, not surprising given the fact that the propagating front is not a step function and thus propagates faster than assumed here.

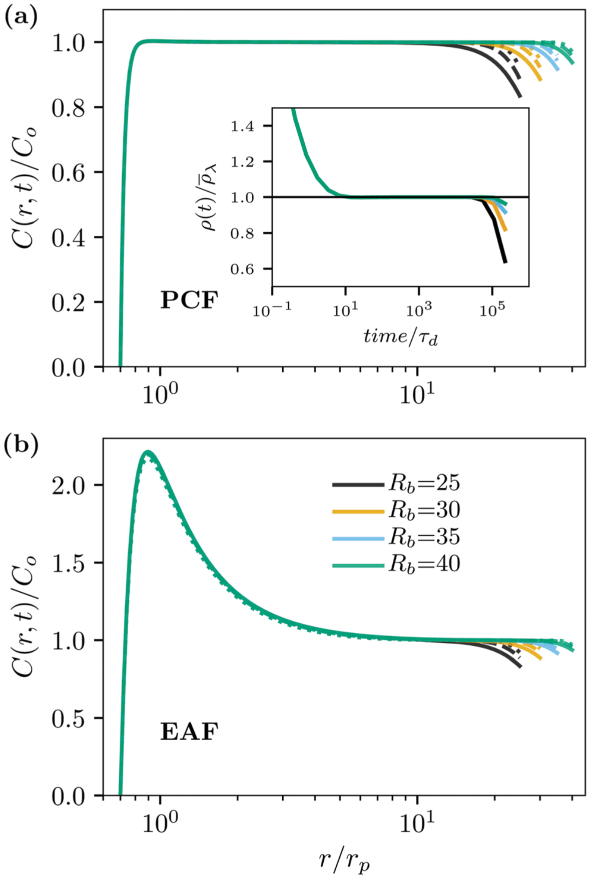

Fig. 6 Scaled concentration $C(r,t)/C_o$ *vs.* r/r_p at times t = 1700 (···), 3500 (- - -) and 7000 (—) τ_d for a field intensity $\lambda_e = 20r_p$. The systems have a reflecting boundary at $r = R_b$, as indicated, and the pore is located at $R_p = r_p/\sqrt{2}$. (a) Simulation results obtained using the PCF, eqn (2). (b) Simulation results obtained using the EAF, eqn (28). Inset in (a): capture rate $\rho(t)$ *vs.* time. The horizontal line is the steady state capture rate predicted by eqn (6).

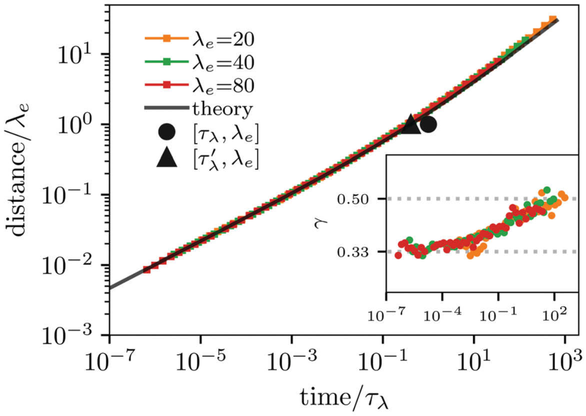

Fig. 7 Log–log plot of the mean distance migrated (in units of λ_e) at time t (in units of τ_λ) when the PCF polarity is reversed. The black line is from eqn (40). The filled circle (●) shows the location of the [τ_λ;λ_e] point, while the triangle (▲) uses the improved estimate of the clean up time τ'_λ given by eqn (40). The particles are initially placed one lattice site above the pore and the data points ($r \geq R_p$) are averaged over 1000 trajectories. Inset: Local slope *vs.* time. The expected values of 1/2 and 1/3 are marked by horizontal lines.

4.5 Time reversal and particle escape

To better understand the dynamics of the particles at different radial distances r, we now study the inverse of the capture process by using an open boundary condition and an inverted PCF polarity. Our goal is to examine the transition between field-driven and diffusion-driven dynamics when a particle moves across the capture radius (the same transition occurs for escape and capture simulations, but the former are computationally more efficient).

We start the particles one lattice site above the pore and let them move away; however, we only record the data once the particles have reached the location $r = R_p$ of the absorbing boundary used in the previous section. The time dependence of the mean radial displacement $\bar{r}(t)$ can inform us about the relative importance of diffusion and electric drift during capture. Indeed, we expect that a particle moving away from the pore will go through two main phases: field-driven (as described by eqn (4)) for short distances, and then diffusive when $r > \lambda_e$ (and similarly, but in reverse order, for capture).

Fig. 7 shows $\bar{r}(t)$ *vs.* t for several field intensities λ_e, and the inset shows the local slope (*i.e.*, the exponent γ if $\bar{r}(t) \sim t^\gamma$). We clearly have two regimes, with $\gamma = 1/2$ (diffusion) at long times $t > \tau_\lambda$, preceded by $\gamma = 1/3$ (field-driven motion).

The data for different field intensities collapse if the distances and times are rescaled by the capture radius λ_e and the cleanup time τ_λ, respectively, in agreement with our previous paper.[25] However, the curves do not quite go through the [τ_λ,λ_e] point as one might have expected. The reason for this is the fact that eqn (5) considers only the deterministic effect of the field and neglects both diffusion and entropic effects. If we take volume (entropic) effects into account, the deterministic time $\tau_r(r)$ to reach a distance r from the origin can be calculated by integrating the combined effects of the electric force ∇U_e and the entropic force $-\nabla U_v$:

$$\begin{aligned}\tau_r(r) &= \frac{k_B T}{D}\int_0^r \frac{dr'}{-\nabla U_v(r') + \nabla U_e(r')} \\ &= \frac{\lambda_e^2 \ln(2r/\lambda_e + 1) - 2r(\lambda_e - r)}{8D}.\end{aligned} \qquad (40)$$

A more accurate estimate of the time to reach the radial distance $r = \lambda_e$ is thus $\tau'_\lambda = \tau_r(\lambda_e) = \frac{3\ln(3)}{8}\tau_\lambda$. Fig. 7 shows that τ'_λ agrees nicely with the simulation results. In the limit $r \gg \lambda_e$ where diffusion dominates eqn (40) gives $\tau_r \approx r^2/4D$ instead of the expected $\tau_r \approx r^2/6D$ in three dimensions: this is the reason why the black curve in Fig. 7 is then below the simulation data. The EAF data are similar although not identical at short times due to the flat field (not shown).

5 Can we concentrate analytes using a time-varying field?

Our KMC algorithm allows us to also study molecular mixtures as well as time-dependent fields. As an example, we now investigate (as a proof of concept) a process by which it might be possible to favour the capture of one molecular species in a mixture of two types of molecules.

The steady-state capture rate is given by eqn (6). Returning to the original variables, this can be written as $\rho = 2\pi C_o \Delta V r_e \mu$, showing that while the mobility μ affects the capture rate, the diffusion coefficient D does not. Therefore, the most challenging situation would be to manipulate the capture rates of two molecules that happen to share the same mobility μ. We will be using this hypothetical case for our proof-of-concept analysis.

We thus consider a mixture with two types of analytes having the same mobility $\mu_1 = \mu_2$ but different diffusion coefficients, with $D_1 < D_2$. The question we are asking ourselves here is simply: can we design a capture process that would favor one species?

In order to bias the translocation process, we have to exploit the fact that $D_1 \neq D_2$, and this implies that we periodically turn the field off so that diffusion can play a role. One approach is to briefly reverse the field polarity to create a depletion region near the pore, and then turn the field off to let the molecules fill this region by diffusion – a slow process that will bring more of the fast-diffusing, smaller type 1 molecule in the vicinity of the pore. If we then apply the translocating field for a short period of time, the nanopore will capture more type 1 than type 2 molecules. Repeating this pulse sequence (Fig. 1d) will lead to a capture process that is biased in favour of type 1 molecules.

The duration of the three pulses in the sequence will be denoted t_ϕ, $t_\leftarrow$ and $t_\rightarrow$. These pulse durations must be selected properly, as we now demonstrate.

According to eqn (4), the radius of the depletion region created during the reverse field phase is

$$\Delta r_\leftarrow \approx \sqrt[3]{3\mu\Delta V r_e t_\leftarrow}. \tag{41}$$

During the recovery phase of duration t_ϕ, the field is turned off and the molecules refill the depletion zone by diffusion. The change in radius of this region is thus

$$\Delta r_\varnothing^{(1,2)} \approx \sqrt{6D_{1,2}t_\varnothing}. \tag{42}$$

Since $D_2 < D_1$, choosing t_ϕ such that $\Delta r_\phi^{(2)} < \Delta r_\leftarrow$ would minimize the number of type 2 molecules near the pore, while a t_ϕ that gives $\Delta r_\phi^{(1)} \geq \Delta r_\leftarrow$ would maximize capture of type 1 molecules. In other words, we need

$$\Delta r_\phi^{(1)} \geq \Delta r_\leftarrow > \Delta r_\phi^{(2)}. \tag{43}$$

In the final phase, we want to capture the molecules in the region not yet fully refilled by the slowest type 2 molecules. Since this region has a radius $\Delta r^{(2)} \approx \Delta r_\leftarrow - \Delta r_\phi^{(2)}$, this means

$$t_\rightarrow < \tau_E(\Delta r^{(2)},0) \tag{44}$$

where τ_E can be estimated using eqn (4). One last condition must be satisfied since the type 1 molecules that reach the mouth of the nanopore must also have time to translocate across the entire nanochannel during the capture pulse of duration $t_\rightarrow$ (we assume that those who do are taken away immediately and permanently, *e.g.* by a liquid flow parallel to the wall). The electric field near nanopore ($r \leq r_p$) is flat with a field intensity of $E_o = E_{PCF}(r_p) = -\Delta V r_e / {r_p}^2$, which is essentially the same as the electric field inside the nanochannel. The distance travelled by the particles (both types) located inside the nanochannel (nc) during the forward field period is thus

$$r_{nc} = \mu E_o t_\rightarrow = \frac{\lambda_e D}{{r_p}^2} t_\rightarrow \tag{45}$$

The last condition is simply

$$r_{nc} > \ell_{nc}, \tag{46}$$

where $\ell_{nc} = \ell_p + 2R_p$ is basically the effective length of the channel here. The three pulse durations must be chosen to satisfy eqn (43), (45) and (46) simultaneously. As usual, the performance of such a system will be a trade-off between high selectivity and high capture rates. We give an example below.

Our KMC simulation scheme can easily be adapted to also include analyte field-driven drift across the nanochannel. The translocation process itself is simply 1D motion in the presence of a uniform field (of intensity E_0). The cross-sectional area of the channel is exactly the surface area of the absorber at $r = R_p$, and the field at that point is indeed $\approx E_0$. We thus extend the x-axis from $r = +R_p$ (where the absorber was located in the previous sections) to $r = -\ell_p - R_p$ (see Fig. 8) and we don't use any entropic force when $r < R_p$. During the forward pulse of duration $t_\rightarrow$, we place the absorber at $r = -\ell_p - R_p$ on the *trans*-side (this is replaced by a RBC during the other two phases in order to stop any leakage). During the recovery phase of duration t_ϕ, a RBC is placed at $r = R_p$ so that analytes do not diffuse inside the nanochannel. These conditions strongly limit the contribution of non-field driven translocation of analytes. Finally, a source boundary is applied maintained at $R_b = 60r_p$ throughout, and the system starts with a uniform concentration C_o.

Since $\lambda_e \sim Q$ and $\mu \sim DQ$, we must have $\lambda_e \sim 1/D$ in order to keep the mobility molecular size independent. In our simulations, we use $D_1 = 2D_2 = 2D$ and a field intensity $\lambda_e^{(2)} = 50r_p = 2\lambda_e^{(1)} \equiv \lambda_e$. In order to define the pulse durations in an unambiguous way, we need a time scale that does not depend on molecular size such as the cleanup time τ_p needed to empty a zone of radius R_p,

$$\tau_p = \tau_E(R_p,0) = {R_p}^3/3\lambda_e D, \tag{47}$$

which is size-independent here since $\lambda_e D \sim \mu$.

The choice of pulse parameters is guided by the three constraints presented above. We first test the following parameters: backward pulse $t_\leftarrow = 62.5\tau_p \ll \tau_\lambda$; refill time $t_\phi \approx {r_\leftarrow}^2/6D_1 \approx 196.9\tau_p$; and capture time $t_\rightarrow = 29.0\tau_p$. Fig. 8 shows the steady-state concentration pattern for the two particles at the end of the reverse (solid lines) and refill (dotted lines) phases. Clearly, the depletion zone at the end of the $t_\leftarrow$ pulse is larger

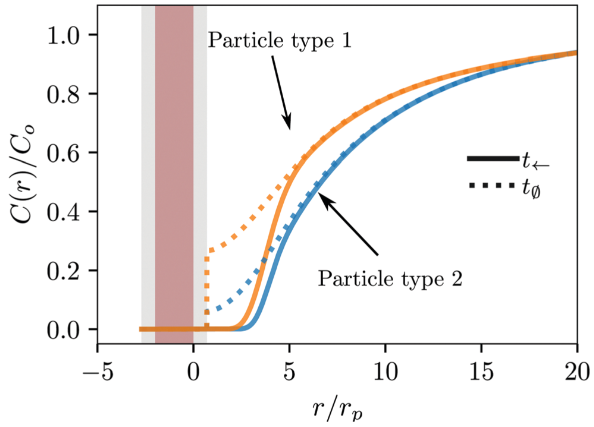

Fig. 8 Scaled concentration $C(r,t)/C_o$ *vs.* scaled radial distance r/r_p for two particles with same mobility but two different diffusion coefficients (see text) under a time-varying field, after 100 cycles. Solid lines: at the end of the reverse phase of duration $t_{\leftarrow} = 62.5\tau_p$. Dotted lines: at the end of the refill phase of duration $t_\phi = 196.9\tau_p$. The brown area marks the position of the wall/membrane with a thickness of ℓ_p, and the gray bands are of thickness R_p.

for particle (2): this is expected since the pulses are designed to keep them far from the nanopore. The molecules then diffuse toward the pore during the t_ϕ phase: obviously, the gap between the dotted lines near the pore must result in two different capture rates. In this particular case, the ratio $\bar{\rho}_1/\bar{\rho}_2$ between the mean capture rates of the two molecular species is ≈ 2.5.

The two capture rates and their ratio can both be modified by changing the refill time, as shown in Fig. 9. The ratio of the mean capture rates increases by a factor of ≈ 6 here; however, the mean capture rates also decrease (≈ 3 fold). An ideal device would have both a high capture ratio and a large capture rate, but in practice, this is not achievable: as usual in separation science, one has to choose between purity and speed. Optimizing the value of the other two time parameters for a given pair of same-mobility analytes is beyond the scope of this paper.

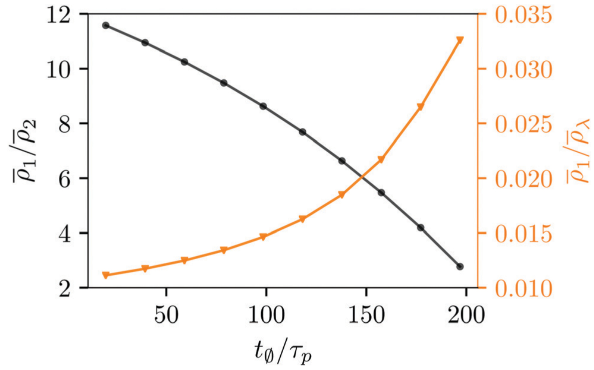

Fig. 9 The ratio $\bar{\rho}_1/\bar{\rho}_2$ of the mean capture rates of the two molecular species (●), and the scaled mean capture rate $\bar{\rho}_1/\bar{\rho}_\lambda$ of the favored species (▼), *vs.* the (scaled) recovery time t_ϕ/τ_p for the system described in Fig. 8.

6 Discussion and conclusion

We have proposed a KMC algorithm that can efficiently map a spherically symmetric d-dimensional drift-diffusion problem onto a 1D biased random walk, and we successfully tested it using the standard problem of the diffusion-limited absorption of point-like particles by a sphere in both finite and infinite systems. The 1D projection greatly reduces the amount of memory needed to simulate large $d > 1$ systems.

Our new KMC algorithm allows us to investigate both the short-time and steady-state dynamics of capture when a point-like external field is added. Our simulation results are in excellent agreement with the theoretical steady-state infinite-system concentration profiles and capture rates in 3D, further supporting the validity of the algorithm. Moreover, the short-time data agree with our theoretical estimates of the steady-state time $\tau_d \sim 1/D\lambda_e^2$ and of the size r_d of the depletion region. We note that the depletion region is barely larger than the pore size, and that τ_d is too short to be observed in the lab.

Interestingly, when the short-distance field is modified to take into account the finite width of the pore, the flatness of the (EAF) field near the pore creates a local traffic jam resulting in a substantially lower initial capture rate and a much increased steady-state time τ_d. Furthermore, the plateau concentration is moved to larger distances r_d. Nevertheless, the same steady-state capture rate is eventually reached, and both τ_d and r_d remain too small to be observable in typical experiments. Crucially, these results strongly suggest that one should not expect any useful depletion region or concentration patterns near the nanopore.

When the system is a finite-size cavity, short time capture dynamics is similar to that observed in an infinite system, as one would expect. The region of the cavity that is beyond the capture radius λ_e acts as a reservoir. As this reservoir is being slowly depleted, an outer depletion zone propagates inward from the cavity walls. The capture rate starts to decay from its initial steady state value when the front of the outer depletion region reaches the capture region at $r = \lambda_e$; however, since the time needed to reach this point increases rapidly with the cavity size ($\sim R_b^3$ if $R_b \gg \lambda_e$, which is normally the case), the capture rate can only be affected in small systems.

Of course, our KMC algorithm can also be used to simulate single particles dynamics. We thus revisited the reverse-polarity single-particle escape process that we introduced in our previous paper.[25] We again observe that the dynamics change from field-driven to diffusion-controlled at a distance λ_e, as expected from theory. Exploiting the fact that our 3D to 1D projection adds an entropic force to the equation of motion, we have proposed an improved approximation for the time-dependent mean trajectory $r(t)$ of the particles, in excellent agreement with the simulation data.

In the last part of the paper, we proposed a novel pulsed-field nanopore-based scheme to separate two different types of molecules with the same mobility but different diffusion coefficients. Section 5 is intended to be a simple proof of concept showing that exploiting diffusivity differences might be possible. Clearly, one can change both the parameters, and even the shape, of the field pulses proposed here. For example, decreasing the recovery time can increase the ratio between the two capture rates, but at the cost of also decreasing the magnitude of both capture rates. In principle, one can also use an array of nanopores to enhance quantities, or a sequence of nanopores to enhance purity.

Conflicts of interest

There are no conflicts to declare.

Appendix

A The solution for a RBC and pure diffusion

With an ABC at $r = R_p$ and a RBC at $r = R_b$, the solution must satisfy the conditions $C(R_p,t) = 0$ and $\partial_r C(r,t)|_{R_b} = 0$. We first define $u(r,t) = rC(r,t)$ and substitute this into eqn (1) to obtain the simple differential equation

$$\frac{\partial u(r,t)}{\partial t} = D\frac{\partial^2 u(r,t)}{\partial r^2} \tag{48}$$

Using the separation of variables method with $u(r,t) = \phi(r)g(t)$, one obtains

$$g(t) = \exp(-tDk^2) \tag{49}$$

and

$$\phi(r) = A\cos(k(r-R_p)) + B\sin(k(r-R_p)), \tag{50}$$

where A and B are constants and $k > 0$. The ABC at $r = R_p$ imposes that $A = 0$ and the RBC at $r = R_b$ leads to eqn (33) for k. Note that eqn (33) has an infinite number of roots k_n and must be solved numerically. When $n \gg 1$, however, we find $k_n \to n\pi/(R_b - r_p)$. Since the eigenfunctions ϕ_n are orthogonal, using the initial condition $u(r,t = 0) = rC_o$, one can find the weights given eqn (33).

Acknowledgements

GWS acknowledges the support of both the University of Ottawa and the Natural Sciences and Engineering Research Council of Canada (NSERC), funding reference number RGPIN/046434-2013. LQ is supported by the Chinese Scholarship Council and the University of Ottawa.

References

1 E. Beamish, V. Tabard-Cossa and M. Godin, *ACS Sens.*, 2019, **4**, 2458–2464.
2 A. N. Sohi, E. Beamish, V. Tabard-Cossa and M. Godin, *Anal. Chem.*, 2020, **92**, 8108–8116.
3 M. Charron, K. Briggs, S. King, M. Waugh and V. Tabard-Cossa, *Anal. Chem.*, 2019, **91**, 12228–12237.
4 J. T. Hagan, B. S. Sheetz, Y. N. D. Bandara, B. I. Karawdeniya, M. A. Morris, R. B. Chevalier and J. R. Dwyer, *Anal. Bioanal. Chem.*, 2020, **412**, 6639–6654.
5 P. Bandarkar, H. Yang, R. Henley, M. Wanunu and P. C. Whitford, *Biophys. J.*, 2020, **118**, 1612–1620.
6 L. He, P. Karau and V. Tabard-Cossa, *Nanoscale*, 2019, **11**, 16342–16350.
7 W. Shi, A. K. Friedman and L. A. Baker, *Anal. Chem.*, 2017, **89**, 157–188.
8 M. Waugh, K. Briggs, D. Gunn, M. Gibeault, S. King, Q. Ingram, A. M. Jimenez, S. Berryman, D. Lomovtsev, L. Andrzejewski and V. Tabard-Cossa, *Nat. Protoc.*, 2020, **15**, 122–143.
9 D. Garoli, H. Yamazaki, N. Maccaferri and M. Wanunu, *Nano Lett.*, 2019, **19**, 7553–7562.
10 M. J. Kim, M. Wanunu, D. C. Bell and A. Meller, *Adv. Mater.*, 2006, **18**, 3149–3153.
11 T. Gilboa, E. Zvuloni, A. Zrehen, A. H. Squires and A. Meller, *Adv. Funct. Mater.*, 2020, **30**, 1900642.
12 Y. M. N. D. Y. Bandara, J. Saharia, B. I. Karawdeniya, J. T. Hagan, J. R. Dwyer and M. J. Kim, *Nanotechnology*, 2020, **31**, 335707.
13 T. Sakaue, *Phys. Rev. E*, 2007, **76**, 021803.
14 M. Muthukumar, *Polymer Translocation*, Taylor & Francis, Boca Raton, 2011.
15 M. Wanunu, *Phys. Life Rev.*, 2012, **9**, 125–158.
16 D. Panja, G. T. Barkema and A. B. Kolomeisky, *J. Phys.: Condens. Matter*, 2013, **25**, 413101.
17 V. V. Palyulin, T. Ala-Nissila and R. Metzler, *Soft Matter*, 2014, **10**, 9016–9037.
18 S. Buyukdagli, J. Sarabadani and T. Ala-Nissila, *Polymers*, 2019, **11**, 118.
19 K. Briggs, G. Madejski, M. Magill, K. Kastritis, H. W. de Haan, J. L. McGrath and V. Tabard-Cossa, *Nano Lett.*, 2018, **18**, 660–668.
20 M. H. Lam, K. Briggs, K. Kastritis, M. Magill, G. R. Madejski, J. L. McGrath, H. W. de Haan and V. Tabard-Cossa, *ACS Appl. Nano Mater.*, 2019, **2**, 4773–4781.
21 O. M. Eggenberger, G. Leriche, T. Koyanagi, C. Ying, J. Houghtaling, T. B. H. Schroeder, J. Yang, J. Li, A. Hall and M. Mayer, *Nanotechnology*, 2019, **30**, 325504.
22 A. Bhattacharya and S. Seth, *Phys. Rev. E*, 2020, **101**, 052407.
23 P. Chen, J. Gu, E. Brandin, Y.-R. Kim, Q. Wang and D. Branton, *Nano Lett.*, 2004, **4**, 2293–2298.
24 A. Y. Grosberg and Y. Rabin, *J. Chem. Phys.*, 2010, **133**, 165102.
25 L. Qiao, M. Ignacio and G. W. Slater, *J. Chem. Phys.*, 2019, **151**, 244902.
26 P. Rowghanian and A. Y. Grosberg, *Phys. Rev. E*, 2013, **87**, 042723.
27 P. Rowghanian and A. Y. Grosberg, *Phys. Rev. E*, 2013, **87**, 042722.
28 S. K. Nomidis, G. Maglia and E. Carlon, *J. Phys.: Condens. Matter*, 2018, **30**, 304001.
29 J. Nakane, M. Akeson and A. Marziali, *Electrophoresis*, 2002, **23**, 2592–2601.

30 M. Muthukumar, *J. Chem. Phys.*, 2010, **132**, 195101.

31 F. Farahpour, A. Maleknejad, F. Varnik and M. R. Ejtehadi, *Soft Matter*, 2013, **9**, 2750.

32 S. C. Vollmer and H. W. de Haan, *J. Chem. Phys.*, 2016, **145**, 154902.

33 L. Qiao and G. W. Slater, *J. Chem. Phys.*, 2020, **152**, 144902.

34 H. H. Katkar and M. Muthukumar, *J. Chem. Phys.*, 2018, **148**, 024903.

35 S. Buyukdagli and T. Ala-Nissila, *J. Chem. Phys.*, 2017, **147**, 114904.

36 M. Muthukumar, *J. Chem. Phys.*, 2014, **141**, 081104.

37 M. Wanunu, W. Morrison, Y. Rabin, A. Y. Grosberg and A. Meller, *Nat. Nanotechnol.*, 2010, **5**, 160–165.

38 A. E. Nkodo, J. M. Garnier, B. Tinland, H. Ren, C. Desruisseaux, L. C. McCormick, G. Drouin and G. W. Slater, *Electrophoresis*, 2001, **22**, 2424–2432.

39 S. Allison, M. Potter and J. McCammon, *Biophys. J.*, 1997, **73**, 133–140.

40 N. G. van Kampen, *Stochastic Processes in Physics and Chemistry*, Elsevier, Amsterdam, Boston, 3rd edn, 2007.

41 S. Redner, *A Guide to First-Passage Processes*, Cambridge Univ. Press, Cambridge, 2001.

42 M. V. Chubynsky and G. W. Slater, *Phys. Rev. E*, 2012, **85**, 016709.

43 M. G. Gauthier and G. W. Slater, *Phys. Rev. E*, 2004, **70**, 015103.

44 H. W. de Haan, M. G. Gauthier, M. V. Chubynsky and G. W. Slater, *Comput. Phys. Commun.*, 2011, **182**, 29–32.

45 S. W. Kowalczyk, A. Y. Grosberg, Y. Rabin and C. Dekker, *Nanotechnology*, 2011, **22**, 315101.

46 P. C. Bressloff, *Stochastic Processes in Cell Biology*, Springer International Publishing, Cham, 2014, vol. 41.

6

Capture of rod-like molecules by a nanopore : defining an "orientational capture radius"

Reproduced from :
Qiao, Le, and Gary W. Slater, J. Chem. Phys. 152, 144902 (2020) ;
https ://doi.org/10.1063/5.0002044,
with the permission of AIP Publishing

The Journal of Chemical Physics ARTICLE scitation.org/journal/jcp

Capture of rod-like molecules by a nanopore: Defining an "orientational capture radius"

Cite as: J. Chem. Phys. 152, 144902 (2020); doi: 10.1063/5.0002044
Submitted: 21 January 2020 • Accepted: 19 March 2020 •
Published Online: 9 April 2020

Le Qiao[a] and Gary W. Slater[b]

AFFILIATIONS

Department of Physics, University of Ottawa, Ottawa, Ontario K1N 6N5, Canada

[a] Electronic mail: lqiao@uottawa.ca
[b] Author to whom correspondence should be addressed: gslater@uottawa.ca

ABSTRACT

Both the translational diffusion coefficient D and the electrophoretic mobility μ of a short rod-like molecule (such as dsDNA) that is being pulled toward a nanopore by an electric field should depend on its orientation. Since a charged rod-like molecule tends to orient in the presence of an inhomogeneous electric field, D and μ will change as the molecule approaches the nanopore, and this will impact the capture process. We present a simplified study of this problem using theoretical arguments and Langevin dynamics simulations. In particular, we introduce a new *orientational capture radius*, which we compare to the capture radius for the equivalent point-like particle, and we discuss the different physical regimes of orientation during capture and the impact of initial orientations on the capture time.

I. INTRODUCTION

Field-driven translocation through a nanopore can be used to analyze biomolecules such as microRNA, DNA, and proteins,[1–8] and new methodologies are continuously being proposed to enhance the performance of the related devices, e.g., improving the capture by pre-confining the DNA with a nanoporous filter,[9,10] controlling the translocation time by coating the nanopore with a lipid bilayer,[11,12] and achieving multiplexed detection using DNA-based labels or carriers.[1,6,13] Unlike spherical objects, highly charged dsDNA molecules can either deform and stretch (if their contour length L is much larger than their persistence length L_p) or simply orient (if $L < L_p$) during the capture process;[14–17] for dsDNA, $L_p \sim 50$ nm or ~150 *bp* under typical salt conditions.[18] The impact of the coupling between the dsDNA conformation/orientation and its dynamics is often neglected. Another example is the translocation of a rod-shaped virus:[19,20] the tobacco mosaic virus (TMV)[21–23] is a charged rigid rod of ~300 nm length and ~15 nm diameter with a persistence length >10 times its length.

Previous studies of the translocation of charged rod-like objects mainly focused on how rods enter a nanopore and then translocate.[17,19,24,25] In this short paper, we examine the capture of a short rod-like object by the field gradient extending outside a nanopore and, in particular, the impact of rod orientation on the capture process. Describing the orientation of the rod using a local order parameter, we conclude that the physics of the problem is related to a new length scale R_θ that characterizes the radial position where orientation starts. Since R_θ is smaller than the standard capture radius, rods drift faster than they can orient, with potential impact on capture rates.

II. THEORETICAL ANALYSIS

As discussed in Sec. II A, the field lines are radial and the field intensity decays as $E \sim 1/r^2$ at large distances from a nanopore (see Fig. 1). A rod-like molecule thus feels a torque and orients in the resulting field gradient to minimize its local energy. We will characterize the mean orientation using the order parameter

$$\Theta = \tfrac{1}{2}\left[3\langle\cos^2\theta\rangle - 1\right], \tag{1}$$

where θ is the angle between the molecule's principal axis and the local field direction. Note that $\Theta = 1$ for perfect alignment, while $\Theta = 0$ for random orientation ($r \to \infty$).

A. The electric field and forces

For radial distances r much larger than the pore radius r_p, the electric field outside the pore can be represented by the point-charge

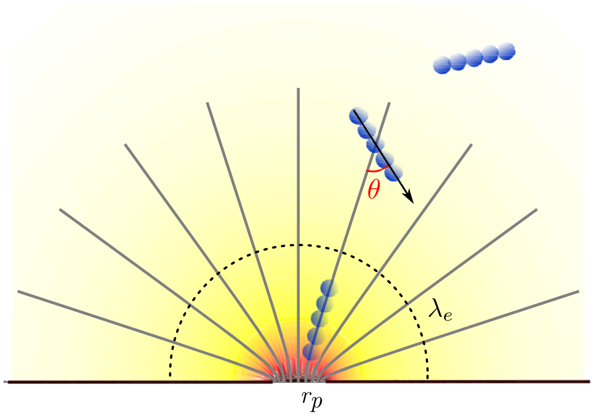

FIG. 1. A schematic view of the nanopore system. The background colors code for the electric field strength (red indicates higher fields). The dashed line depicts the capture radius λ_e, while the gray lines depict field lines. The angle between the rod and the electric field line is θ.

approximation[26,27]

$$E(r) \approx -r_e \Delta V/r^2, \tag{2}$$

where ΔV is the potential difference across the system and the length scale $r_e = r_p/(\frac{2l}{r_p} + \pi)$ describes the pore's size and aspect ratio (l is the pore length). This approximation will be used in our theoretical analysis, while an analytical solution to Laplace's equation[14,28] will be used in the simulations.

As described in Ref. 29, $Q = k_B T\mu/D$ is the effective DNA electrophoretic charge, where μ and D are the mobility and diffusion coefficient of the DNA in free solution. The standard definition of the capture radius is the length scale $r = \lambda_e$, where the analyte's potential energy $QV(r) = k_B T$; this gives

$$\lambda_e = \frac{Q\Delta V}{k_B T} r_e. \tag{3}$$

Note that we will use λ_e to measure the amplitude of the applied electric forces; for instance, the velocity of the rod can then be written simply as $v(r) = \lambda_e D/r^2$.

For the simulations, we chose the following dimensionless parameters: a rod of length $L = \frac{10}{3} r_p$, a pore aspect ratio of $l/r_p = 2$ (giving $r_e = \frac{r_p}{4+\pi}$), and fields in the range of $\lambda_e = 200$–$1000\ r_p$. As a guide, if one were to map this simulation onto the dynamics of a short $L = 100\ bp$ (or ≈34 nm long) dsDNA, the pore size would be $r_p \approx 10$ nm, the effective rod charge would be $Q = k_B T\mu/D \approx 70\ e$, and the voltages would be in the range $\Delta V \approx 0.5$–$2.5\ V$.

B. Static orientation in the field gradient

We consider a uniformly charged rigid rod of length L whose center of mass (CM) is at position r, and we assume that it is in orientational equilibrium in the potential $V(r)$. Its potential energy in this radial field is

$$\frac{\Psi_\theta(r)}{k_B T} = \frac{\lambda_e}{L} \cdot \int_{-L/2}^{+L/2} \frac{\mathrm{d}z}{\sqrt{r^2 + z^2 + 2rz\cos\theta}}, \tag{4}$$

where z is the distance between a charge along the rod and the center-of-mass of the rod. Note that the potential energy of the rod depends only on the distance r and the angle θ because the field in Eq. (2) is radial. The orientational potential energy for the rod is

$$\delta\Psi_\theta(r) = \Psi_{\theta=0}(r) - \Psi_\theta(r), \tag{5}$$

and the corresponding mean orientation is given by[30,31]

$$\langle\cos^2\theta(r)\rangle = \frac{\int_0^\pi \cos^2\theta \sin\theta \exp\left(-\delta\Psi_\theta(r)/k_B T\right)\mathrm{d}\theta}{\int_0^\pi \sin\theta \exp\left(-\delta\Psi_\theta(r)/k_B T\right)\mathrm{d}\theta}. \tag{6}$$

Although these integrals cannot be done in the closed form, they can be computed numerically to obtain the order parameter $\Theta(r)$ for different values of the nominal capture radius λ_e (see Fig. 2). As expected, $\Theta(r)$ drops quickly with distance because the field gradient decays as r^{-3}. We note that distances much smaller than λ_e are needed to obtain substantial orientation: in other words, the DNA rod is "captured" much before it orients.

When $r \gg L$, the asymptotic form of Eq. (6) is

$$\Theta(r) \approx \lambda_e L^2/60\ r^3 \equiv (R_\theta/r)^3, \tag{7}$$

where the length scale R_θ will be called the *orientational capture radius*. Since $\lambda_e \sim Q \sim \mu/D$, it scales like

$$R_\theta = \left(\tfrac{1}{60}\lambda_e L^2\right)^{1/3} \sim \left(L^2 \Delta V/D\right)^{1/3}. \tag{8}$$

The inset of Fig. 2 shows the same data but with r now rescaled using R_θ. The curves collapse, except (weakly) at very short distances. The

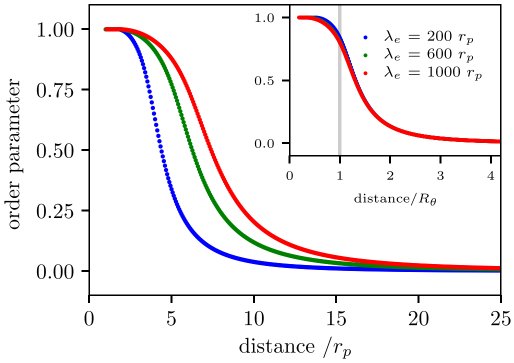

FIG. 2. Static order parameter $\Theta(r)$ vs scaled distance r/r_p for a rod of length $L = \frac{10}{3} r_p$ and different field intensities λ_e (in units of r_p), as obtained from the numerical integration of Eq. (6). Inset: same data with the x-axis now rescaled using R_θ, with R_θ (λ_e = 200 r_p) = 3.3 r_p, R_θ (600 r_p) = 4.8 r_p, and R_θ (1000 r_p) = 5.7 r_p.

orientational capture radius $R_\theta = \sqrt[3]{\lambda_e L^2/60}$ is thus the length scale describing the decay of the order parameter. Importantly, we have $R_\theta \ll \lambda_e$ since $L \ll \lambda_e$. Given that $D \sim 1/L$ for a rod, this relation also predicts that $R_\theta \propto L\Delta V^{1/3}$, where the 1/3-scaling comes directly from the field gradient. Note that we chose three dimensionless field intensities $\lambda_e > 60L$ to ensure that $R_\theta \geq L$.

C. Scaling analysis

We now examine this problem using a scaling analysis of the competition between the field-driven and the diffusion-driven rotation for a rod fixed in space at CM position r. The rod's free rotational relaxation time is roughly the time it needs to diffuse over half its own length[32] and thus scales like $\tau_\theta \sim L^2/D$. When $r \gg L$, the force driving rotation is $F_e \sim \mathrm{d}\psi_\theta/L\mathrm{d}\theta \sim L\lambda_e kT/r^3$, and the corresponding time scale is $\tau_e \sim L/(F_e/\xi)$, where $\xi = k_BT/D$ is the friction coefficient. When $\tau_\theta < \tau_e$, rotational diffusion dominates and the electric forces are not sufficient to align the rod along the local field line; when $\tau_\theta > \tau_e$, on the other hand, rotational diffusion cannot stop the rod from orienting. The location r where $\tau_\theta = \tau_e(r)$ scales like $r \sim (\lambda_e L^2)^{1/3} \sim R_\theta$, in agreement with the analysis of the equilibrium limit presented in Sec. II B.

III. SIMULATIONS: METHODS AND RESULTS

A. Coarse-grained stiff rod-like molecules

We employ Langevin Dynamics (LD) simulations and more precisely the ESPResSo's standard coarse-grained bead-spring model.[33,34] The excluded volume interactions between monomer beads and between the wall and the monomers are modeled using a repulsive Weeks–chandler–Andersen potential (WCA),[35]

$$U_{\mathrm{WCA}}(r) = \begin{cases} 4\epsilon\left[\left(\frac{\sigma}{r}\right)^{12} - \left(\frac{\sigma}{r}\right)^{6}\right] + \epsilon & \text{for } r < r_c \\ 0 & \text{for } r \geq r_c. \end{cases} \tag{9}$$

The parameter $\epsilon = k_BT$ is used as the fundamental unit of energy in our simulations, the nominal monomer size σ is used as the fundamental unit of length, and $r_c = 2^{1/6}\,\sigma$ is the cutoff length that makes U_{WCA} purely repulsive. Adjacent monomers are connected with the Finitely -Extensible-Nonlinear-Elastic (FENE) potential,[36]

$$U_{\mathrm{FENE}}(r) = -\tfrac{1}{2}K_{\mathrm{FENE}}\, r_0^2\, \ln\left(1 - \frac{r^2}{r_0^2}\right). \tag{10}$$

We use the spring constant $K_{\mathrm{FENE}} = 30\ \epsilon/\sigma^2$ and the maximum extension $r_0 = 1.5\ \sigma$. We control the chain stiffness via the harmonic angular potential,

$$U_{\mathrm{Bend}}(\phi) = \tfrac{1}{2}K_{\mathrm{Bend}}(\phi - \pi)^2, \tag{11}$$

with the bending constant $K_{\mathrm{Bend}} = 100\ \epsilon$; the molecule's persistence length is approximately equal to the nominal thermal bending length in free solution:[37] $L_p/\sigma \approx K_{\mathrm{Bend}}/k_BT = 100$, where $\sigma = \frac{2}{3}\,r_p$ is the nominal monomer size. Our five bead molecule has a contour length of $L = 5\,\sigma = \frac{10}{3}\,r_p \ll L_p$.

B. Langevin dynamics simulations

Since the solvent is implicit in LD formalism, the equation of motion for a monomer of mass m is[33]

$$m\dot{\vec{v}} = \vec{\nabla}U(\vec{r}) - \xi\vec{v} + \sqrt{2\xi k_{\mathrm{B}}T}\,\vec{R}(t), \tag{12}$$

where $U(\vec{r}) = U_{\mathrm{WCA}}(\vec{r}) + U_{\mathrm{FENE}}(\vec{r}) + U_{\mathrm{Bend}}(\vec{r}) + U_{\mathrm{E}}(\vec{r})$ is the sum of the conservative potentials, with $U_{\mathrm{E}}(\vec{r}) = QV(\vec{r})$, and $-\xi\vec{v}$ is the damping force. The last term on the *rhs* is the uncorrelated noise that models the random kicks from the solvent; as usual, $\vec{R}(t)$ satisfies $\langle R_i(t)\rangle = 0$ and $\langle R_i(t)R_j(0)\rangle = \delta(t)\delta_{ij}$, where $\delta(t)$ is the Dirac delta function and i and j represent the Cartesian coordinates.

C. Static orientation

We first test the theory for static orientation in Sec. II B by simulating the equilibrium orientation of the rod-like molecules when their CM position is placed at different distances r right above the pore. The numerical results are in good agreement with theory, as shown in Fig. 3; the small deviations found for small values of r/R_θ are due to the non-radial field lines near the nanopore, as discussed in our previous paper.[26]

D. Orientation during capture

We now simulate the capture of a randomly oriented rod released far from the pore ($\lambda_e > r \gg R_\theta$) and evaluate its mean orientation $\Theta(r)$ from an ensemble of 5000 trajectories. How a rod-like molecule enters a pore depends on multiple factors, such as the pore-molecule interactions and the detailed field lines, but since this is not our focus here, we stop the simulation once the rod is at a distance of $r = L/2$ away from the nanopore.

As shown in Fig. 3, the dynamic order parameter curves $\Theta(r)$ also collapse if r is rescaled by $R_\theta(\lambda_e)$, implying that R_θ is again the relevant length scale. For distances $r < 3\ R_\theta$, however, the drift toward the pore is too fast for the rod to adapt to the local field conditions, and the order parameter is less than

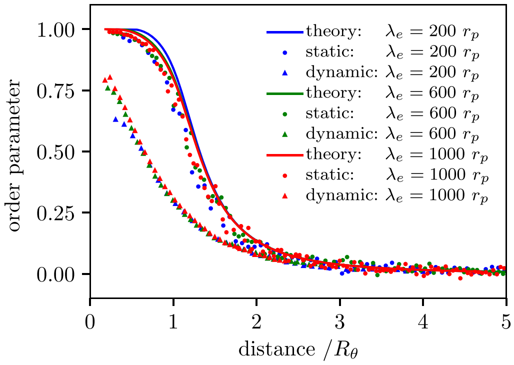

FIG. 3. Order parameter $\Theta(r)$ vs scaled distance r/R_θ for rods of length $L = \frac{10}{3}r_p$ and three field intensities λ_e (in units of r_p). The data points are from simulations, while the solid lines (theory) are from Eqs. (1) and (6). We show the results for fixed rods that are in equilibrium (marked theory and static) as well as for free rods moving toward the pore (dynamic).

that predicted by equilibrium theory for all three field intensities. The deviations can also be observed when looking at the orientation probability distribution function: Fig. 4 shows that the rods have a much larger probability of being unaligned than what is predicted by the equilibrium theory. The inset of Fig. 4 shows some capture trajectories with rods starting from different polar angles; because of the radial symmetry of the field (except near the pore), the trajectories and orientation statistics of the rods do not depend on this angle (note, however, that the rods starting very close to the wall are affected by the steric restrictions to rotational motion).

The fact that R_θ is also the relevant length scale for dynamic orientation can be understood as follows for a LD model. The time needed for the CM of the rod to move over a distance Δr is simply $\Delta t = \Delta r/v(r)$. The amount of rotation achieved during that time is $\Delta\theta \sim \Delta t/\tau_e$; using the expressions for Δt and τ_e given previously, we obtain the simple scaling $\Delta\theta/\Delta r \sim 1/r$. This has to be compared to the expected difference in equilibrium orientation, $\partial\langle\theta\rangle/\partial r$. The latter can be calculated in the $r \gg L$ limit using the approach given in Eqs. (4)–(6), giving $\partial\langle\theta\rangle/\partial r \sim \lambda_e L^2/r^4$. These two rates are equal at a distance of $r \sim (\lambda_e L^2)^{1/3} \sim R_\theta$. In other words, rod orientation is never in equilibrium during capture.

E. Effect of initial orientation

Figure 5 shows that the capture process is impacted by the fact that rod orientation is not in equilibrium with the local field if $r \lesssim R_\theta$. Molecules are first released from different initial vertical positions r with initial orientations in local static equilibrium (note that starting the rod along another polar angle gives the same results because of the radial symmetry of the field lines—data not shown). The black curve is the static order parameter (same as the inset of Fig. 2), while the gray data points show a case with the initial position $r \gg R_\theta$. Although the three curves corresponding to smaller initial distances tend to converge toward the gray curve, only one does so before reaching the pore. In the other two cases, i.e., for $r \lesssim 1.5R_\theta$, the initial rod orientations impact the entire capture trajectory.

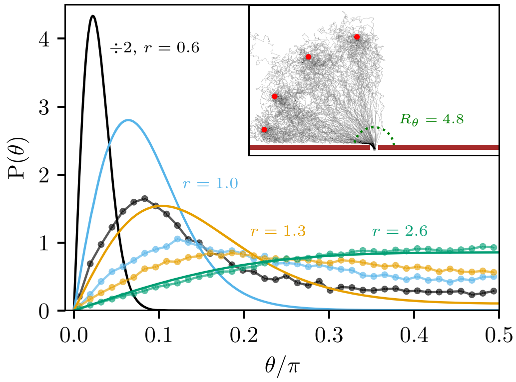

FIG. 4. Normalized probability distribution functions $P(\theta)$ for the local rod orientation θ at different radial distances from the pore (r = 0.6, 1, 1.3, and 2.6 R_θ); the field intensity is $\lambda_e = 600\ r_p$, the orientational capture radius is $R_\theta = 4.8\ r_p$, and the rods are launched from an initial radial distance of 27.6 r_p. The connected data points are from LD simulations (ensemble size of 40 000); each point corresponds to a bin size of $\pi/80$. The solid lines give the equilibrium distribution function $P(\theta) \sim \sin\theta \exp(-\delta\Psi_\theta(r)/k_BT)$. Inset: sample trajectories for rods launched from four different initial angles (red dots; the angles, from the wall, are $= \frac{\pi}{2}j$; j = 0.1, 0.3, 0.6, and 0.9). The green dashed line shows the orientational radius R_θ.

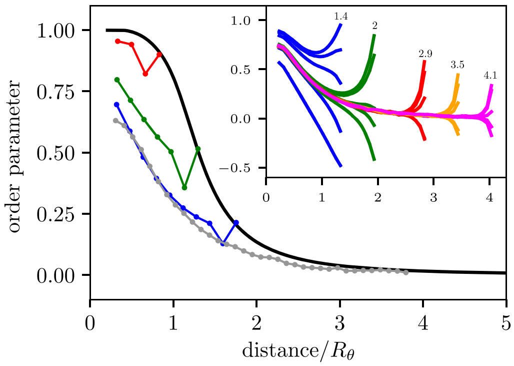

FIG. 5. Order parameter $\Theta(r)$ vs scaled distance r/R_θ for a field intensity of $\lambda_e = 1000\ r_p$. Main figure: Rods are launched from four different vertical initial positions r after their orientation has reached local equilibrium (given by the black curve). Inset: the rods are launched from five different initial positions r right above the nanopore and five different orientations ($\frac{i}{8}\pi$; i = 0, 1, 2, 3, 4). All curves are averaged over 5000 trajectories.

The memory effects are more obvious if we launch the rods with specific initial angles θ. For the inset of Fig. 5, we chose five different initial orientations, from perfectly aligned with to orthogonal to the local field lines. When the rods start at distances of $r \gtrsim 1.5R_\theta$, the initial orientation is rapidly lost and all trajectories converge to the one shown in gray in the main figure: reorientation is thus faster than capture. However, when the rods start at distances of $r \lesssim 1.5R_\theta$, the initial orientation affects the capture process and the curves do not merge before capture: the capture time of the rods then depends on both their initial position and orientation.

IV. CONCLUSIONS

Using scaling arguments, equilibrium calculations, and LD simulations, we showed that we need a second length scale (besides the nominal capture radius λ_e), the *orientational capture radius* $R_\theta = \sqrt[3]{\lambda_e L^2/60}$, in order to describe the capture of charged rods of length L by a nanopore. First, R_θ is the radial distance at which rods start orienting if their initial radial position is $r_o > R_\theta$. However, because rotational dynamics is slower than capture when $r_o < R_\theta$, the rods orient less than predicted by local equilibrium arguments. The last point also implies that if $r_o < R_\theta$, the final orientation of the rod at the pore does depend on its initial orientation. While the main part of Fig. 5 shows that rods starting at distances $r_o < R_\theta$ are, on average, more oriented when they reach the pore than those starting further, the inset shows that some actually orient less. These results must be taken into account when studying how rods enter nanopores.

The new length scale R_θ includes the two relevant lengths in this problem: the rod length L and the nominal capture radius λ_e. Under normal experimental conditions, one would have $\lambda_e \gg R_\theta \gg r_p$, and the rods are captured well before they orient. However, unless one uses high field intensities $\lambda_e \gg 60$, the value of R_θ may not be much larger than the length of the rod itself.

As shown above, the capture of a rod is affected by its initial orientation if $r_o < R_\theta$. To estimate the maximum impact on the capture time, let us consider two non-rotating rods, one starting parallel ($\parallel$) to the local field lines and the other starting perpendicular ($\perp$). The mean capture time of such a rod starting from distance $r < R_\theta$ would be $\tau_E(r) = \int_0^r dz/v(z) = r^3/\lambda_e D$. Since $D_\parallel \approx 2D_\perp$ for a rod, the difference in arrival times would be at most a factor of 2. However, since $\tau_E(R_\theta)/\tau_E(\lambda_e) = (R_\theta/\lambda_e)^3 \ll 1$, this is not expected to be important during experiments, unless one can manipulate rod orientations prior to or during the experiment.

Our theoretical analysis and LD simulations neglect all hydrodynamics/electrohydrodynamics effects; the latter are necessary to properly model the electrophoresis of a charged rod (e.g., the effective charge Q depends on ion concentration and the rod's aspect ratio[29,38–40]). More importantly, the friction coefficient of the rod is independent of its orientation in LD, with direct impact on rotation and capture times. In the case of flexible polymers, the electric field will orient *and* deform the molecules, with impact on the capture and translocation processes.[14,15] For nonlinear polymers and/or non-uniform charge distributions, the electric forces might orient the object very differently. These subtle issues will be addressed in future papers.

ACKNOWLEDGMENTS

Simulations were performed using ESPResSo 4.0[34] on Compute Canada's Cedar system. G.W.S. acknowledges the support of both the University of Ottawa and the Natural Sciences and Engineering Research Council of Canada (NSERC), funding Reference No. RGPIN/046434-2013. L.Q. was supported by the Chinese Scholarship Council and the University of Ottawa.

REFERENCES

[1] E. Beamish, V. Tabard-Cossa, and M. Godin, "Identifying structure in short DNA scaffolds using solid-state nanopores," ACS Sens. **2**, 1814–1820 (2017).

[2] M. Wanunu, T. Dadosh, V. Ray, J. Jin, L. McReynolds, and M. Drndić, "Rapid electronic detection of probe-specific microRNAs using thin nanopore sensors," Nat. Nanotechnol. **5**, 807–814 (2010).

[3] S. W. Kowalczyk, A. R. Hall, and C. Dekker, "Detection of local protein structures along DNA using solid-state nanopores," Nano Lett. **10**, 324–328 (2010).

[4] P. Waduge, R. Hu, P. Bandarkar, H. Yamazaki, B. Cressiot, Q. Zhao, P. C. Whitford, and M. Wanunu, "Nanopore-based measurements of protein size, fluctuations, and conformational changes," ACS Nano **11**, 5706–5716 (2017).

[5] E. Beamish, V. Tabard-Cossa, and M. Godin, "Programmable DNA nanoswitch sensing with solid-state nanopores," ACS Sens. **4**, 2458–2464 (2019).

[6] M. Charron, K. Briggs, S. King, M. Waugh, and V. Tabard-Cossa, "Precise DNA concentration measurements with nanopores by controlled counting," Anal. Chem. **91**, 12228–12237 (2019).

[7] L. He, P. Karau, and V. Tabard-Cossa, "Fast capture and multiplexed detection of short multi-arm DNA stars in solid-state nanopores," Nanoscale **11**, 16342–16350 (2019).

[8] P. Bandarkar, H. Yang, R. Henley, M. Wanunu, and P. C. Whitford, "How nanopore translocation experiments can measure RNA unfolding," Biophys. J. **118**, 1–9 (2020).

[9] M. H. Lam, K. Briggs, K. Kastritis, M. Magill, G. R. Madejski, J. L. McGrath, H. W. de Haan, and V. Tabard-Cossa, "Entropic trapping of DNA with a nanofiltered nanopore," ACS Appl. Nano Mater. **2**, 4773–4781 (2019).

[10] K. Briggs, G. Madejski, M. Magill, K. Kastritis, H. W. de Haan, J. L. McGrath, and V. Tabard-Cossa, "DNA translocations through nanopores under nanoscale preconfinement," Nano Lett. **18**, 660–668 (2018).

[11] E. C. Yusko, J. M. Johnson, S. Majd, P. Prangkio, R. C. Rollings, J. Li, J. Yang, and M. Mayer, "Controlling protein translocation through nanopores with bio-inspired fluid walls," Nat. Nanotechnol. **6**, 253–260 (2011).

[12] O. M. Eggenberger, G. Leriche, T. Koyanagi, C. Ying, J. Houghtaling, T. B. H. Schroeder, J. Yang, J. Li, A. Hall, and M. Mayer, "Fluid surface coatings for solid-state nanopores: Comparison of phospholipid bilayers and archaea-inspired lipid monolayers," Nanotechnology **30**, 325504 (2019).

[13] C. Plesa, N. van Loo, P. Ketterer, H. Dietz, and C. Dekker, "Velocity of DNA during translocation through a solid-state nanopore," Nano Lett. **15**, 732–737 (2015).

[14] F. Farahpour, A. Maleknejad, F. Varnik, and M. R. Ejtehadi, "Chain deformation in translocation phenomena," Soft Matter **9**, 2750–2759 (2013).

[15] S. C. Vollmer and H. W. de Haan, "Translocation is a nonequilibrium process at all stages: Simulating the capture and translocation of a polymer by a nanopore," J. Chem. Phys. **145**, 154902 (2016).

[16] J. Sarabadani, T. Ikonen, and T. Ala-Nissila, "Iso-flux tension propagation theory of driven polymer translocation: The role of initial configurations," J. Chem. Phys. **141**, 214907 (2014).

[17] S. Buyukdagli, J. Sarabadani, and T. Ala-Nissila, "Theoretical modeling of polymer translocation: From the electrohydrodynamics of short polymers to the fluctuating long polymers," Polymers **11**, 118 (2019).

[18] J. K. Rosenstein, M. Wanunu, C. A. Merchant, M. Drndic, and K. L. Shepard, "Integrated nanopore sensing platform with sub-microsecond temporal resolution," Nat. Methods **9**, 487–492 (2012).

[19] A. McMullen, H. W. de Haan, J. X. Tang, and D. Stein, "Stiff filamentous virus translocations through solid-state nanopores," Nat. Commun. **5**, 4171 (2014).

[20] K. E. Venta, M. B. Zanjani, X. Ye, G. Danda, C. B. Murray, J. R. Lukes, and M. Drndić, "Gold nanorod translocations and charge measurement through solid-state nanopores," Nano Lett. **14**, 5358–5364 (2014).

[21] J. M. Alonso, M. Ł. Górzny, and A. M. Bittner, "The physics of tobacco mosaic virus and virus-based devices in biotechnology," Trends Biotechnol. **31**, 530–538 (2013).

[22] C. Koch, F. J. Eber, C. Azucena, A. Förste, S. Walheim, T. Schimmel, A. M. Bittner, H. Jeske, H. Gliemann, S. Eiben, F. C. Geiger, and C. Wege, "Novel roles for well-known players: From tobacco mosaic virus pests to enzymatically active assemblies," Beilstein J. Nanotechnol. **7**, 613–629 (2016).

[23] A. Schmatulla, N. Maghelli, and O. Marti, "Micromechanical properties of tobacco mosaic viruses," J. Microsc. **225**, 264–268 (2007).

[24] H. Wu, Y. Chen, Q. Zhou, R. Wang, B. Xia, D. Ma, K. Luo, and Q. Liu, "Translocation of rigid rod-shaped virus through various solid-state nanopores," Anal. Chem. **88**, 2502–2510 (2016).

[25] Y. M. Nuwan, D. Y. Bandara, J. Tang, J. Saharia, L. W. Rogowski, C. W. Ahn, and M. J. Kim, "Characterization of flagellar filaments and flagellin through optical microscopy and label-free nanopore responsiveness," Anal. Chem. **91**, 13665–13674 (2019).

[26] L. Qiao, M. Ignacio, and G. W. Slater, "Voltage-driven translocation: Defining a capture radius," J. Chem. Phys. **151**, 244902 (2019).

[27] M. Wanunu, W. Morrison, Y. Rabin, A. Y. Grosberg, and A. Meller, "Electrostatic focusing of unlabelled DNA into nanoscale pores using a salt gradient," Nat. Nanotechnol. **5**, 160–165 (2010).

[28] S. W. Kowalczyk, A. Y. Grosberg, Y. Rabin, and C. Dekker, "Modeling the conductance and DNA blockade of solid-state nanopores," Nanotechnology **22**, 315101 (2011).

[29] A. Y. Grosberg and Y. Rabin, "DNA capture into a nanopore: Interplay of diffusion and electrohydrodynamics," J. Chem. Phys. **133**, 165102 (2010).

[30] G. W. Slater and J. Noolandi, "New biased-reptation model for charged polymers," Phys. Rev. Lett. **55**, 1579–1582 (1985).

[31] G. W. Slater, S. J. Hubert, and G. I. Nixon, "Construction of approximate entropic forces for finitely extensible nonlinear elastic (FENE) polymers," Macromol. Theory Simul. **3**, 695–704 (1994).

[32] M. Doi, "Rotational relaxation time of rigid rod-like macromolecule in concentrated solution," J. Phys. France **36**, 607–611 (1975).

[33] G. W. Slater, C. Holm, M. V. Chubynsky, H. W. de Haan, A. Dubé, K. Grass, O. A. Hickey, C. Kingsburry, D. Sean, T. N. Shendruk, and L. Zhan, "Modeling the separation of macromolecules: A review of current computer simulation methods," Electrophoresis **30**, 792–818 (2009).

[34] F. Weik, R. Weeber, K. Szuttor, K. Breitsprecher, J. de Graaf, M. Kuron, J. Landsgesell, H. Menke, D. Sean, and C. Holm, "ESPResSo 4.0 – an extensible software package for simulating soft matter systems," Eur. Phys. J. Spec. Top. **227**, 1789–1816 (2019).

[35] J. D. Weeks, D. Chandler, and H. C. Andersen, "Role of repulsive forces in determining the equilibrium structure of simple liquids," J. Chem. Phys. **54**, 5237–5247 (1971).

[36] G. S. Grest and K. Kremer, "Molecular dynamics simulation for polymers in the presence of a heat bath," Phys. Rev. A **33**, 3628–3631 (1986).

[37] D. Sean and G. W. Slater, "Langevin dynamcis simulations of driven polymer translocation into a cross-linked gel," Electrophoresis **38**, 653–658 (2017).

[38] S. A. Allison and S. Mazur, "Modeling the free solution electrophoretic mobility of short DNA fragments," Biopolymers **46**, 359–373 (1998).

[39] S. A. Allison, H. Pei, S. Baek, J. Brown, M. Y. Lee, V. Nguyen, U. T. Twahir, and H. Wu, "The dependence of the electrophoretic mobility of small organic ions on ionic strength and complex formation," Electrophoresis **31**, 920–932 (2010).

[40] S. Allison, C. Chen, and D. Stigter, "The length dependence of translational diffusion, free solution electrophoretic mobility, and electrophoretic tether force of rigid rod-like model duplex DNA," Biophys. J. **81**, 2558–2568 (2001).

7

Capture and translocation of a rod-like molecule by a nanopore : orientation, charge distribution and hydrodynamics

Manuscript to be submitted.

Capture and translocation of a rod-like molecule by a nanopore: orientation, charge distribution and hydrodynamics

Le Qiao, Gary W. Slater[1]

Department of Physics, University of Ottawa, Ottawa, Ontario K1N 6N5, Canada

(Dated: June 2, 2021)

We investigate the translocation of rods with different charge distributions using hybrid Langevin Dynamics and Lattice Boltzmann (LD-LB) simulations. Electrostatic interactions are added to the system using the P^3M algorithm to model the electro-hydrodynamic interactions (EHI). We first examine the free-solution electrophoretic properties of rods with various charge distributions. Our translocation simulation results suggest that the order parameter is asymmetric during the capture and escape processes despite the symmetric electric field lines, while the impacts of the charge distribution on rod orientation are more significant during the capture process. The capture/threading/escape times are under the combined effects of charge screening, rod orientation, and charge distributions. We also show that steric and hydrodynamic interactions with the wall speed up the capture process. Remarkably, the *orientational capture radius* we proposed previously for uniformly charged rods is still valid in the presence of EHI.

I. INTRODUCTION

The voltage-driven translocation of analytes through a nanopore has attracted a lot of attention due to its potential application to molecular detection in general[1–3], and DNA gene sequencing[4–6] in particular. In short, an electric field is used to force the analyte through the nanopore (or nanochannel); during this translocation process, the analyte blocks part of the ionic current through the channel. A current meter is thus employed to detect and characterize the analytes, including large ions, nanoparticles, viruses, and charged polymers such as DNAs, RNAs, proteins, and other polyelectrolytes. A wide range of experimental, theoretical, and computational studies have been conducted to understand the mechanisms of translocation[6–9].

While translocation is now better understood, our understanding of the physics of the capture process remains incomplete. This process is both subtle and complex; for instance, it is potentially affected by thermal diffusion, drift due to external perturbations, long-range hydrodynamic interactions, and fluid flow. Furthermore, different analytes react differently to the same conditions; for example, the electrophoretic dynamics of uniformly charged spherical particles are fairly straightforward, while for anisotropic objects such as rod-like polymers, the direction of net motion may not align with the local electric field.

We previously investigated the capture of point-like particles with a focus on the definition of the capture radius[10], the time dependence of the capture rate, the size of the depletion zone, and the effects of the boundary conditions[11]. We also examined the orientation of rod-like polymers during capture using simple theoretical arguments and a Langevin Dynamics (LD) simulation approach[12] (thus neglecting long-ranged electrohydrodynamic interactions, EHI): this led us to introduce the concept of an orientational capture radius R_θ.

Waszkiewicz *et al.*[13] further extended our work on rod orientation during the capture process by considering anisotropic diffusivity and wall hindered hydrodynamic interactions in their analytical and numerical calculations. They recovered the orientational capture radius we defined previously and concluded that rods do not follow field lines during capture due to the anisotropic diffusion[12]. Furthermore, they showed that the trajectory of a rod towards the nanopore depends on its initial orientation and position because of the near-wall hydrodynamic interactions (these interactions were missing in our previous work). However, the electrostatic interactions between the rod and the ions in solution are still missing in their calculation; such interactions can change the dynamics, for instance when the rod is in the high field region near (or inside) the nanopore or when the rod is not uniformly charged. The main goal of the current paper is to examine these effects.

The availability of powerful GPUs and new hybrid simulation algorithms allows us to efficiently simulate molecular dynamics with EHI even for fairly large systems[14]. As an extension to our previous LD simulations and Waszkiewicz *et al.*'s calculations, we now report the results of a study of the capture and translocation of a stiff rod molecule modeled using a coarse-grained raspberry-like structure coupled to the salt-containing solvent via a lattice-Boltzmann (LB) algorithm. In order to illustrate the impacts of charge screening, EHI and rod orientation, we first examine the free solution electrophoresis of rods with different charge distributions and compare the simulation results to those obtained when a sedimentation-like mechanical force is used. We then investigate the impact of EHI on the capture and translocation processes, with emphasis on the difference between small analytes and rods.

II. SIMULATION DETAILS

We simulate rod capture and translocation using a hybrid simulation approach that includes (1) a LD simulation algorithm for the motion of the rod and ions, (2) a LB method for the fluid, and (3) a particle-particle-particle-mesh (P^3M) algorithm for the electrostatic interactions. The simulations were carried out using the ESPResSo package[15].

A. The raspberry rod model

In this section, we construct a rigid rod-like polymeric molecule of length $L \ll L_P$, where L_P is the persistence length, using the "raspberry" approach[16–19]. The general idea of the raspberry approach is to fill the target object with enough beads (all of which interact with the LB fluid[20]) in order to properly model its hydrodynamics properties. As shown in Fig. 1, our rods are built by piling up N raspberry disks (1a) that each contain $1 + 6 + 12 = 19$ beads in three concentric layers. The beads have a radius $\frac{1}{2}\sigma$, where σ is the fundamental length in our simulation. Therefore, the nominal diameter of the rod is $d = 5\,\sigma$ while its length is $L = N\sigma$. To make the rod rigid, all the beads are fixed in their relative position by linking them to the bead at the centre of mass via rigid bonds.

In this paper, we also study the impact of the charge distribution on the capture process. Figures 1 b-f show different scenarios of interest. In b-c the total charge is $Q = 2N \times e$, but these charges are distributed differently along the surface of the rod. The last three rods (d-e-f) have charges over only one half of their length; if we divide these rods into four segments, the charges can symbolically be described as $[0 : 0 : \frac{Q}{2} : \frac{Q}{2}]$, $[0 : \frac{Q}{2} : \frac{Q}{2} : 0]$ and $[\frac{Q}{2} : 0 : 0 : \frac{Q}{2}]$, respectively. In real units, if we choose $\sigma = 0.4\,nm$, then the rod-like dsDNA structure has a diameter $d = 2\,nm$ and the distance between basepairs is $\sigma = 0.4\,nm$.

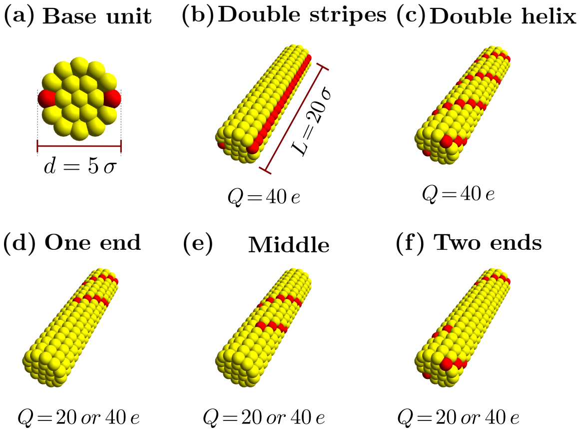

Figure 1. Raspberry rods of length $L = 20\,\sigma$ with different charge distributions (the charged beads are in red and the total charge is given by Q). (a) The basic disk-shaped building block. (b) The charges are lined up along two stripes. (c) A double-helix charge distribution. (d) One half of the rod is like c while the other is uncharged. (e) Similar to d, but the charged part is in the centre. (f) Same as d, but the charges are distributed only near the two ends.

B. Coupling the Lattice Boltzmann solver with LD

We use the GPU based LB solver with D3Q19 lattice model built in the ESPResSo package to simulate the fluid, which we connect to the LD description of the rod and ions via a force coupling method[20]. The coupling is implemented using a friction force $\boldsymbol{F}_\gamma = -\gamma(\boldsymbol{v} - \boldsymbol{u}_b)$, where γ is the friction coefficient, $\boldsymbol{v}$ is the bead's velocity and $\boldsymbol{u}_b$ is the fluid velocity at the bead position. An opposite force is applied to the fluid to conserve the momentum of the overall system. A zero-mean random force with a second moment that depends on temperature is added to both beads and fluid according to the fluctuation-dissipation theorem. For a bead of mass m, the equation of motion is thus

$$m\dot{\mathbf{v}} = \boldsymbol{\nabla} U(\mathbf{r}) + \boldsymbol{F}_{\gamma} + \sqrt{2\gamma k_{\mathrm{B}}T}\;\mathbf{R}(\boldsymbol{r},t), \tag{1}$$

where $\boldsymbol{\nabla} U(\mathbf{r}) = \boldsymbol{\nabla}(U_{\mathrm{WCA}} + U_{\mathrm{c}} + U_{\mathrm{E}})$ is the sum of the conservative forces, U_{WCA} is the repulsive Weeks-Chandler-Anderson (WCA) potential between the rod beads, the ion beads and the wall:

$$U_{\mathrm{WCA}}(r) = \begin{cases} 4\epsilon\left[\left(\frac{\sigma}{r}\right)^{12} - \left(\frac{\sigma}{r}\right)^{6}\right] + \epsilon & \text{for } r < r_c \\ 0 & \text{for } r \geq r_c. \end{cases} \tag{2}$$

We use $\epsilon = k_B T$ as the fundamental unit of energy in our simulations, and $r_c = 2^{1/6}\,\sigma$ is the cutoff length that makes U_{WCA} purely repulsive. $U_{\mathrm{E}}(\mathbf{r})$ is the external electric potential, $U_{\mathrm{c}}(\mathbf{r})$ is the electrostatic energy due to the charged beads. The last term is the stochastic component that models the effects of Brownian motion; the random variable $\mathbf{R}(\boldsymbol{r},t)$ satisfies $\langle \boldsymbol{R}(\boldsymbol{r},t)\rangle = 0$ and

$$\langle \boldsymbol{R}(\boldsymbol{r},t)\boldsymbol{R}(\boldsymbol{r'},t')\rangle = \delta(t-t')\delta(\boldsymbol{r}-\boldsymbol{r'}) \ , \tag{3}$$

where $\delta(z)$ is the Dirac delta function. The electrostatic interactions are calculated using the P^3M algorithmic[21,22]. The electrostatic energy between two beads of charge q_i and q_j at distance r is $U_{\mathrm{c}}(\boldsymbol{r}) = c\frac{q_i q_j}{r}$, where $c = \ell_B k_B T/e^2$ with $\ell_B = e^2/4\pi\varepsilon k_B T$ the Bjerrum length and ε the permittivity of the medium. The Bjerrum length is set to $\ell_B = 1.8\,\sigma$ and we tune P^3M to obtain an accuracy of $10^{-3}\,\epsilon/\sigma$ for the electrostatic force.

Our unit of time $\tau_o = \sigma^2\gamma/k_B T$ is the time needed for a bead to diffuse over a distance σ, and the integration time step is $\Delta t = 0.01\,\tau_o$ for both the LD and LB algorithms. The parameters are chosen to match the coarse grained LB dsDNA model from ref[19]. For instance, the friction coefficient is $\gamma = 7\,m/\tau_o$, the LB kinematic viscosity is set to $\eta = 0.6\,\sigma^2/\tau_o$, the fluid density is $\rho = 1\,m/\sigma^2$, and the LB lattice size is σ. The mobilities are in units of $\mu_o = 1\,\sigma^2 e/\tau_o\epsilon$. We use $C_s^o = 0.0385\,\sigma^{-3}$ as the unit of concentration for single valence salts (this corresponds to $1\,mol/L$ when $\sigma = 0.4\,nm$). Note however that our goal is to study the impact of hydrodynamics rather than match our data to a specific experimental system.

III. FREE SOLUTION ELECTROPHORESIS

In this section, we compare the electrophoresis of rods in free solution (with different charge distributions and in various salt concentrations) to the drift motion of the same rods under an equivalent mechanical force.

In the presence of a uniform electric field, the cloud of counterions (which has a thickness $\lambda_D = \sqrt{\frac{\varepsilon k_B T}{2e^2 C}}$, the Debye length for single valence salts; as an example, we obtain $\lambda_D \approxeq 1.75\,nm$ when $C_s = 0.03\,C_s^o = 0.03\,M$) surrounding the analyte moves in the direction opposite to the latter; the net motion of the analyte thus depends on both its size and λ_D. Note that in the case of rods, Manning condensation[23,24] may reduce the linear charge density to e/ℓ_B if it exceeds this critical value.

We carry out two different types of free-solution simulations (Fig. 2). First, we apply an electric field $\boldsymbol{E}$ to all charged beads (including the ions in solution) to simulate electrophoresis. And then we repeat the simulations while only applying the field to the charged beads on the rod (a weak force must also be applied to the fluid in the opposite direction in order to conserve momentum); this is equivalent to applying a mechanical force $\boldsymbol{F_m} = Q\boldsymbol{E}$ to the rod (all the other electrostatic interactions are kept).

For our purposes here, we define the electrophoretic mobility as the constant linking the mean magnitude of the instantaneous velocity and the magnitude of the applied field:

$$\langle|\boldsymbol{v_e}|\rangle = \mu_e|\boldsymbol{E}|. \tag{4}$$

Taking the norm ($|\ldots|$) is not necessary when the velocity and the force point in the same direction, but this is not always the case for rods when EHI effects are included, as we shall see. Similarly, we define the friction coefficient in the presence of the external mechanical force using the expression

$$|\boldsymbol{F_m}| = \gamma_m\langle|\boldsymbol{v_m}|\rangle\ . \tag{5}$$

To characterize rod orientation, we use the order parameter[12]

$$\Theta = \tfrac{1}{2}\left[3\langle\cos^2\theta\rangle - 1\right] \tag{6}$$

where θ is the angle between the direction of the force and the rod's principal axis.

Figures 3a and b show that the rods' electrophoretic mobility μ_e and equivalent mechanical mobility $\mu_m = Q/\gamma_m$ behave differently when we change the salt concentration C_s: while

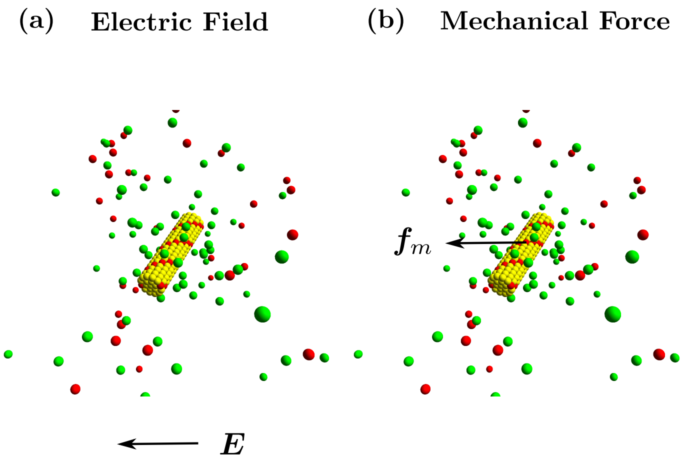

Figure 2. Our two free-solution simulation schemes. The green and red beads are counterions and coions, respectively. (a) An electric field $\boldsymbol{E}$ affects all charged components. (b) A mechanical force is applied only to the charged beads located on the rod.

μ_e decreases when we increase C_s, as expected, μ_m is unaffected. Figure 3c, together with Figs. 3a-b and Table I (which gives the mobilities and orientations for $C_s = 0.03\, C_s^o$), clarify the physics of the problem. Let us summarize the main elements:

- When the force is applied at only one of its ends, the rod tends to align along the direction of the field ($\Theta \to 1$).
- Since mechanical friction is smaller when the rod is aligned (i.e., $\gamma_{\parallel} < \gamma_{\perp}$), μ_m increases with orientation. For example, μ_m is ≈ 1.3 times larger when only one end is pulled by the mechanical force – Table I.
- Despite the increased orientation obtained when the electric charge is at only one end, μ_e is actually smaller than for a uniformly charged rod. This is due to the fact that Manning condensation is more intense for partially charged rods (1ed40, 2ed40, mid40) since they have a higher local linear charge density.
- When considering only partially charged rods, the electrophoretic mobilities are ranked in this order: $\mu_e(1ed) > \mu_e(2ed) > \mu_e(mid)$. This indicates that the charge conden-

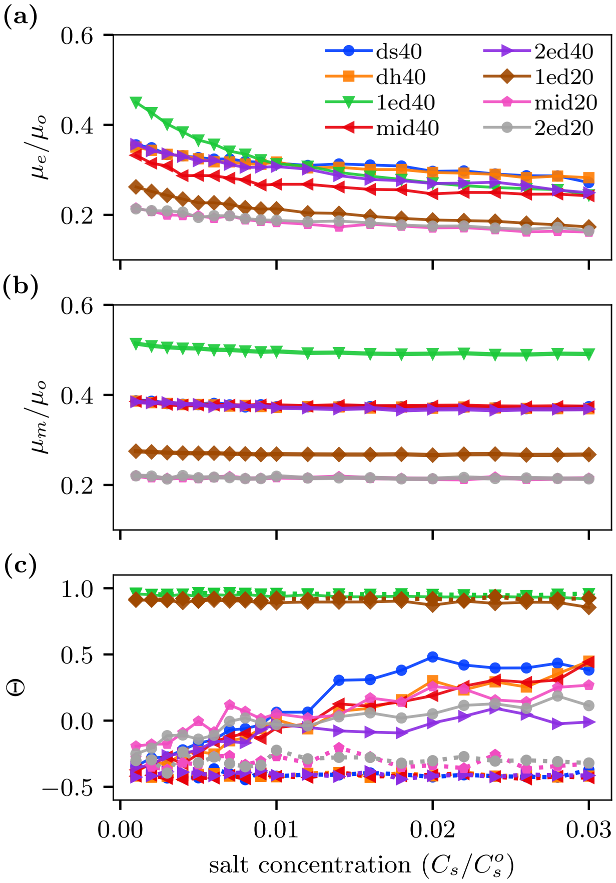

Figure 3. (a) Scaled electrophoretic mobility μ_e/μ_o; (b) scaled mechanical mobility μ_m/μ_o; and (c) order parameter Θ, *vs* the salt concentration C_s/C_s^o, for different charge distributions. The results are averages over long trajectories (10^5 integration steps) starting with 10 random initial orientations. In panel (c), the dashed (solid) lines correspond to the mechanical (electrical) case. Legend: The codes read AB, where the A is for charge location (ds for double-striped, dh for double helix; 1ed and 2ed for one or two end; mid for middle) and B is the total bare charge Q/e. The electric/mechanical force applied to the charged sites on the rod is of magnitude $1\,\frac{\epsilon}{\sigma e}$.

sation and the electrophoretic force have different weights along the rod[25,26]. Interestingly, given the same charge distribution, when the charge is reduced by half, the mobility is only reduced by $\frac{1}{3}$, again showing the combined effects of orientation and condensation.

- When the mechanical force is applied uniformly along the rod, the latter tends to orient perpendicular to the force ($\Theta \to -\frac{1}{2}$), similar to what was reported in[27,28].
- When we electrophorese a uniformly charged rod, on the other hand, we observe an interesting transition: the rod orients perpendicular to the field at low salt concentration (in which case λ_D is too large to be a factor) while $\Theta_e \approx 0 - 0.5$ at high salt concentration. This is a good example of the Smoluchowski-Hückel transition that we expect when the salt concentration is changed.

Charge Distribution	Q/e	μ_e/μ_o	μ_m/μ_o	Θ_e	Θ_m
Double stripes	40	0.280	0.374	0.47	-0.37
Double helix	40	0.283	0.369	0.46	-0.42
One end	40	0.246	0.491	0.92	0.96
Middle	40	0.236	0.374	0.33	-0.43
Two ends	40	0.244	0.369	-0.05	-0.41
One end	20	0.174	0.268	0.86	0.93
Middle	20	0.160	0.215	0.20	-0.33
Two ends	20	0.162	0.214	0.08	-0.32

Table I. Scaled mobilities $\mu_e/\mu_o\,(\pm 0.003)$ and $\mu_m/\mu_o\,(\pm 0.001)$, and order parameters $\Theta_e\,(\pm 0.05)$ and $\Theta_m\,(\pm 0.01)$, for different charge distributions in a salt concentration $C_s = 0.03\,C_s^o$.

We also investigated the correlation between the directions of the instantaneous velocity and of the rod axis. Figure 4 shows the angle between the velocity and the rod axis *vs* the angle between the force and the rod axis for both electric and mechanical forces. The diagonal dashed lines correspond to the velocity being aligned with the local field. Obviously, the velocity is not perfectly parallel to the field direction, except when the rod is oriented parallel or perpendicular to the field ($\theta = 0$ or $\pi/2$).

Using the double helix (dh) charged rod as an example, the deviation reaches a maximum value of $\approx 10°$ when the rod makes an angle of $\theta \approx \pi/3$ with the field. Moreover, when we increase the field intensity, the rod is more frequently oriented perpendicular with the field direction ($\theta \to \pi/2$) while the fluctuations are much reduced; this is also observed when we use a mechanical force.

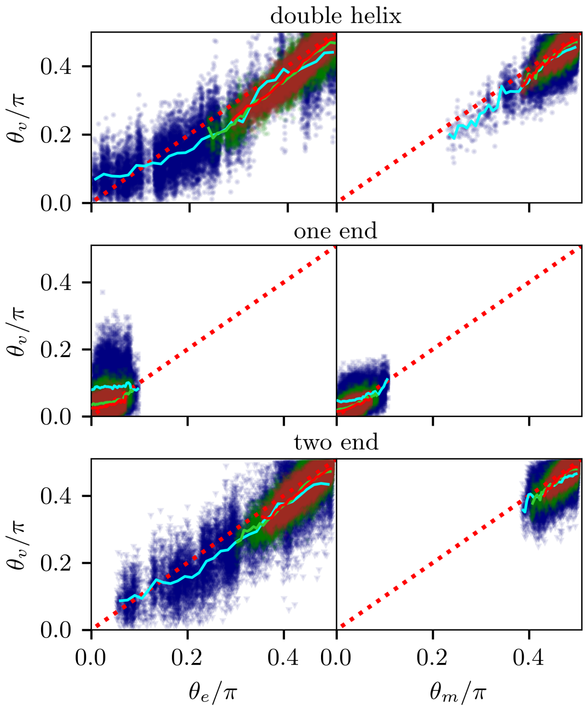

Figure 4. Correlation between the directions of the local velocity and of the local external field/force for a rod of charge $Q = 40\,e$ with different charge distributions. θ_v is the angle between velocity and the rod axis, θ_e (or θ_m) is the angle between the rod axis and the direction of the electric (mechanical) force. Scattered data points are instantaneous values and the solid curves are averages. The red dashed lines show $\theta_v = \theta_e$ and $\theta_v = \theta_m$. The colors code for the magnitude of the force applied to the charged sites on the rod: the values are 1 (*blue*), 2 (*green*), 3 (*brown*) $\frac{\epsilon}{\sigma e}$. The salt concentration $C_s/C_s^o = 0.03$ is used for these simulations.

The situation is entirely opposite for the one-end (1ed) charged rod, which tends to orient with the field/force even when the force is small. The two-end (2ed) charged rod is more or less the same as the double-helix rod, although this rod seems to prefer perpendicular orientations under a mechanical force.

Our free solution electrophoresis simulations thus indicate that a rod can orient with the field even under an uniform field at high salt concentrations. The hydrodynamic interactions can make the rod move in a direction different from that of the applied force. This last point suggests that the rod will move between field lines when the latter are converging (this is the case during the capture process), a phenomenon that we will observe in the next section.

IV. ORIENTATION DURATION CAPTURE

A. Simulation setup

We now set up a translocation simulation system with a periodic box of size $L_x = L_y = \frac{1}{2}\,L_z = 6\,L$ and an impenetrable wall with a nanopore in its centre. The radius of the pore is $r_p = \frac{5}{4}\,d = \frac{25}{4}\,\sigma$ and the length $\ell_p = r_p$. The charged rod is initialized on the *cis* side as shown in Fig. 5. We also randomly add $N_c = 2\,N$ explicit counterions beads and $N_s = 2\,CV_{box}$ single valence salt ions to the system, where $C_s = 0.03\,C_s^o$ is the salt concentration and $V_{box} = L_xL_y(L_z - \ell_p) + \pi r_p^2 \ell_p$ is the accessible volume (this excludes the impenetrable wall).

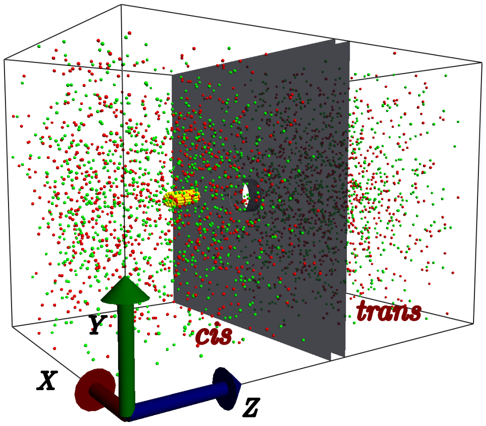

Figure 5. Snapshot of the simulation system for a double-helix rod molecule with a salt concentration $C_s = 0.03\,C_s^o$. The colored beads in solution represent cations (green) and anions (red).

The electrostatic potential outside the pore is given by[29].

$$V(\zeta,\beta,\phi) = \Delta V\;\frac{r_e}{r_p}\;\arctan\left[\sinh(\zeta)\right], \tag{7}$$

where ΔV is the total potential difference across the device, $r_e = r_p/(\frac{2\ell_p}{r_p} + \pi) = r_p/(2+\pi)$ is the electrostatic length of the nanochannel, and $\zeta \in (-\infty,+\infty)$, $\beta \in [0,\pi]$ and $\phi \in [0,2\pi]$

are the oblate spherical coordinates[29]. The potential drop across the channel is

$$\delta V = \Delta V \times \frac{2\ell_p r_e}{r_p^2}, \tag{8}$$

corresponding to a uniform electric field

$$E_p = \frac{\delta V}{\ell_p} = \Delta V \times \frac{2r_e}{r_p^2}. \tag{9}$$

B. Orientation during capture and escape

In order to illustrate the impacts of the charge distribution on the orientation of the rod during the capture and translocation processes, we show how the order parameter $\Theta(r)$ depends on the radial distance to the pore (r) in Fig. 6a. We present two different order parameters: Θ_E uses the angle between the rod axis and direction $\hat{\boldsymbol{E}}_{\boldsymbol{CM}}$ of the field at the centre-of-mass of the rod, while Θ_z uses the pore axis $\hat{\boldsymbol{z}}$ instead. Several trajectories are shown in Fig. 6b for the case of a double-striped rod.

Despite the fact that all of the rods are launched from the same position, right above the nanopore (the black dot in Fig. 6b), they follow different trajectories and spread widely before arriving at the nanopore. Figure 6a shows that the rod is oriented along the local field direction $\hat{\boldsymbol{E}}_{\boldsymbol{CM}}$ and not along the nanochannel axis $\hat{\boldsymbol{z}}$. The two order parameters do not merge until the rod is engaged in the nanopore, which suggests that the rod tends to enter the pore sideways even when starting right above the nanopore. There are three reasons for this: (1) Rods diffuse in random directions before entering the high field region. (2) When a rod is already in the high-field region but not fully aligned with the local field, it tends to jump between field lines. (3) The field is higher near the pore edges[10]. The trajectories in Fig. 6b also show that rods tend to move along the wall (note the depletion region right above the pore). The two order parameters converge at the pore because the entry process aligns the rod with the pore axis $\hat{\boldsymbol{z}}$.

Although the field lines are identical on both sides of the wall, we observe a clear asymmetry in the rod orientation: the orientation is kept for a larger radial distance when escaping from the pore. More strikingly, there is little difference between the Θ_E and Θ_z.

Rods with different charge distributions follow different $\Theta(r)$ *vs* r curves during the capture process. For $Q = 40\,e$, the rod with charges at both ends tends to be more oriented

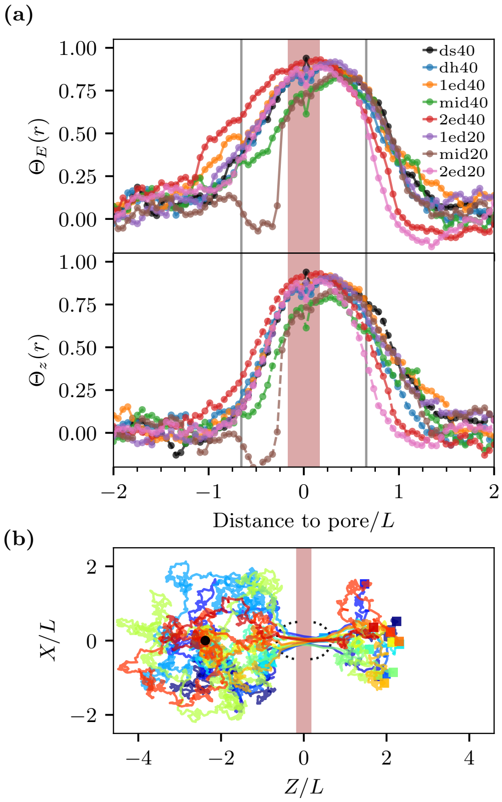

Figure 6. (a) Order parameters $\Theta_E(r)$ and $\Theta_E(r)$ *vs* scaled distance to the pore, r/L, for rods with various charge distributions. The rods start with random initial orientations, right above the nanopore at a distance of $r = 2.2\,L$ from the centre of the pore entrance (see the ● symbol in b below) and stop when they arrive the same distance from the centre of the pore exit on the *trans* side (■). The applied potential is $\Delta V = 15.6\,k_BT/e$. The vertical lines are at a distance $L/2$ from the wall (the latter is marked by the shaded area). Each curve is averaged from 50 simulations using a salt concentration $C_s/C_s^o = 0.03$. (b) Trajectories of ds40 rods projected on the XZ plane. Two doted semi-cycles indicates the CM position when the rod first enter/exit the nanopore.

than the rod charged at only one end, followed by the uniformly charged rods (both dh40 and ds40). The rod with middle charges, on the other hand, is the least oriented.

When reducing the charge to $Q = 20\,e$, similar results are found, except for the rod charged in the middle, which shows no orientation until it is well inside the nanopore. In the latter case, the negative values of $\Theta_z(r)$ near the nanopore pore indicate that these rods arrive misoriented and thus require large amount of time to enter the nanopore (see Table II). Overall, the fact $\Theta_z(r) < \Theta_E(r)$ suggests that rods enter the nanopore from the side despite being launched right above it. During the escape process, the rods follow roughly the same $\Theta(r)$ curves except for the two-end charged rods, which disorient faster.

As shown in Table II, rods charged at only one end enter the nanopore via this end while there is no preference for the other rods. The data also show that the capture time is roughly the same for rods that have the same type of charge distribution but different charges ($Q = 20\,e$ *vs* $40\,e$), a consequence of Manning condensation. The same effect also explains why chains with the same total charge $Q = 40\,e$ but different distributions have different capture times (*e.g.*, double-helix *vs* one end).

Clearly, the translocation times are directly impacted by both the bare charge density and the location of this charge (note that because the wall thickness is $< L/2$, we have cases where the rod segment inside the channel is neutral during part of the translocation process). Moreover, the nature of the pore-rod and hydrodynamic interactions inside the channel may also impact the translocation times.

Finally, we see in Table II that although the escape times are about three times smaller than the capture times, the relative escape times are very similar.

Charge distribution	Q/e	P	τ_c	τ_t	τ_e
Double stripes	40	1/2	1	1	1
Double helix	40	1/2	1.0	1.0	1.0
One end	40	1	1.3	2.2	1.1
Middle	40	1/2	1.4	1.6	1.2
Two ends	40	1/2	1.0	1.1	1.0
One end	20	1	1.2	2.7	1.3
Middle	20	1/2	6.0	2.9	1.1
Two ends	20	1/2	1.3	1.5	1.1

Table II. Probability P for the rod to enter the nanopore via a pre-determined end (the charged one for the one-end cases); capture time τ_c; translocation time τ_t; and escape time τ_e for different rod types and nominal charges Q. The times are normalized by the values found for the two-stripe case (first line), i.e., $3.1(5) \times 10^4$, $2.5(2) \times 10^2$, and $0.7(3) \times 10^4\,\tau_o$, respectively.

C. Initial orientations

In this section, we examine whether the initial orientation of a rod has an impact on its capture time. We place the randomly oriented rods at a distance L from the entrance of the nanopore; as shown in Fig. 7a, we start them from three different angular positions (polar angles). Since they start their journey very close to the pore, we know the field gradient will modify their initial orientation well before they reach the pore.

For the rods starting right above the nanopore (black line) in Fig. 7, the capture time is almost flat for all initial orientations θ_o. However, for the other two polar angles ϕ_o, the capture time is a strong function of the initial orientation, with perpendicular orientations taking twice as much time as parallel ones. Rods that start nearly aligned with the local field direction encounter less friction from the start. These results are consistent with our previous investigations[10].

The capture time for the different initial angular positions converges to roughly the same value when the rod is initially perpendicular to the local field because the time for the rod to rotate and align with the field then dominates the capture time. However, when the rods are already aligned with the field lines and start close to the wall, the presence of the wall helps the rod maintain its alignment and the capture time is shorter, similar to what is reported in ref[13].

D. Orientational capture radius

We previously proposed an orientational radius R_θ to characterize the rod orientation during capture but we did not consider electrohydrodynamic interactions[12]: this orientational capture radius depends on the field intensity and the length of the rod,

$$R_\theta = \left(\tfrac{1}{60}\lambda_e L^2\right)^{1/3}, \tag{10}$$

where λ_e is the capture radius[10],

$$\lambda_e = \frac{\tilde{Q}\Delta V}{k_B T}\; r_e \tag{11}$$

with $\tilde{Q}$ the effective electrophoretic charge of the analyte.

We now revisit the problem by considering the effects EHI might have on a double-helix rod. If we assume that the charge of the rod stays constant for different field intensities,

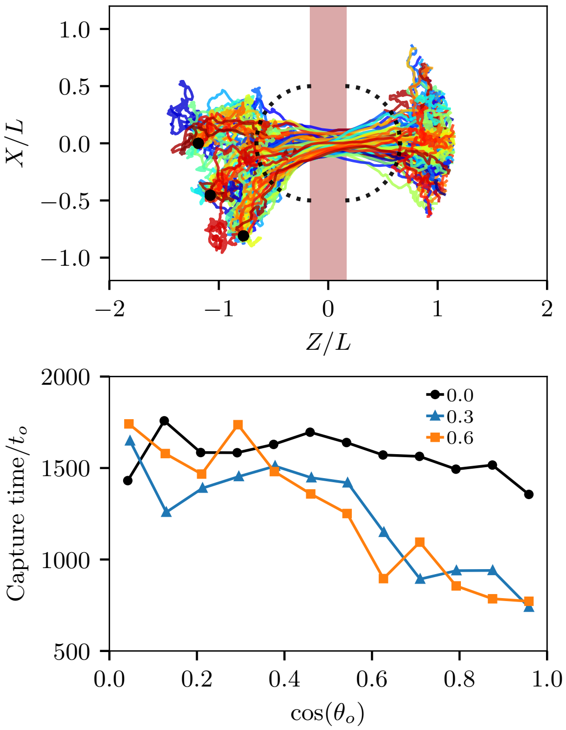

Figure 7. (a) Centre-of-mass trajectories of double-helix rods with $Q = 40\,e$ (or dh40) during translocation, projected on the XZ plane. The three black filled circles indicate the initial positions, all at a distance $r = L$ from the pore centre at $[0, 0, -\frac{1}{2}\ell_p]$ but with varying polar angles $\phi_o \in [0, 0.3, 0.6] \times \frac{\pi}{2}$ from the pore axis. Two doted half circles indicate the CM position when the rod first enter/exit the nanopore. (b) Capture time *vs* initial rod orientation for the same three different initial polar angles ϕ_o. The rod is parallel to the local field when $\cos(\theta_o) = 1$ and perpendicular when $\cos(\theta_o) = 0$. Each curve is an average over 150 translocation simulations; the salt concentration is $C_s/C_s^o = 0.03$.

the orientational radius should only depend on the applied voltage, with $R_\theta \sim \lambda_e^{1/3} \sim \Delta V^{1/3}$. In order to test this voltage dependence, we simulated the capture of the rod by applying different voltages $\Delta V = 15.6,\ 31.2$ and $46.8\,\frac{k_BT}{e}$. Our data do indeed collapse when $\Theta(r, \Delta V)$ is plotted *vs* $r/\Delta V^{1/3}$ (data not shown) despite the presence of EHI.

A more complete investigation of the effects of the EHI on rod orientation would need an estimate of $R_\theta = \left(\frac{1}{60}\lambda_e L^2\right)^{1/3}$. The key step is thus to calculate the rod's effective charge $\tilde{Q}$ in order to obtain $\lambda_e = \frac{\tilde{Q}\Delta V}{k_B T}\, r_e$. For a spherical analyte, the effective charge can be estimated from the electrophoretic mobility μ using the expression $\tilde{Q} = \mu\frac{k_B T}{D}$, where D is the diffusion coefficient of the analyte. We assume that the rod starts orienting (along the direction of the local electric field) only when it reaches the orientational radius at $r = R_\theta$. The rod's local mobility and orientation are then approximately given by the values obtained in the uniform electric field case in Sec. III and Table I: $\Theta \approxeq 0.46$ and $\mu_e \approxeq 0.283\,\mu_o$. Its friction coefficient $\gamma_m = \frac{k_B T}{D}$ at this location should be that obtained under a mechanical force when the rod has the same mean orientation. We use the friction coefficient measured when the mechanical force is applied only at one end because this is the case that most resembles the orientation of the double-helix rod. Rewriting eq. 5, one gets $\gamma_m = \frac{|\boldsymbol{F_m}|}{|\langle \boldsymbol{v_m} \rangle|} = \frac{1}{\mu_m}$; therefore, the effective charge is simply given by the ratio of the two mobilities when the field and force are equal. Here this gives $\tilde{Q}/Q \approx \mu_e(dh40)/\mu_m(1ed40) \approx 0.58$, or $\tilde{Q} = 23\,e$, where $\mu_m(1ed40) \approxeq 0.491\,\mu_o$. In simulations, we chose $\Delta V = 15.6,\ 31.2$ and $46.8\,\frac{k_B T}{e}$, which gives capture radii $\lambda_e \approx 435.1,\ 870.3$ and $1305.4\,\sigma$, respectively. Given the rod length $L = 20\,\sigma$, these values correspond to $R_\theta = 14.3,\ 18.0$ and $20.6\,\sigma$.

As shown in Fig. 8, the order parameters obtained at different field intensities collapse on a single curve after rescaling the distance to the pore by these estimates of R_θ. Interestingly, the curve is not the same for the capture by, and exit from, the pore, again showing the asymmetry between these two processes. Nevertheless, we see that the order parameter essentially vanishes for $r > R_\Theta$; we thus conclude that despite the presence of EHI, the orientational capture radius defined previously remains valid, including for the escape process (we did not study this in our previous paper).

V. CONCLUSION AND DISCUSSION

We have built computational raspberry-like rods with different charge distributions and simulated their electrophoretic and mechanical drift in free solution under various salt conditions to investigate how electrohydrodynamic interactions impact the electrophoretic velocity and orientation of short rod-like charged molecules. We also studied how these interactions and the details of the charge distribution affect the capture, translocation, and escape of these rods. For instance, we tested our previously defined orientation radius R_θ in the new

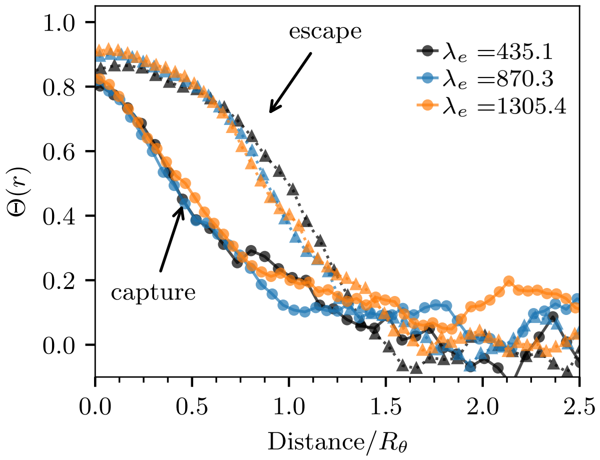

Figure 8. Order parameter $\Theta(r)$ *vs* scaled radial distance r/R_θ to the pore entrance/escape during the capture/escape processes for a double-helix rod ($Q = 40\,e$) with different field intensities λ_e. We have $R_\theta = 14.3,\ 18.0$ and $20.6\,\sigma$ for the cases shown here. Each curve is averaged over 50 translocation simulations using a salt concentration $C_s/C_s^o = 0.03$.

simulation setup, and studied the effect of the rod-wall interactions on rod capture. In order to be systematic, we present our main conclusions as a list of points below:

- The decrease of the free-solution electrophoretic mobility μ_e with salt concentration is a result of the competition between charge screening and rod orientation (Figs. 3a and c). Rods charged at one end only tend to orient with the field and have a higher mobility due to the lower frictional drag they encounter when oriented that way. For rods with other charge distributions, increasing the salt concentration also orients the rod with the field and thus increases μ_e. On the other hand, μ_e is reduced due to the charge screening at high salt concentration.

- The mechanical drift mobility μ_m is independent of the salt concentration (Fig. 3b) and is higher when the force is applied at the end of the rod. Rods with symmetric charge distributions move perpendicular to the force for the concentration range we have tested (Fig. 3c), which is consistent with what is reported in refs[27,28].

- The rod velocity and the applied field/force are not necessarily pointing in the same direction even in a uniform field due to hydrodynamic interactions (Fig. 4). The maximum deviation is $\approx 10°$ for $C_s/C_s^o = 0.03$ when the rod makes an angle of $\theta \approx \pi/3$ with the field.

- The rod's orientational order parameter is asymmetric during the capture and escape processes despite the field lines being identical on both sides of the wall. The charge distribution has more effect on rod orientation during the capture process when compared to the escape process.
- However, the charge distribution impacts capture, translocation, and escape times, as well as the way rods enter the nanopore (Table II). End-charged rods enter the nanopore via their charged end while there is no preference for other rods due to their symmetric charge distributions. The translocation time has a strong dependence on the charge distribution. For instance, sometimes the part of the rod that is inside the nanopore is uncharged, which severely slows down the translocation; for example, the translocation time is approximately 2.2 times larger for end-charged rods compared to double-helix rods (Table II).
- The capture time is correlated with the initial angular (polar) position and orientation of the rod when it starts close to the nanopore, in agreement with our previous investigations[12]. The mean capture time of a rod is shorter when it is launched near the wall because the rod then tends to align along the wall[13,30].
- The previously defined orientational capture radius R_Θ is still valid for both the capture and escape processes when EHI are present.

Overall, our simulations of the raspberry-like rod provide us with a more complete picture of the electrophoresis of rod-like molecules both in free solution and during translocation. We have demonstrated the important role that salt plays for rod orientation and charge screening, especially when the charge distribution is not uniform. Our results of rod orientation during capture qualitatively agree with our previous theories and LD simulations[12] as well as with theoretical calculations[13] that account for the anisotropic friction coefficient of rods and near-wall interactions. For applications such as the translocation of aptamer-bound molecules[1,31], our simulation results shine some light on the underlying physics under different conditions.

ACKNOWLEDGEMENT

GWS acknowledges the support of both the University of Ottawa and the Natural Sciences and Engineering Research Council of Canada (NSERC), funding reference number RGPIN/046434-2013. LQ is supported by the Chinese Scholarship Council and the University of Ottawa. The authors wish to thank Christian Holm and Kai Szuttor for fruitful discussions.

REFERENCES

[1]L. Reynaud, A. Bouchet-Spinelli, C. Raillon, and A. Buhot, "Sensing with Nanopores and Aptamers: A Way Forward," Sensors **20**, 4495 (2020).

[2]L. Xue, H. Yamazaki, R. Ren, M. Wanunu, A. P. Ivanov, and J. B. Edel, "Solid-state nanopore sensors," Nat. Rev. Mater. **5**, 931–951 (2020).

[3]C. Wen and S.-L. Zhang, "Fundamentals and potentials of solid-state nanopores: A review," J. Phys. D: Appl. Phys. **54**, 023001 (2021).

[4]D. Deamer, M. Akeson, and D. Branton, "Three decades of nanopore sequencing," Nat. Biotechnol. **34**, 518–524 (2016).

[5]M. J. U. Hasnain, "A review on nanopore sequencing technology, its applications and challenges Mirza Jawad Ul Hasnain," PAB **9** (2020), 10.19045/bspab.2020.90019.

[6]Y. Goto, R. Akahori, I. Yanagi, and K.-i. Takeda, "Solid-state nanopores towards single-molecule DNA sequencing," J Hum Genet **65**, 69–77 (2020).

[7]Z. Yuan, Y. Liu, M. Dai, X. Yi, and C. Wang, "Controlling DNA Translocation Through Solid-state Nanopores," Nanoscale Res Lett **15**, 80 (2020).

[8]V. V. Palyulin, T. Ala-Nissila, and R. Metzler, "Polymer translocation: The first two decades and the recent diversification," Soft Matter **10**, 9016–9037 (2014).

[9]S. Buyukdagli, J. Sarabadani, and T. Ala-Nissila, "Theoretical Modeling of Polymer Translocation: From the Electrohydrodynamics of Short Polymers to the Fluctuating Long Polymers," Polymers **11**, 118 (2019).

[10]L. Qiao, M. Ignacio, and G. W. Slater, "Voltage-driven translocation: Defining a capture radius," J. Chem. Phys. **151**, 244902 (2019).

[11]L. Qiao, M. Ignacio, and G. W. Slater, "An efficient kinetic Monte Carlo to study analyte capture by a nanopore: Transients, boundary conditions and time-dependent fields," Phys. Chem. Chem. Phys. **23**, 1489–1499 (2021).

[12]L. Qiao and G. W. Slater, "Capture of rod-like molecules by a nanopore: Defining an "orientational capture radius"," J. Chem. Phys. **152**, 144902 (2020).

[13]R. Waszkiewicz and M. Lisicki, "Hydrodynamic effects in the capture of rod-like molecules by a nanopore," J. Phys.: Condens. Matter **33**, 104005 (2021).

[14]A. V. Datar, M. Fyta, U. M. B. Marconi, and S. Melchionna, "Electrokinetic Lattice Boltzmann Solver Coupled to Molecular Dynamics: Application to Polymer Translocation," Langmuir **33**, 11635–11645 (2017).

[15]F. Weik, R. Weeber, K. Szuttor, K. Breitsprecher, J. de Graaf, M. Kuron, J. Landsgesell, H. Menke, D. Sean, and C. Holm, "ESPResSo 4.0 – an extensible software package for simulating soft matter systems," Eur. Phys. J. Spec. Top. **227**, 1789–1816 (2019).

[16]V. Ustach and R. Faller, "The Raspberry model for protein-like particles: Ellipsoids and confinement in cylindrical pores," The European Physical Journal Special Topics **225**, 1643–1662 (2016), arXiv:1604.01829.

[17]L. P. Fischer, T. Peter, C. Holm, and J. de Graaf, "The Raspberry Model for Hydrodynamic Interactions Revisited. I. Periodic Arrays of Spheres and Dumbbells," J. Chem. Phys. **143**, 084107 (2015), arXiv:1503.02671.

[18]J. de Graaf, T. Peter, L. P. Fischer, and C. Holm, "The Raspberry Model for Hydrodynamic Interactions Revisited. II. The Effect of Confinement," J. Chem. Phys. **143**, 084108 (2015), arXiv:1503.02681.

[19]T. Rau, F. Weik, and C. Holm, "A dsDNA model optimized for electrokinetic applications," Soft Matter **13**, 3918–3926 (2017).

[20]P. Ahlrichs and B. Dünweg, "Simulation of a single polymer chain in solution by combining lattice Boltzmann and molecular dynamics," J. Chem. Phys. **111**, 8225–8239 (1999).

[21]M. Deserno and C. Holm, "How to mesh up Ewald sums. II. An accurate error estimate for the particle–particle–particle-mesh algorithm," J. Chem. Phys. **109**, 7694–7701 (1998).

[22]M. Deserno and C. Holm, "How to mesh up Ewald sums. I. A theoretical and numerical comparison of various particle mesh routines," J. Chem. Phys. **109**, 7678–7693 (1998).

[23]G. S. Manning, "Limiting laws and counterion condensation in polyelectrolyte solutions. 7. Electrophoretic mobility and conductance," J. Phys. Chem. **85**, 1506–1515 (1981).

[24] G. S. Manning, "Limiting laws and counterion condensation in polyelectrolyte solutions. 8. Mixtures of counterions, species selectivity, and valence selectivity," J. Phys. Chem. **88**, 6654–6661 (1984).

[25] L. C. McCormick and G. W. Slater, "The molecular end effect and its critical impact on the behavior of charged-uncharged polymer conjugates during free-solution electrophoresis," Electrophoresis **26**, 1659–1667 (2005).

[26] M. V. Chubynsky and G. W. Slater, "Theory of end-labeled free-solution electrophoresis: Is the end effect important?" Electrophoresis **35**, 596–604 (2014).

[27] M. Shin, D. L. Koch, and G. Subramanian, "Structure and dynamics of dilute suspensions of finite-Reynolds-number settling fibers," Phys. Fluids **21**, 123304 (2009).

[28] A. Hamid, A. Arshad, S. Mehdi, M. Qasim, A. Ullah, J. Molina, and R. Yamamoto, "A numerical study of sedimentation of rod like particles using smooth profile method," International Journal of Multiphase Flow **127**, 103263 (2020).

[29] F. Farahpour, A. Maleknejad, F. Varnik, and M. R. Ejtehadi, "Chain deformation in translocation phenomena," Soft Matter **9**, 2750 (2013).

[30] J. T. Padding and W. J. Briels, "Translational and rotational friction on a colloidal rod near a wall," J. Chem. Phys. **132**, 054511 (2010).

[31] J. Y. Y. Sze, A. P. Ivanov, A. E. G. Cass, and J. B. Edel, "Single molecule multiplexed nanopore protein screening in human serum using aptamer modified DNA carriers," Nature Communications **8**, 1552 (2017).

8

Ratcheting charged polymers through symmetric nanopores using pulsed fields : designing a low pass filter for concentrating DNA

Manuscript under review.

Ratcheting charged polymers through symmetric nanopores using pulsed fields: Designing a low pass filter for concentrating DNA

Le Qiao, Gary W. Slater
Physics Department, University of Ottawa,
Ottawa, Ontario, Canada, K1N 6N5

(Dated: March 1, 2021)

Abstract

When nanopores are used to capture and translocate DNA molecules through a membrane, the resulting capture rate is essentially independent of molecular size, which makes the process incapable of changing relative concentrations in a mixture. Using Langevin Dynamics simulations, we show that it is possible to design pulsed fields to ratchet captured semiflexible molecules in such a way that only short chains successfully translocate, effectively transforming the nanopore process into a low pass molecular filter. The process itself can be run with many pores in parallel, thus increasing its potential usefulness.

I. INTRODUCTION

Polymer translocation is the process by which a polymeric chain is forced to move through a wall via a nanochannel [1–7]. Typically, an electric field is used to drive this process for charged molecules like DNA; the field is then used to both capture the molecules and force translocation. Several low-resolution devices have been built using this general idea [6, 7]. One feature of this process is the fact that while DNA translocation times are molecular size dependent [3], the capture rates are not (except for short chains) [8–13]; as a consequence, it cannot be used to change the concentration ratio (e.g., for purification purposes) of DNA mixtures.

In theory, we can favor translocation of the smallest molecule in a mixture by applying the translocating field (*i.e.*, once the molecule is captured) during a forward time $\tau_{\rightarrow}$ comparable to its mean DC translocation time $\overline{\tau}$, after which the field polarity would be reversed for a duration $\tau_{\leftarrow}$ long enough to disengage all molecules that have failed to translocate. Unfortunately, the distribution of translocation times is very broad [2]: if the molecules are close in size, these distributions will significantly overlap and $\tau_{\rightarrow}$ will have to be chosen very short ($\tau_{\rightarrow} \ll \overline{\tau}$) to inhibit the translocation of the longer chains – with an obvious unfavourable effect on translocation rates (as usual, the conditions for high purity and high numbers compete with each other).

Here we propose to use pulsed electric fields to selectively ratchet [14–18] captured molecules across a symmetric nanochannel. In principle, the fact that we have different molecular partial sizes and conformations on both sides of the wall during translocation can be used to drive a ratchet process even with a perfectly symmetric nanochannel. We show that asymmetric pulsed fields improve ratcheting. More precisely, we use the ratchet effect to move small molecules in one direction (translocation) while moving the larger ones in the opposite direction (retraction). We explore two versions (or protocols): one in which the ratchet effect starts upon capture, while the second one combines capture and translocation.

II. THEORY

Both computer simulation data and the tension propagation theory [19–22] show that the mean translocation time of a relaxed chain of N monomers under a constant driving force applied to the monomers inside the nanochannel scales like $\overline{\tau} \sim N^{\alpha}$, where α increases with N to reach the asymptotic value $\alpha = 1 + \nu$ ($\nu = 3/5$ is Flory's exponent). The capture time τ_c of a chain, however, is independent of N. Since $\tau_c \gg \overline{\tau}$, translocating a solution of DNA molecules using a DC field is not expected to change the relative abundance of the different molecular sizes. This is the problem we are proposing to address using ratcheting pulsed fields.

Two elements are required to build a ratchet that can rectify otherwise random motion: keeping the system out of equilibrium and symmetry breaking. The first condition can be achieved using either a stochastic or a deterministic external perturbation [23–25], such as a pulsed field. The symmetry can be spatially [25–29] and/or temporally broken [26, 30]. In this paper, some spatial asymmetry comes from the conformational and size differences between the polymer segments on each side of the wall, while temporal asymmetry comes from pulsed fields such as the Zero-Integrated-Field Electrophoresis (ZIFE) pulses shown in Fig. 1b and previously used in gel electrophoresis [31].

III. MODEL AND PARAMETERS

Our Langevin Dynamics simulations use coarse-grained bead-spring chains with the bead-bead and bead-wall excluded volume interactions modeled using the purely repulsive Weeks-Chandler-Andersen (WCA) potential [32]

$$U_{\mathrm{WCA}}(r) = \begin{cases} 4\epsilon\left[\left(\frac{\sigma}{r}\right)^{12} - \left(\frac{\sigma}{r}\right)^{6}\right] + \epsilon & \text{for } r < r_c \\ 0 & \text{for } r \geq r_c. \end{cases} \tag{1}$$

The nominal bead size σ is used as the unit of length and the well depth $\epsilon = k_B T$ as the unit of energy, while the cutoff length $r_c = 2^{1/6}\,\sigma$ makes U_{WCA} purely repulsive. The Finitely-Extensible-Nonlinear-Elastic (FENE) potential $U_{\mathrm{FENE}}(r) = -\frac{1}{2}K_{\mathrm{FENE}}\ r_0^2\ \ln\left(1 - {r^2}/{r_0^2}\right)$ is used to connect adjacent monomers [33]; the maximum extension is $r_0 = 1.5\,\sigma$ and the spring constant is $K_{\mathrm{FENE}} = 30\,\epsilon/\sigma^2$. The combined energy $U_{WCA} + U_{FENE}$ gives a mean bond length of $\langle b \rangle \approx 0.96\ \sigma$. We control the polymer stiffness via the angular harmonic potential $U_{\mathrm{Bend}}(\phi) = \frac{1}{2}K_{\mathrm{Bend}}\,(\phi - \pi)^2$, where ϕ is the angle between two consecutive bonds and $K_{\mathrm{Bend}} = 10\,\epsilon$; the resulting free solution polymer persistence length is $L_p \approx 5\,\sigma$.

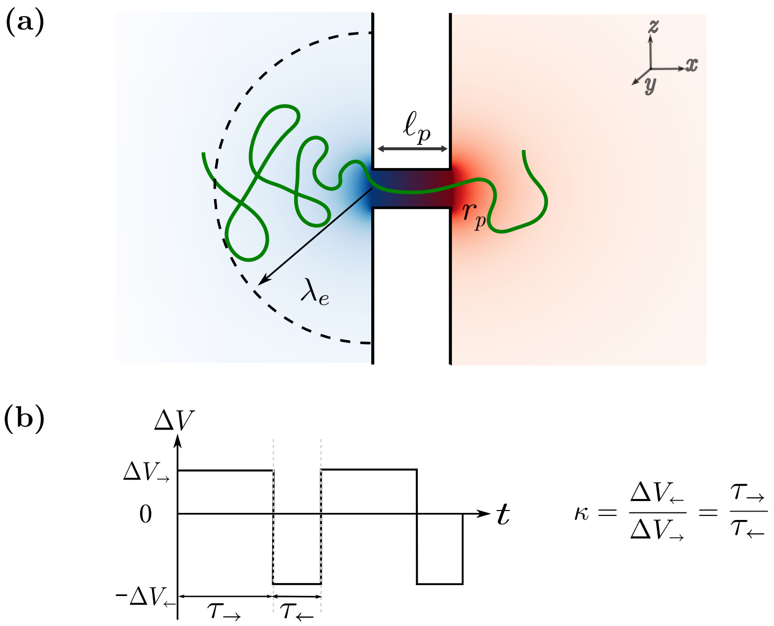

FIG. 1. (a) A schematic view of polymer translocation through a nanopore; the background codes for the strength of the electric field (more opacity meaning higher fields). The nanochannel is of radius r_p and length ℓ_p. The dashed line depicts the nominal capture radius (λ_e) separating the diffusion dominated and drift dominated regions. (b) A schematic of the pulse sequence: the pulses are asymmetric when $\kappa \neq 1$.

The electric potential outside the pore is given by [34]

$$V(\zeta, \eta, \phi) = \Delta V \; \tfrac{r_e}{r_p} \; \arctan\left[\sinh(\zeta)\right], \tag{2}$$

where ΔV is the total potential difference across the device, $r_e = r_p/(\frac{2\ell_p}{r_p} + \pi)$ is the characteristic length of the electrostatic potential outside a nanochannel of radius r_p and length ℓ_p, while $\zeta \in (-\infty, +\infty)$, $\eta \in [0, \pi]$ and $\phi \in [0, 2\pi]$ are the oblate spherical coordinates. The potential drop across the channel is $\delta V = \Delta V \times 2\ell_p r_e/r_p^2$, corresponding to a electric field $E_p = \delta V/\ell_p = \Delta V \times 2r_e/r_p^2$. We use $r_p = 1.5\,\sigma$ (which ensures single file dynamics) and $\ell_p = 5\,\sigma$; the potential drop between an electrode ($r \to \infty$) and the pore is then $\approx \frac{1}{6}\,\Delta V$ while the drop inside the channel is $\delta V \approx \frac{2}{3}\,\Delta V$. The nominal capture radius for a chain of N monomers (each with a charge Q), $\lambda_e = N\Delta V Q r_e/k_B T$, will be used as a field intensity.

The LD equation of motion for a monomer is

$$m\dot{\vec{v}} = \vec{\nabla}U(\vec{r}) - \xi\vec{v} + \sqrt{2\xi k_{\mathrm{B}}T}\ \vec{R}(t), \tag{3}$$

where $\vec{\nabla}U(\vec{r}) = \vec{\nabla}(U_{\mathrm{WCA}} + U_{\mathrm{FENE}} + U_{\mathrm{Bend}} + U_{\mathrm{E}})$ is the sum of the conservative forces, $U_{\mathrm{E}}(\vec{r})$ is the electric potential, m and ξ are the mass and friction coefficient of a monomer, and $-\xi\vec{v}$ is the damping force due to the fluid. The last term on the *rhs* is the uncorrelated noise that models random kicks from the solvent. The random variable $\vec{R}(t)$ satisfies $\langle R_i(t)\rangle = 0$ and $\langle R_i(0)R_j(t)\rangle = \delta(t)\delta_{ij}$, where $\delta(t)$ is the Dirac delta function and $i, j \in [x, y, z]$. The unit of time $\tau_o = \sigma^2\xi/k_BT$ is chosen to be the time needed for a monomer to diffuse over its own size σ. In our simulations the integration time step is $\Delta t = 0.01\,\tau_o$. The systems are in a box with a minimum size of $1.5\,\lambda_e$ (as measured from the nanopore) and periodic boundary conditions are applied.

Although we use dimensionless variables, it is useful to look at potential examples. Since dsDNA has a persistence length $L_p \approx 50\,nm$, our parameters then correspond to $\sigma = 10\,nm$, $r_p = 15\,nm$ and $\ell_p = 50\,nm$. For ssDNA, these numbers would be $L_p \approx 2\,nm$, giving $\sigma = 0.4\,nm$, $r_p = 0.6\,nm$ and $\ell_p = 2\,nm$.

IV. POLYMER CAPTURE

Before proposing two different pulsed field protocols to ratchet semiflexible chains, we must first examine polymer capture since this does impact translocation dynamics. We start each capture simulation by placing the center of mass of a polymer with a random equilibrium conformation (radius of gyration R_{go}) at a radial distance $r_o = \lambda_e \approx 5 - 10\,R_{go}$ right above the nanopore; the capture is completed when one end monomer has reached the channel's mid-point.

During capture, the electric forces drive molecules to the nanopore, and their conformations deform and orient in response to both the converging field lines and the presence of the wall. This can be visualized by following the mean square radius of gyration R_g^2 as the "doomed" chain end approaches the pore – Fig. 2a. We note that R_g^2 doubles when the end monomer moves from $\approx 8\,R_{go}$ to $\approx 5\,R_{go}$. However, the conformation then compresses as the chain gets closer to the nanopore. Since the end monomer needs time to find the pore entrance (hence the cloud of data points around $[r = 2R_{go}, R_g = R_{go}]$), the rest of the chain catches up, further compression takes place, and eventually we even get $R_g < R_{go}$. Our results are consistent with those of [35].

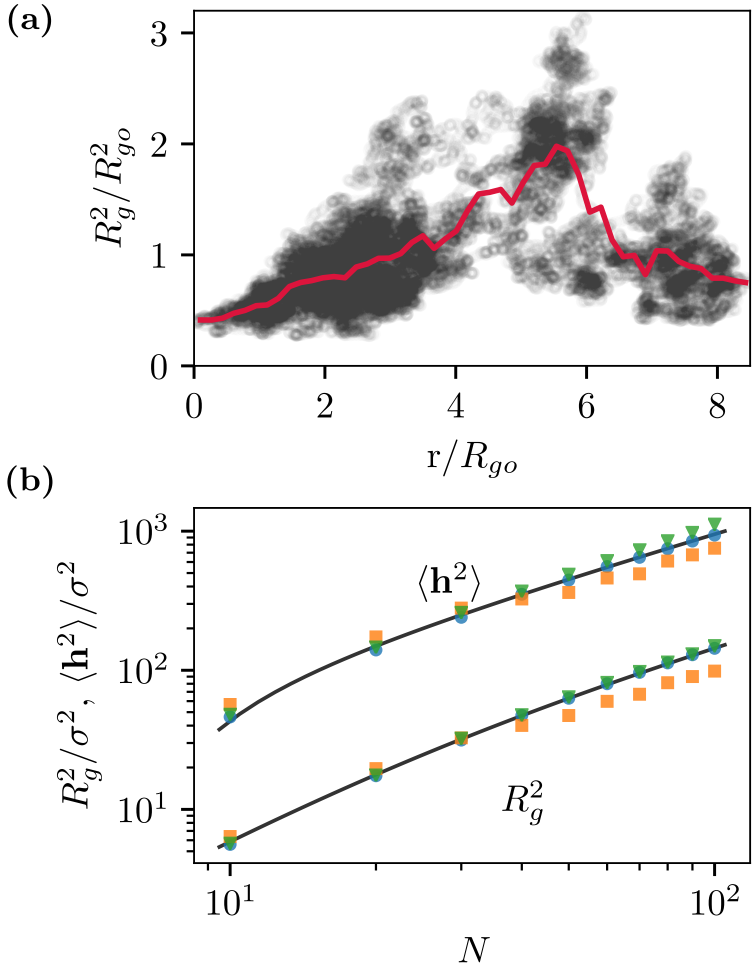

FIG. 2. (a) Mean square radius of gyration R_g^2 *vs* distance r between the pore entrance and the end-monomer that will be captured. Both axes are rescaled by the polymer's equilibirum radius of gyration $R_{go} = 8.9\,\sigma$. The grey cycles give periodically sampled simulation data obtained for the capture of a single $N = 60$ chain with a field intensity $\lambda_e = 67.5\,\sigma$; the solid line is the binned average. (b) R_g^2 and mean squared end-to-end distance $\langle \mathbf{h^2} \rangle$ *vs* chain length N (ensemble size $\Omega = 1000$). The field intensity is $\lambda_e(N) = \frac{N}{60} \times 67.5\,\sigma$. Data shown for polymers in free solution (●), after being captured by the pore (■) and grafted on the wall (▼). The solid lines are the theoretical predictions of the Kratky-Porod equation [36] for free semi-flexible chains.

The semi-flexible nature of the chain impacts this process. Figure 2b shows the N-dependence of both R_g^2 and the mean square end-to-end distance $\langle \mathbf{h^2} \rangle$ of free chains and of polymers immediately after capture. Since simulation studies often start chains in a relaxed state with ≥ 1 monomers already engaged in the channel, we have also added data corresponding to the relaxed state of a chain grafted on the wall. Up to $N \approx 40$, both captured and grafted chains are slightly more extended than free chains; since these molecules are close to the rod-like limit, they orient [37] during capture which helps the end monomer find the pore. But beyond that point, the data sets diverge, with captured chains being more compact (in agreement with Fig. 2a) and grafted chains being slightly more extended. Theory [21, 22] indicates that initial conformations affect translocation times; indeed, for the range of chain lengths and field intensities used here, we obtain $\overline{\tau} = (1.10 \pm 0.03) \times N^{1.21\pm0.01}$ when we start with captured conformations, but $\overline{\tau} = (0.95 \pm 0.08) \times N^{1.28\pm0.02}$ for relaxed chains (data not shown). The field outside the pore also plays a role since we find $\overline{\tau} = (0.89 \pm 0.10) \times N^{1.31\pm0.02}$ when relaxed conformations are driven with the force applied only in the nanopore, a standard set-up in simulations.

V. SEPARATING DNAS USING A FEEDBACK MECHANISM

Our first protocol sorts polymers by size from a binary mixture using a feedback mechanism. In short, it employs a DC field to capture polymers (as described above) and a current detector to determine when a chain end has entered (or left) the nanopore. When a capture is detected, the DC field is replaced by the pulsed field to selectively translocate the shortest chains.

Figure 3a shows the probability of translocation P_N as a function of the pulse duration $\tau_{\rightarrow}$ when a symmetric pulsed field ($\kappa = 1$) is used. The vertical lines indicate the mean DC translocation times $\overline{\tau} \sim N^{1.21}$. Not surprisingly, we observe sigmoidal curves with midpoints located roughly at $\tau_{\rightarrow} \approx \overline{\tau}(N)$ and widths directly related to that of the distribution function of DC translocation times. Some trajectories are shown in Fig. 3c for $\tau_{\rightarrow} = 50\,\tau_o$: the short $N = 50$ chains translocate before the first polarity reversal while the $N = 70$ chains oscillate back and forth for a few cycles ($\approx 50\%$ of them ultimately succeed). The $N = 100$ chains do not translocate: they simply retract after a few cycles.

An ideal separation device would have both a high differential efficiency $\Delta P(N_1, N_2) =$

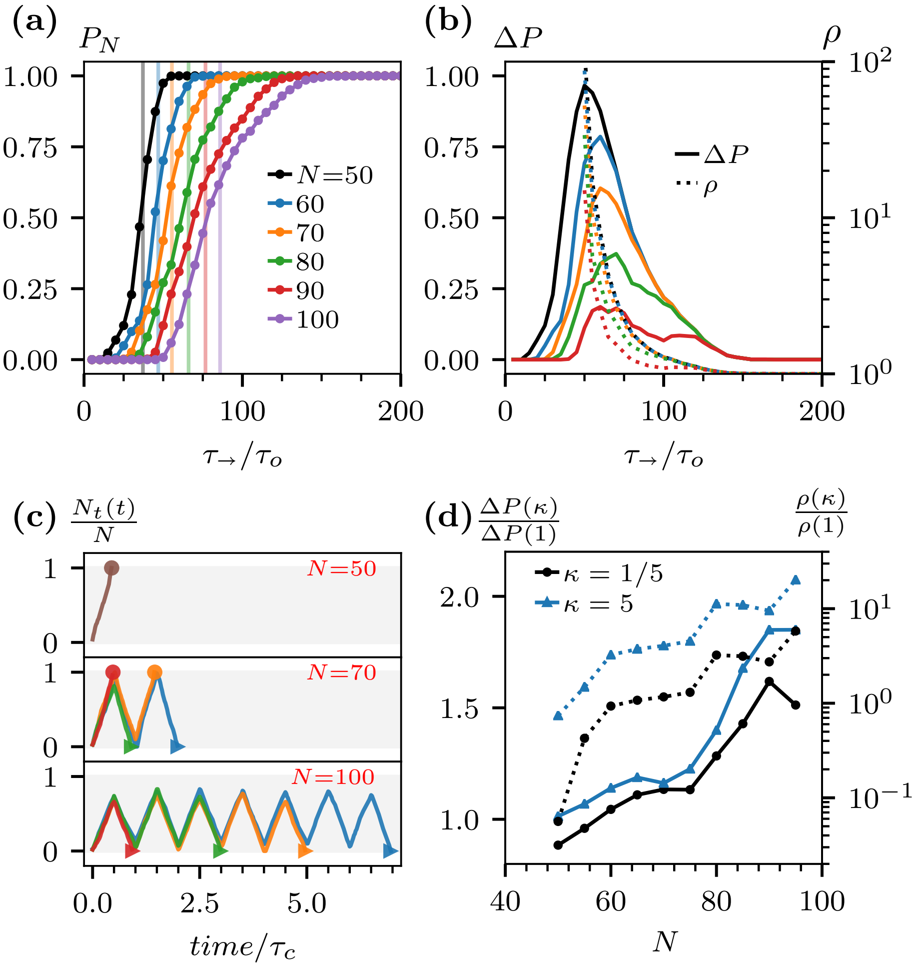

FIG. 3. Pulsed field data for captured polymers of size $N = 50 - 100$ (ensemble size $\Omega = 1000$). (a) Translocation probability P_N *vs* forward pulse duration $\tau_\rightarrow$ for unbiased pulses ($\kappa = 1$) with a field intensity $\lambda_e(N) = \frac{N}{50} \times 168.9\,\sigma$. The vertical lines give the mean DC translocation times. (b): Same data plotted to show the differential probability $\Delta P(N, 100)$ (solid lines; left y-axis) and the probability ratio $\rho(N, 100)$ (dotted lines; right y-axis). (c) Fractional number of monomers $N_t(t)/N$ that have passed the mid-point of the channel *vs* time for three chain lengths. The unbiased pulse duration $\tau_c = 2\tau_\rightarrow = 100\,\tau_o$ is used to rescale the time axis. The filled circles show the end of a successful translocation while the triangles mark full retraction. (d) Ratios $\Delta P(N, 100, \kappa)/\Delta P(N, 100, 1)$ (left y-axis) and $\rho(N, 100, \kappa)/\rho(N, 100, 1)$ (right y-axis) *vs* polymer size N for $\kappa = 5$ and $\kappa = 1/5$. The low and high field intensities are $\lambda_e(N) = \frac{N}{50} \times 56.3\,\sigma$ and $\lambda_e(N) = \frac{N}{50} \times 281.5\,\sigma$, respectively.

$P_{N_1} - P_{N_2}$ and an excellent purity ratio $\rho(N_1, N_2) = P_{N_1}/P_{N_2}$. Figure 3b shows how $\Delta P(N, 100)$ and $\rho(N, 100)$ vary as a function of the pulse duration $\tau_{\rightarrow}$ for a field intensity $\lambda_e(N) = \frac{N}{50} \times 168.9\,\sigma$ and $\kappa = 1$. As expected, both parameters increase with the molecular size difference, with $\Delta P(N, 100)$ increasing from 0.2 (for $N = 90$) to 0.95 (for $N = 50$), while the corresponding ratio $\rho(N, 100)$ increases from 3 to 80. The ratio ρ diverges at short pulse durations because the $N = 100$ chains then fail to translocate; however, ΔP then rapidly decays. The best overall performance is thus located near the maximum of $\Delta P(N, 100)$. The performance is rather poor when $(N_1 - N_2) \ll N_2$, as expected.

Since conformational asymmetry alone does not produce a strong ratchet effect, we now explore the impact of adding a pulse asymmetry $\kappa \neq 1$. We explore two different cases: $\kappa < 1$ (the translocation is driven by the higher field intensity) and $\kappa > 1$ (the low field drives the translocation). For a fixed asymmetry κ, both $\Delta P(N, 100)$ and $\rho(N, 100)$ are enhanced compared to the $\kappa = 1$ case – see Fig. 3d, with the $\kappa > 1$ ZIFE pulses providing better results. In fact, the ratio $\rho(95, 100)$ is increased by a remarkable factor of ≈ 20 compared to symmetric pulses.

VI. NANOPORES IN PARALLEL

However, the feedback approach presented above does not make it possible to use multiple nanopores in parallel (the feedback loop is necessary because unbiased ZIFE pulses cannot capture polymers). To avoid this issue, we now bias the pulses by increasing the forward time from $\tau_{\rightarrow}$ to $\tau_f = \tau_{\rightarrow} + \tau_{\Rightarrow}$. The dimensionless mean field intensity $\Phi(\tau_{\Rightarrow}, \kappa, \tau_{\rightarrow}) = \frac{\langle \Delta V \rangle}{\Delta V_{\rightarrow}} = \frac{\tau_{\Rightarrow}}{\tau_{\Rightarrow} + \tau_{\rightarrow}(1 + 1/\kappa)}$ will be used as a measure of the bias.

The field-driven deterministic time to move from position r_o to $r < r_o$ under the action of the electric is $\tau_E(r_o, r) = \int_{r_o}^{r} v_d^{-1}(r')\mathrm{d}r' = (r_o^3 - r^3)/3\lambda_e D$ [12], with a similar expression for reverse pulses. The position after M complete cycles is then $r(r_o, M) = \sqrt[3]{r_o^3 - 3M\lambda_e D\tau_{\Rightarrow}}$ (note that unbiased $\tau_{\Rightarrow} = 0$ pulses lead to $r = r_o$ or no net motion towards the pore). The largest value of M ($\in \mathbb{N}_0$) for which the argument of the cubic-root is positive gives the number M_o of complete pulse cycles needed to capture a polymer initially located at $r = r_o$. The capture process proper thus starts with a forward pulse of reduced duration $\tau_f^o = \tau_f - \tau_E(r(r_o, M_o), 0) = \tau_{\rightarrow} + \tau_{\Rightarrow} - r(r_o, M_o)^3/3\lambda_e D$. We tested that $\tau_f^o \in [0, \tau_f]$ is essentially a random number when we vary r_o, even though this is a deterministic result for a particle (data not shown). Since both Brownian motion and the time required by the polymer ends to find the nanopore add randomness, we test the biased ratchet process by averaging over a flat distribution of initial pulse times τ_f^o.

Figure 4a shows the probabilities P_{100}, P_{50} and $\Delta P = P_{50} - P_{100}$ as a function of the mean field intensity Φ for pulse biases $\tau_{\Rightarrow} = 30\,\tau_o$ and $15\,\tau_o$ (both values are smaller than the chains' mean DC translocation times $\overline{\tau}_{50} = 111.6\,\tau_o$ and $\overline{\tau}_{100} = 257\,\tau_o$). Since we saw in Fig. 3d that $\kappa = 5$ provides an excellent separation ratio, here we fix κ and use $\tau_{\rightarrow}$ to tune the mean field $\Phi(\tau_{\Rightarrow}, 5, \tau_{\rightarrow})$. In the short pulse regime $(\tau_{\rightarrow} + \tau_{\leftarrow}) = (1 + 1/\kappa)\tau_{\rightarrow} \ll \tau_{\Rightarrow}$, the AC component is negligible and we basically have a DC field of intensity $\Phi = 1$: both molecules then easily translocate ($P_N \to 1$). In the opposite long pulse limit $\tau_{\rightarrow} > \overline{\tau}_N > \tau_{\Rightarrow}$, a chain of size N translocates immediately during the first part of the first cycle and we again have $P_N \to 1$ although Φ is now small. Note that since this is happening at a molecular size dependent critical value of the pulse duration $\tau_{\rightarrow}(N)$, there is a range where separation is possible, as shown. As expected, the maximum value of $\Delta P = P_{50} - P_{100}$ increases when the bias is reduced (from $\tau_{\Rightarrow} = 30\tau_o$ to $15\tau_o$ here) because we are moving towards the conditions present in Fig. 3d. In other words, the bias reduces ΔP because it increases the probability of translocation for both molecular sizes.

However, the bias allows the pulses to also capture the polymer chains here: Fig. 4b shows two capture-and-translocation trajectories with $\Phi(30, 5, 150) = 0.14$. The $N = 100$ and 50 chains start from $r_o = 50\,\sigma$ right above the nanopore with a reflecting wall at $z = 100\,\sigma$. Similar to the DC capture case, both chains spend a large amount of time trying to find the entrance of the nanopore. The $N = 50$ chain translocates within 2 cycles after capture while the $N = 100$ chain quickly retracts. In short, a bias added to the ratcheting pulses allows us to both capture and translocate molecules, but the size specificity is reduced. On the other hand, the absence of a feedback loop means that one can run hundreds or thousands of pores in parallel (or/and in series), a major advantage in some cases. Optimization of parameters for specific applications is beyond the scope of this letter.

VII. CONCLUSIONS

The combination of molecular size-independent capture rates and broad distributions of translocation times greatly limits the use of nanopore translocation as a process that

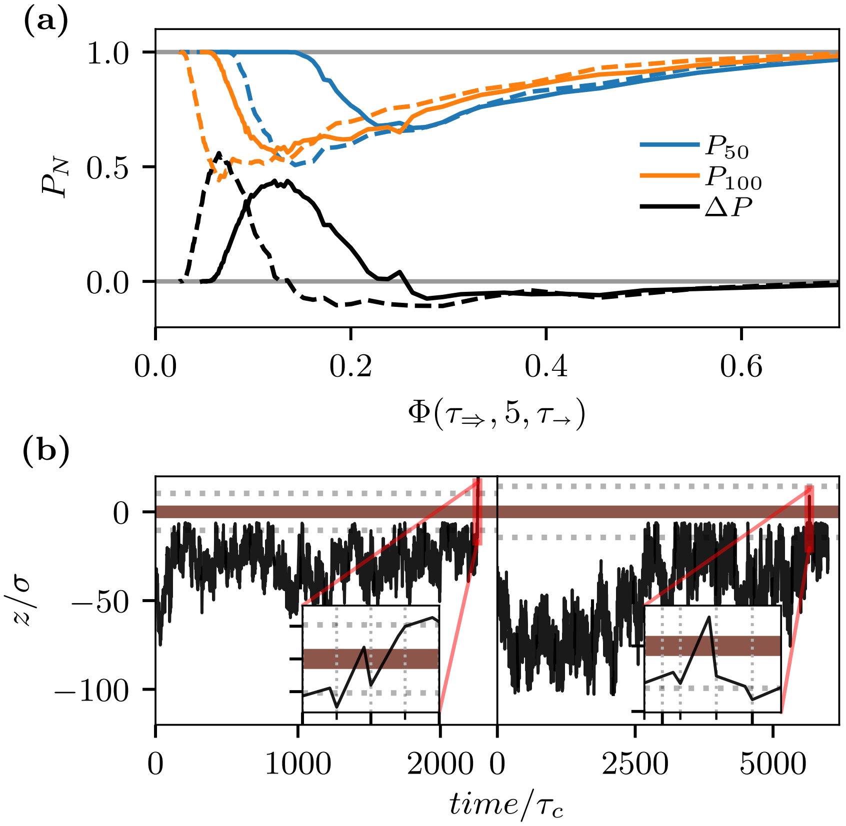

FIG. 4. (a) Translocation probability P_N *vs* dimensionless mean field intensity $\Phi(\tau_{\Rightarrow}, \kappa = 5, \tau_{\rightarrow})$. The time biases are $\tau_{\Rightarrow} = 15$ (dashed lines) and $30\,\tau_o$ (solid lines); the mean field is changed by varying $\tau_{\rightarrow}$ between 25 and $500\,\tau_o$. (b) Trajectory of the end monomer of chains of size $N = 50$ (left panel) and 100 (right panel). The bias is $\tau_{\Rightarrow} = 30\tau_o$ and the total cycle duration is $\tau_c = \tau_{\rightarrow} + \tau_{\Rightarrow} + \tau_{\leftarrow} = 210\,\tau_o$, which gives a mean field intensity $\Phi(30, 5, 150) = \frac{1}{7}$. The y-axis gives the monomer's vertical distance to the wall center. The gray dashed lines mark the distance R_{go} from the wall surface, with of $R_{go} = 7.9$ and $12\,\sigma$ for $N = 50$ and 100, respectively

can modify the concentration ratio of DNA solutions. We have previously an experimental approach for small (point-like) particles that have different diffusion coefficients but the same electrophoretic mobility: this scheme made use of *on/off* pulsed-fields [13] to modify their capture rates.

In this Letter, we have introduced the basic features of a low pass molecular filter device for molecules such as dsDNA. The key idea is to use pulsed electric fields to ratchet captured polymer chains through the nanochannel, and to design the pulses to favour the translocation of small molecules. We tested two such theoretical ideas using Langevin Dynamics simulations that include realistic field lines. Note that we also simulated the capture process since translocation dynamics do depend on the initial polymer conformations; long semiflexible polymers were shown to orient due to the converging field lines while drifting towards pore, but to also compress while the end monomers are trying to find the pore entrance. The next logical modeling step would be to add hydrodynamic interactions; previous simulation studies suggested that HI have small effects on molecular conformations at capture [34] and on translocation times [38].

We first proposed using unbiased ZIFE pulses with a feedback mechanism (necessary since ZIFE pulses cannot capture polymers). Although symmetric pulses can preferentially ratchet small captured molecules through the pore, we showed that asymmetric pulses can significantly enhance the device efficiency. Our results demonstrate that temporal asymmetry is sufficient to drive the ratchet process with a symmetric nanopore: asymmetric channels such as periodic cone/sawtooth-shaped channels[17, 29] or spatial asymmetric external potentials (*e.g.* sawtooth-shaped potentials[14, 15, 23, 25]) are not needed. In essence, the pulsed field dynamically reduces the impact of the overlapping distribution functions of DC translocation times.

However, the presence of the feedback loop is likely to be a major issue in practice for several reasons. We thus proposed to add a small bias to the ZIFE pulses to build a device that can both capture and translocate short polymer molecules. Since this process does not need a feedback loop, it can be used with a large number of pores in parallel (with a substantial gain in quantities) or in series (with gains in selectivity). In these cases, the mean-field has to be tuned properly to achieve sufficient capture rates while maintaining a useful ratchet effect (the addition of the bias increases the probability that long chains may translocate).

Time varying fields have been proposed previously, but essentially with the goal of increasing sequencing performance and accuracy (see, for example, Refs. [39] and [40]). Our goals here are fundamentally different since we are proposing approaches to change concentration ratios in mixed DNA solutions.

Most polymer ratchet devices that have been proposed use asymmetric channels. What makes our approach unique is that we use a symmetric nanopore system and take advantage of the dynamical asymmetries that exist during translocation (different polymer lengths and conformations across the wall). As we have shown, asymmetric pulses can improve the resulting effects. However, it is also possible that the pore geometry and walls could be designed to further increase the effects reported here. For example, Mondal et al. [41] have shown that pore-polymer interactions and conformational entropy can lead to Stochastic Resonance effects during the translocation of flexible polymer chains under an oscillatory driving force. Adding such effects would greatly increase the size of the parameter space and may lead to new ways to manipulate DNA molecules in fluidic systems.

ACKNOWLEDGMENTS

Simulations were performed using the ESPResSo package [42] on the computer clusters provided by WestGrid (https://www.westgrid.ca) and Compute Canada (https://www.computecanada.ca). GWS acknowledges the support of both the University of Ottawa and the Natural Sciences and Engineering Research Council of Canada (NSERC), funding reference number RGPIN/046434-2013. LQ is supported by the Chinese Scholarship Council (CSC) and the University of Ottawa.

[1] A. Meller, L. Nivon, and D. Branton, Phys. Rev. Lett. **86**, 3435 (2001).

[2] M. Wanunu, Phys. Life Rev. **9**, 125 (2012).

[3] V. V. Palyulin, T. Ala-Nissila, and R. Metzler, Soft Matter **10**, 9016 (2014).

[4] W. Shi, A. K. Friedman, and L. A. Baker, Anal. Chem. **89**, 157 (2017).

[5] S. Buyukdagli, J. Sarabadani, and T. Ala-Nissila, Polymers **11**, 118 (2019).

[6] L. Xue, H. Yamazaki, R. Ren, M. Wanunu, A. P. Ivanov, and J. B. Edel, Nat. Rev. Mater. **5**, 931 (2020).

[7] C. Wen and S.-L. Zhang, J. Phys. D: Appl. Phys. **54**, 023001 (2021).

[8] M. Muthukumar, J. Chem. Phys. **132**, 195101 (2010).

[9] P. Rowghanian and A. Y. Grosberg, Phys. Rev. E **87**, 042722 (2013).

[10] A. Y. Grosberg and Y. Rabin, J. Chem. Phys. **133**, 165102 (2010).

[11] S. K. Nomidis, J. Hooyberghs, G. Maglia, and E. Carlon, J. Phys.: Condens. Matter **30**,

304001 (2018).

[12] L. Qiao, M. Ignacio, and G. W. Slater, J. Chem. Phys. **151**, 244902 (2019).

[13] L. Qiao, M. Ignacio, and G. W. Slater, Phys. Chem. Chem. Phys. **23**, 1489 (2021).

[14] D. R. Chialvo and M. M. Millonas, Phys. Lett. A **209**, 26 (1995).

[15] J. S. Bader, R. W. Hammond, S. A. Henck, M. W. Deem, G. A. McDermott, J. M. Bustillo, J. W. Simpson, G. T. Mulhern, and J. M. Rothberg, Proc. Natl. Acad. Sci. U.S.A **96**, 13165 (1999).

[16] Z. Wang, Z. Jia, and X. He, Soft Matter **9**, 11107 (2013).

[17] D. Mondal and M. Muthukumar, J. Chem. Phys. **145**, 084906 (2016).

[18] S. Park, J. Song, and J. S. Kim, Sci. Adv. **5**, eaav4943 (2019).

[19] T. Sakaue, Phys. Rev. E **76**, 021803 (2007).

[20] T. Sakaue, Phys. Rev. E **81**, 041808 (2010).

[21] J. Sarabadani, T. Ikonen, H. Mökkönen, T. Ala-Nissila, S. Carson, and M. Wanunu, Sci. Rep. **7**, 7423 (2017).

[22] T. Ikonen, A. Bhattacharya, T. Ala-Nissila, and W. Sung, Phys. Rev. E **85** (2012).

[23] M. O. Magnasco, Phys. Rev. Lett. **71**, 1477 (1993).

[24] Y. V. Gulyaev, A. S. Bugaev, V. M. Rozenbaum, and L. I. Trakhtenberg, Phys.-Usp. **63**, 311 (2020).

[25] M. Kenward and G. W. Slater, Phys. Rev. E **78** (2008).

[26] G. W. Slater, H. L. Guo, and G. I. Nixon, Phys. Rev. Lett. **78**, 1170 (1997).

[27] R. W. Hammond, J. S. Bader, S. A. Henck, M. W. Deem, G. A. McDermott, J. M. Bustillo, and J. M. Rothberg, Electrophoresis **21**, 74 (2000).

[28] P. Malgaretti, I. Pagonabarraga, and J. M. Rubi, J. Chem. Phys. **138**, 194906 (2013).

[29] M. Heidari, M. Mikani, and N. Nikoofard, J. Nanostructure Chem. **10**, 131 (2020).

[30] F. Tessier and G. W. Slater, Appl. Phys. A **75**, 285 (2002).

[31] E. Brassard, C. Turmel, and J. Noolandi, Electrophoresis **13**, 529 (1992).

[32] J. D. Weeks, D. Chandler, and H. C. Andersen, J. Chem. Phys. **54**, 5237 (1971).

[33] G. S. Grest and K. Kremer, Phys. Rev. A **33**, 3628 (1986).

[34] F. Farahpour, A. Maleknejad, F. Varnik, and M. R. Ejtehadi, Soft Matter **9**, 2750 (2013).

[35] S. C. Vollmer and H. W. de Haan, J. Chem. Phys. **145**, 154902 (2016).

[36] I. Teraoka, en*Polymer Solutions: An Introduction to Physical Properties* (Wiley, New York,

2010).

[37] L. Qiao and G. W. Slater, J. Chem. Phys. **152**, 144902 (2020).

[38] M. G. Gauthier and G. W. Slater, Eur. Phys. J. E **25**, 17 (2008).

[39] G. M. Cherf, K. R. Lieberman, H. Rashid, C. E. Lam, K. Karplus, and M. Akeson, Nat. Biotechnol. **30**, 344 (2012).

[40] M. T. Noakes, H. Brinkerhoff, A. H. Laszlo, I. M. Derrington, K. W. Langford, J. W. Mount, J. L. Bowman, K. S. Baker, K. M. Doering, B. I. Tickman, and J. H. Gundlach, Nat. Biotechnol. **37**, 651 (2019).

[41] D. Mondal and M. Muthukumar, J. Chem. Phys. **144**, 144901 (2016).

[42] F. Weik, R. Weeber, K. Szuttor, K. Breitsprecher, J. de Graaf, M. Kuron, J. Landsgesell, H. Menke, D. Sean, and C. Holm, Eur. Phys. J. Spec. Top. **227**, 1789 (2019).

9

Conclusion

We investigated the voltage-driven capture and translocation of charged analytes through a nanopore using computer simulations and theoretical calculations. Our research started logically with the capture of point-like particles before moving to rod-like molecules and long flexible polymers. Our aim was to achieve a better understanding of the mechanisms at play during the capture process, clarifying the existing theories, and exploring new possibilities for the various nanopore translocation techniques.

Our work began with the concept of the *capture radius*, which is the length scale that is frequently used in the literature to estimate the capture rate for translocation experiments. Several theories have been proposed in the past to define the capture radius. However, some of the approximations are rather crude and sometimes contradict each other. In particular, the nanopore size doesn't appear in those calculations. We revisited and revised some of the existing approaches by taking into account the pore size using theoretical analysis and Lattice Monte Carlo (LMC) simulations. Our theory demonstrated that the capture radius is not always a steady-state quantity. Instead, it grows slowly as $\sim t^{1/3}$. Our simulation results, on the other hand, suggested a growth $\sim t^{1/2}$ for the long-time diffusion-limited regime. The crossover between the two regimes is larger than the capture radius predicted by existing theories. Our simulations also predicted a steady-state capture rate except for a very short transient time, which is consistent with experimental results.

The term *depletion zone* is often associated or mixed with the concept of the *capture radius*. To the best of my knowledge, it was only experimentally reported once by looking at snapshot pictures of fluorescent DNA translocation [31]. We looked at the capture of point-like particles using Kinetic Monte Carlo (KMC) simulations. Our simulation results using the point-charge field (PCF) approximation suggested the steady-state depletion zone near the nanopore is barely larger than the pore radius and narrows at higher field intensities. Those results are consistent with the steady-state solution of the drift-diffusion equation. Furthermore, when we replace the PCF with the exact field lines near the pore, there is a concentration peak built up near the nanopore due to the flat field, and the peak grows and is displaced toward the nanopore at higher field intensities.

Polymer capture is a non-equilibrium process due to molecular orientation and deformation, two phenomena sometimes missed in previous theories. We studied orientational effects on rod capture, both with and without electrohydrodynamic interactions (EHI). We showed that the orientation of the rod during the capture can be characterized by an orientational capture radius $R_\theta = \sqrt[3]{\lambda_e L^2/60}$, which depends on the field intensity outside the nanopore (λ_e) and the length of the rod (L). Under normal experimental conditions, one expects the orientational radius to be smaller than the capture radius. This indicates the rods are captured well before they orient ; as a result, the orientation only impacts the last step of the capture process, *i.e.*, finding the entrance of the nanopore. Furthermore, the orientation of the rod is not at its local equilibrium because the center of mass drifting is faster than rotational dynamics ; for instance, when a rod starts below R_θ, its capture time depends on its initial orientation.

The capture of a non-uniformly charged rod is a nontrivial process because of the EHI, charge screening, and orientation. In free solution, we compared rod electrophoresis with drift under a mechanical force. We showed that the mobility and orientation not only depend on the charge distribution but also on the type of force. For example, uniformly charged rods tend to orient with the field lines even though the field is uniform. In contrast, when a mechanical force is applied uniformly along the rod, the latter tends to orient perpendicular to the force. Our translocation simulations indicate that the orientational order parameter is asymmetric during the capture and post translocation processes, despite the field lines being identical on both sides of the wall. In fact, the charge distribution impacts the orientation more significantly during the capture. Moreover, the capture/translocation/escape times depend on the charge distribution for many coexisting reasons. By performing capture simulations for a uniformly charged rod, we showed that the orientational capture radius R_θ defined previously under a quasi-static approximation is still valid when EHI are included in LD simulations. Lastly, the near-wall steric and hydrodynamic interactions accelerate the capture process.

For the capture of the flexible polymers, the electric field drives molecules toward the nanopore and their conformations deform in response to the converging field lines and the presence of the wall. Our LD simulation results indicate that the polymer conformation elongates first before they arrive at the pore entrance ; then one end of the polymer chain needs to unravel to find the pore, during which the polymer chain is compressed by the field lines and wall constraints. These more compact conformations result in a faster translocation in comparison to the results from conventional simulations where we start the translocation with one end already inside the nanopore.

Nanopore translocation has been primarily used for sensing purposes in the past. In this thesis, we showed that it should be possible to use a nanopore and pulsed electric fields to design novel separation devices. We first proposed a separation scheme for small particles that have the same mobility but different diffusion coefficients. The idea is to make use of *on/off* pulsed-fields to modify the ratio of the capture rates. For long flexible polymers, the capture rate is size-independent and the translocation time distribution is very broad. Therefore it is challenging to modify the concentration ratio of DNA solutions using nanopore translocation. We demonstrated how one could use pulsed fields and a nanopore to ratchet polymers by size such that only short chains successfully translocate. We proposed and tested two schemes using LD simulations, with or without feedback mechanisms ; both could effectively modify the concentration ratio of polymer solutions.

Outlook

As summarized above, we focused on understanding the capture process by combining computer simulations and theoretical analysis. Analyte capture by a nanopore is still a complex process due to the conformational orientation and deformation. EHI, on the other hand, push the complexity to another level. This is especially true for molecules with anisotropic architectures or asymmetric charge distributions. On a different note, our work on nanopore ratchet opens up many new possibilities. Below I propose some potential future extensions of my work :

- We studied rod orientation and polymer deformation separately. However, the conformation of long polymers is cigar-like in free solution. One would expect the coexistence of the two effects during the early stages of the capture process. How do they contribute to capture ?

- The translocation of small molecule-bound aptamers has been a hot topic in the past decade. However, theories for the dynamic of those molecules are still not complete. We introduced the GPU-based LD-LB simulations for charged rods with different charge distributions, the first step in this direction. Besides moving forward with adding EHI to the simulation of long polymers, we can also focus on understanding the electrophoresis of small molecules with anisotropic architectures.

- The combination of the pulsed field and nanopore translocation could also be used for many purposes :
  - ☐ **Speculation I :** Can we design a pulsed-field system to help end monomers find the nanopore ?
  - ☐ **Speculation II :** Can we tune the pulsed fields to create stochastic resonance with polymer conformational relaxation to narrow the translocation time distribution ?
  - ☐ **Speculation II :** Can we envision a ratchet device with a dual nanopore and pulsed fields to trap/retract long polymers while translocating short chains.

In conclusion, the work described in this thesis is just the first milestone along the long road to understanding and controlling the capture process. Our simulation models can be further refined or adapted to suit different research purposes not limited to polymer translocation. We are hoping that this thesis may provide a framework and spark new ideas for future investigations.

APPENDIX

A

An empirical method to characterize and parametrize anomalous yet Brownian diffusion

Manuscript to be submitted.
The sections that include the work done by Nicholas Ilow,
the second co-author, are presented in greyscale.

An empirical method to characterize and parametrize anomalous yet Brownian diffusion

Le Qiao, Nicholas Ilow, Maxime Ignacio, Gary W. Slater
Department of Physics, University of Ottawa,
Ottawa, Ontario K1N 6N5, Canada.

(Dated: May 31, 2021)

Abstract

We propose an empirical fitting function to characterize non-Gaussian displacement distribution functions (DispD) often observed for heterogeneous diffusion problems. We first this fitting function with a typical anomalous yet Brownian problem of a colloidal particle diffusing between two walls using Langevin Dynamics (LD) simulations of a raspberry particle coupled to a lattice Boltzmann (LB) fluid. We also test the function with a simple model of anomalous diffusion on a square lattice with obstacles. In both cases, the fitting parameters provide more information than just the Kurtosis (which is often the method used in such cases), including the length scale at which the tails of the DispD begin. In all cases, the fitting parameters smoothly converge towards the Gaussian values when the systems become less anomalous.

I. INTRODUCTION

Diffusion in inhomogeneous media is ubiquitous in Nature and can be observed in a wide range of systems including surface diffusion of atoms in an elastic field[1–3]; diffusion of colloidal particles in a confined fluid[4–8] or polymer network[9]; polymer translocation through a nanopore membrane[10–12]; protein diffusion in crowded cell environments[13–16]. Experimental observations have shown that some of these systems can lead to non-trivial dynamical properties which require special attention.

For instance, some systems give rise to anomalous diffusion where the mean-square displacement (MSD) increases like t^γ, with $\gamma < 1$. This is often related to diffusion in disordered systems, in which case there is a crossover distance beyond which diffusion becomes normal ($\gamma = 1$). Another particularly interesting case is the possible existence of *anomalous yet Brownian* diffusion which is characterized by a linear MSD ($\gamma = 1$) coexisting with a non-Gaussian Displacement Distribution (DispD)[17–19]. The physical origin of anomalous yet Brownian diffusion remains a very active field of research, in particular because it may differ between systems. A common feature though is the fact that the diffusion coefficient varies during the process.

In both classes of problems, the nature of the DispD is central to our understanding of the physics. The Kurtosis $K(t) = \mu_4(t)/\mu_2(t)^2$ of the DispD is often used to characteristic the deviations from Gaussian (normal diffusion) dynamics[4,9,20] (μ_i is the i^{th} central moment of the distribution). However, the DispD obviously contains more information than what the Kurtosis provides, including the shape of the tails and the length scale(s) that separate the various dynamical regimes.

In this article, we propose a new empirical function that can be used to fit a DispD that has different regimes for short and large distances. In particular, this function can capture both the Gaussian and the non-Gaussian components of a DispD. This flexible interpolating function allow us to locate the transition between the two components as the external control parameters are changed. To test our fitting function, we simulate two different systems corresponding to the two classes of problems mentioned above. First, we use a lattice Boltzmann method coupled Langevin Dynamics (LB-LD) to simulate the diffusion of a particle in a liquid between two flat walls, an example of anomalous yet Brownian motion[17,21]. We then study diffusion on a lattice with obstructed sites, a case where short-time diffusion is known to be anomalous.

II. A PRACTICAL FITTING FUNCTION

To fit both the central and tail parts of "anomalous" distributions, we propose to use the 3-parameter function

$$P(x,t)\mathrm{d}x = \frac{1-A}{\sqrt{\pi x_o^2}}\ \exp\left[1-\left[1+\left(\tfrac{x}{x_o}\right)^{2-\alpha}\right]^{1-\beta}\right]\mathrm{d}x, \tag{1}$$

where x is the position and t is the time. The three fitting parameters are the length scale x_o and the two exponents, which we expect to be in the ranges $0 \leq \alpha < 2$ and $\beta < 1$ (note that A is simply the normalization factor). A single-exponent DispD corresponds to $\beta = 0$, including the Gaussian distribution for $\alpha = 0$ (in which case we also have $A = 0$), the exponential function for $\alpha = 1$, and the Weibull (or stretched exponential) distribution for $1 < \alpha < 2$. The combination $[\beta = \frac{1}{2}, \alpha = 0]$ is a Gaussian with exponential tails, while $1 - \beta = \frac{2}{2-\alpha}$ is a distribution with Gaussian tails (a special case being $[\beta = -1, \alpha = 1]$, an exponential distribution with Gaussian tails).

As long as $\beta \neq 0$, we have two regimes, namely

$$P(x,t) \sim \begin{cases} \exp\left[-(1-\beta)\left(x/x_o\right)^{2-\alpha}\right] & \text{for } x \ll x_o \\ \exp\left[-\left(x/x_o\right)^{(2-\alpha)(1-\beta)}\right] & \text{for } x \gg x_o. \end{cases} \tag{2}$$

The arguments of the two exponentials are equal for a critical value $x^{*2} = x_o^2/(1-\beta)^{2/\beta(2-\alpha)}$. The mean-square displacement (MSD) is given by

$$\langle x^2(t,\alpha,\beta)\rangle = x_o^2(t) \times \frac{G(2,\alpha,\beta)}{G(0,\alpha,\beta)} \tag{3}$$

where $G(i,\alpha,\beta) = \int_0^\infty y^i \exp\left[1-\left[1+y^{2-\alpha}\right]^{1-\beta}\right]\mathrm{d}y$. The only explicit time-dependence of the MSD is in $x_o(t)$, with $x_o^2(t) = \langle x^2(t)\rangle = 4Dt$ for normal diffusion; however, the exponents α and β can also vary with time. The corresponding Kurtosis is given by

$$K(\alpha,\beta) = \frac{\langle x^4(\alpha,\beta)\rangle}{\langle x^2(\alpha,\beta)\rangle^2} = \frac{G(4,\alpha,\beta)\ G(0,\alpha,\beta)}{G^2(2,\alpha,\beta)}\ . \tag{4}$$

Although $G(i,\alpha,\beta)$ has no closed form, the following second-order approximations are useful for a nearly Gaussian DispD (*i.e.*, when $\alpha \ll 1$ and $|\beta| \ll 1$):

$$A \approx \frac{\alpha}{109.6} + \frac{\beta}{1.354} + \frac{\alpha^2}{29.65} + \frac{\beta^2}{4.126} + \frac{\alpha\beta}{2.537} \tag{5}$$

$$\frac{x^{*2}}{x_o^2} \approx e^1 \times \left[1 + \frac{\alpha+\beta}{2} + \frac{9\alpha^2 + 11\beta^2 + 12\alpha\beta}{24}\right] \tag{6}$$

$$\frac{\langle x^2 \rangle}{\frac{1}{2}x_o^2} \approx 1 + \frac{\alpha}{1.930} + \frac{\beta}{0.5509} + \frac{\alpha^2}{1.992} + \frac{\beta^2}{0.3204} + \frac{\alpha\beta}{0.4895} \tag{7}$$

$$\frac{\langle x^2 \rangle}{\frac{1}{2e}x^{*2}} \approx 1 + \frac{\alpha}{55.14} + \frac{\beta}{0.7603} + \frac{\alpha^2}{8.479} + \frac{\beta^2}{0.4987} + \frac{\alpha\beta}{1.141} \tag{8}$$

$$K - 3 \approx \alpha + \frac{\beta}{0.9695} + \frac{\alpha^2}{1.426} + \frac{\beta^2}{0.6297} + \frac{\alpha\beta}{0.8653} \; . \tag{9}$$

These equations can be useful when examining the relative roles of the exponents α and β.

III. EXAMPLE I: WALL-HINDERED DIFFUSION

Our first example is a simulation of the wall-hindered diffusion of a spherical particle of radius R between two walls separated by a distance h. In bulk solution, the particle's diffusion coefficient is given by $D_0 = k_B T / 6\pi\eta R$, with η the viscosity of the fluid. Hydrodynamic interactions (HI) make the diffusion coefficient space-dependent and anisotropic near surfaces. For a particle at a distance z (see Fig. 1b) from a single flat wall[22], the diffusivities parallel and perpendicular to the wall are

$$D_{\parallel}(z)/D_0 \approx 1 - \tfrac{9}{16}\Gamma + \tfrac{1}{8}\Gamma^3 - \tfrac{45}{256}\Gamma^4 - \tfrac{1}{16}\Gamma^5 + ... \tag{10}$$

$$D_{\perp}(z)/D_0 \approx (6 - 10\Gamma + 4\Gamma^2)/(6 - 3\Gamma - \Gamma^2), \tag{11}$$

with $\Gamma = \frac{R}{R+z}$. As recently shown by Matse *et al.*[23], the z-dependence of $D_{\perp}$ leads to anomalous yet Brownian motion (linear time-dependence of the MSD but non-Gaussian DispD).

A. Raspberry colloidal particle diffusion

We use Langevin Dynamics as implemented in the ESPResSo package[24]. The HI are included by coupling the particle's velocity to a lattice Boltzmann fluid. Here we employ the raspberry particle model[25,26] shown in Fig 1a. The particle comprises $N = 454$ beads of size σ, for a total radius of $R = 3\,\sigma$ and a volume $V_o = \frac{4}{3}\pi R^3 \approx 113\,\sigma^3$. We freeze all beads relative to that at the center of mass using virtual rigid bonds which transfer momentum. The particle and the solvent share the same density, $\rho_s = m_o/\sigma^3$.

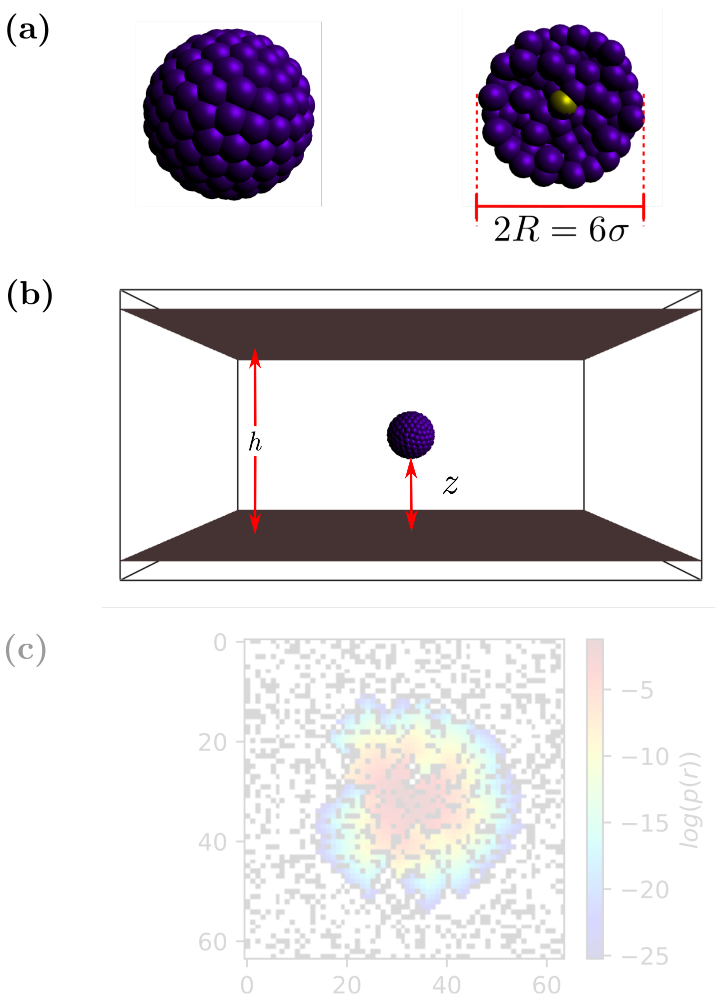

FIG. 1. The raspberry colloidal particle in the simulation system. (a) A raspberry particle of radius $R = 3\,\sigma$ comprising 336 coupling beads. The golden bead is the center of mass bead. (b) Two repulsive boundaries are separated by a distance h, while z is the distance between the particle surface and the wall. (c) A two dimensional square lattice (64x64) with $\phi = 30\%$ of the lattice sites occupied by obstacles (in black). A concentration profile is evolved to $t = 30/8$, where $\tau = \frac{1}{8}$, and the resulting profile is plotted overtop the obstacle configuration.

The implicit solvent is modeled by a GPU implementation of the three-dimensional 19 velocity LB method (D3Q19). The velocity $\boldsymbol{v}$ of a bead is coupled to the fluid via a drag force $\boldsymbol{f}_\gamma = -\gamma(\boldsymbol{v} - \boldsymbol{u}_i)$, where $\boldsymbol{u}_i$ is the velocity of the fluid at lattice grid where the bead resides, and γ is the coupling friction, which has to be to tuned to insure that hydrodynamic radius $R_H = R$.

The repulsive Weeks-Chandler-Andersen (W) potential[27] $U_{\mathrm{W}}(r) = 4\epsilon \left[\left(\frac{\sigma}{r}\right)^{12} - \left(\frac{\sigma}{r}\right)^{6} \right] + \epsilon$ models the steric interactions between the raspberry beads and the wall when $r < r_c = 2^{1/6}\,\sigma$, while $U_W(r > r_c) = 0$. We use ϵ for our unit of energy, σ for length and $\tau_o = \sigma\sqrt{m_o/\epsilon}$ for time. The temperature is chosen to be $k_BT = \epsilon$ while the kinematic viscosity of the fluid is $\eta = 12\,\sigma^2/t_o$ and the coupling per bead is $\gamma = 15\,m_o/t_o$. These choices give a mean hydrodynamic radius $R_H \approx 2.98\,\sigma$ and a diffusion coefficient $D_o = 0.00148\,\sigma^2/t_o$ in free solution. We use an integration time step $\delta t = 0.005\,t_o$.

B. Displacements distributions between two plates

The DispD$_\perp$ is computed for different time intervals and locations between two non-slip walls (Fig. 1b) separated by a distance $h = 30\,\sigma$. We start the particle in the center (*i.e.*, at $z = z_o = 7\,\sigma$) and let it diffuse freely until it reaches $z = \sigma/2$. The simulation times are long enough to generate 2000 uncorrelated sub-trajectories for different initial positions $z < z_o$.

When a particle diffuses away from a given initial position for a brief period of time, its diffusivity is essentially constant during the trajectory: our results (Appendix A) then show that it undergoes normal diffusion (MSD $\sim t$) but with a local diffusivity $D(z)$, in agreement with eqs. 10-11. However, when the DispD$_\perp$ is averaged over a high $\nabla D_\perp(z)$ region (the diffusion diffusivity regime[28]), it includes both Gaussian and non-Gaussian components. Figure 2a shows an example for the region $\frac{z}{R} \in [0.5, 2]$: the dashed Gaussian lines clearly demonstrate the presence of fat tails, in agreement with ref.[23], while the solid lines show that eq. 1 provides an excellent fit for all values of Δx and all times ($\alpha = 0$ here since the short distance behavior is Gaussian). Nevertheless, the MSD is still increasing linearly with time, as shown in Fig. 2b. Note that the DispD remains Gaussian in the parallel direction (not shown) because the diffusivity gradient is weak.

A common way to characterize such an "anomalous DispD" is to compute its Kurtosis. Figure 2c shows that the excess Kurtosis (both of the fitted function, $K - 3$, and of the raw data, $K_d - 3$) vanishes at short times (we then probe local regions with uniform diffusivity). We note that $K > K_d$ because the tails of the distributions are heavily truncated here (at a distance comparable to the length scale x_o).

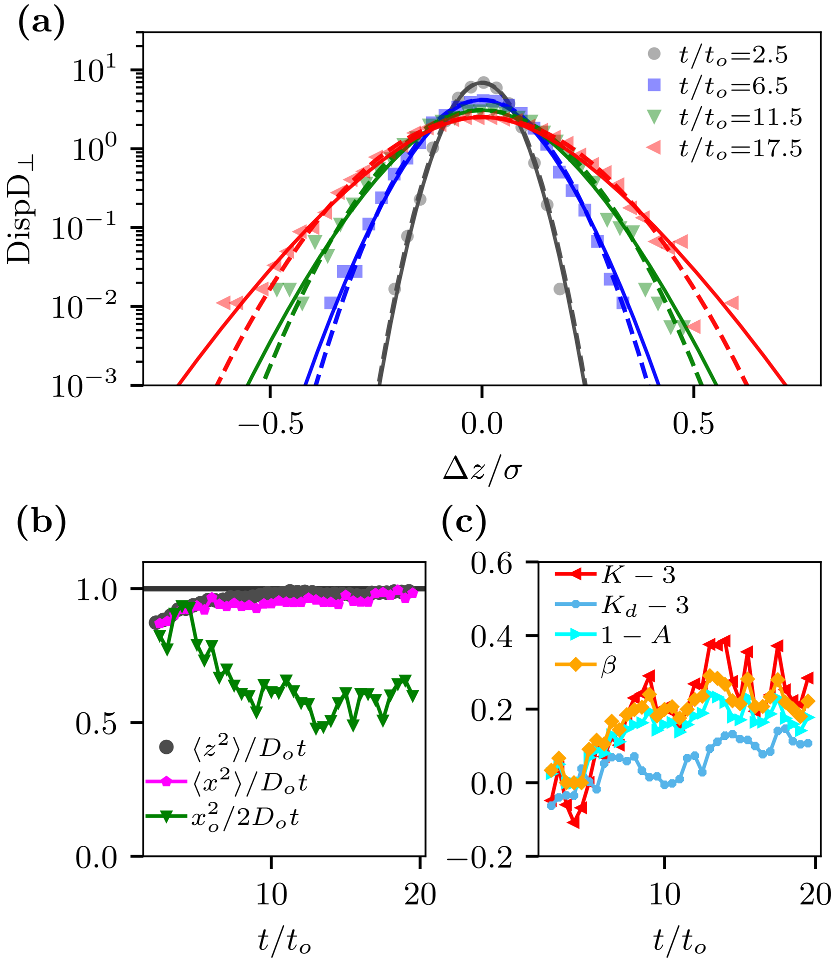

FIG. 2. (a) DispD$_\perp$ averaged over different starting positions $z/R \in [0.5, 2]$ at four different times. The simulation data points are binned with a bin size $0.03\,\sigma$. The dashed lines are Gaussian fits while the solid lines show the interpolating function $P(x, t, x_o, \alpha = 0, \beta)$. (b) Length scales divided by $D_o t$ as a function of time: $\langle z^2\rangle$ is the perpendicular MSD calculated from the raw data, while the other two are obtained from the fits. (c) The excess Kurtosis $K-3$, the normalization prefactor $1-A$ and the exponent β (as obtained from the fits) as a function of time; note that $K_d - 3$ is calculated directly from the raw data.

Our fitting function includes additional information. For instance, we see that the exponent β mirrors the behavior of the Kurtosis. In fact, we note that $K - 3 \approx \beta$ when β is small in Fig. 2c, in agreement with eq. 9. Similarly, the length scale x_o decays with time.

As suggested by eqs. 6 to 9, these parameters vary as the exponent β increases with time. The fit thus provide detailed information about the shape of the DispD as well as the length scale beyond which the Gaussian part (short distances) changes to fat tails (large distances). The fits indicate that the MSD increases linearly with time because the decrease in the ratio x_o^2/t is perfectly compensated by an increase in the tail anomalous exponent β.

Finally, we note that for a Gaussian distribution with perfect exponential tails, our interpolating function predicts $K(0, \frac{1}{2}) \approx 4.857$, which appears to agree with the limiting value reported in ref[23].

IV. EXAMPLE II: ANOMALOUS DIFFUSION IN RANDOM SYSTEMS

We now examine the usefulness of eq. 1 for a case of obstructed diffusion. We use the simplest model: a random walk on a two-dimensional square lattice with a fraction ϕ of the sites being randomly occupied by immobile obstacles (see Fig. 1c). In short, diffusion is expected to be normal (*i.e.*, the MSD grows linearly with time) for short times (before the particle starts colliding with the obstacles; this regime only exists at low obstacle concentration) and long times (the steady-state, achieved for times larger than the crossover time t^* and distances larger than the system's crossover length r^*). For intermediate times, the MSD grows roughly as t^γ, where the anomalous exponent $\gamma < 1$. See refs.[29–31] for detailed studies of this system. Obviously, given the transients mentioned above, we expect non-Gaussian distribution functions unless $t \gg t^*$.

A. Radom-Walk on a 2D Lattice

By randomly placing a concentration ϕ of 1×1 obstacles on a 1600×1600 square lattice, and averaging over an ensemble of 500 different obstacle configurations we can retrieve distribution functions for varying systems. This calculation uses a standard Markov Chain Monte Carlo propagation algorithm: we initially place a unit concentration on the lattice site at the center of the system, and we propagate the concentration throughout the system using the master equation. Jumping probabilities $p_x = p_y = p = \frac{1}{8}$ are chosen, leaving a probability of not jumping of $p_0 = \frac{1}{2}$. The Diffusion Coefficient throughout the lattice is set to $D = 1$, and the lattice spacing is set to $a = 1$. Calculating the time interval over a Markov

Step is then simply $\tau = \frac{a^2 p}{D} = \frac{1}{8}$. The resulting distribution functions (a few examples are shown in Fig. 3), at specific times, are then fitted with both a Gaussian and eq. 1.

B. Displacement distributions *vs* time

Our fitting function does not do a very good job at short time in Fig. 3 because of the coarse lattice discretization effects for short displacements (although it is slightly better than a Gaussian fit). Once we approach the crossover time t^* the tails are perfectly captured by our fit while the Gaussian fits are clearly inadequate. In fact, the Gaussian fits slowly converges with the data only when $t \gg t^*$, as expected.

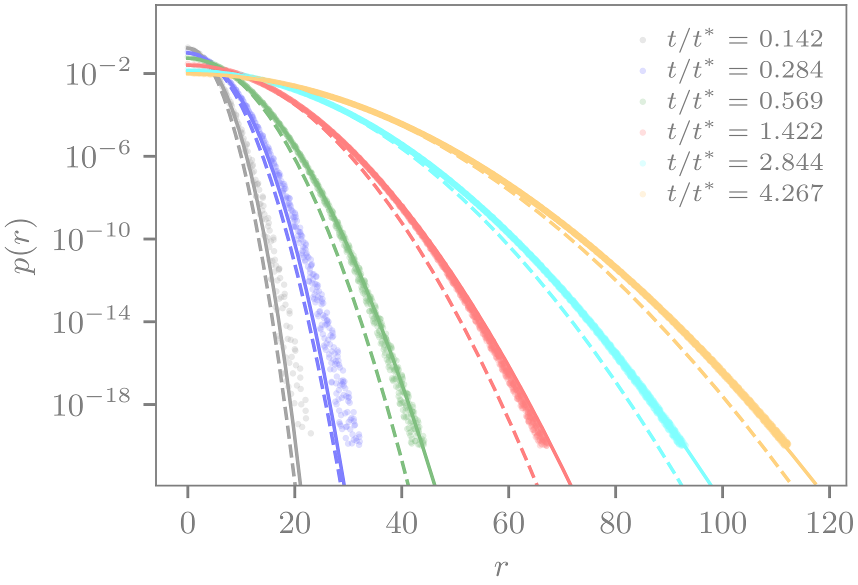

FIG. 3. Probability of being a distance r away from the center of a square lattice averaged over 500 random obstacle configurations at an obstacle concentration of $\phi = \frac{1}{9}$. The solid lines are the fits from eq. 1 and the dashed lines are Gaussian fits. Note that $r^* = 8.12$, $t^* = 21.9$ and $\gamma = 0.961$ for this system.

We examine how the fitting parameters in eq. 1 evolve as a function of time t in Fig. 4. We expect the distribution to become more Gaussian (or $(1-\beta)(2-\alpha) \to 2$) as we increase the time, and fully Gaussian distributions (*i.e.*, $\alpha = \beta = 0$) for times $t \gg t^*$.

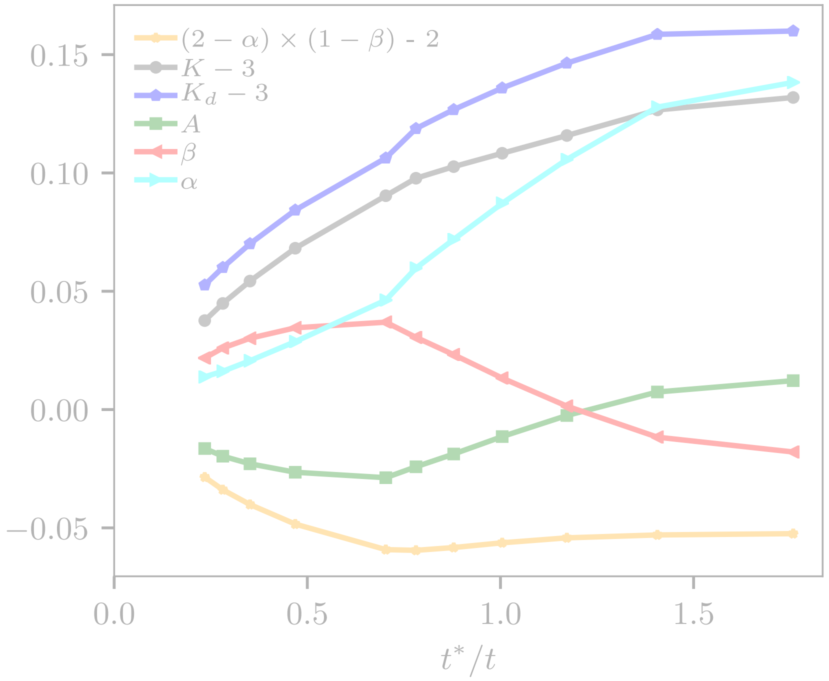

FIG. 4. The normalized concentration, $p(r)$, of all lattice sites a distance r away from the initial lattice site populated with a unit concentration is presented at varying times. We compute the Excess Kurtosis $K-3$, the exponents α and β, and the normalization factor A, from the interpolating fit of the data. Meanwhile K_d-3 is calculated directly from the distribution. All curves approach 0, i.e. their Gaussian limits, as $t \rightarrow \inf$.

However, the distribution function is not expected to be Gaussian over distances $r < r^*$ since diffusion is anomalous over these length scales (*i.e.*, we then have $\langle r^2(t)\rangle \sim t^\gamma$, with $\gamma < 1$). Indeed, all of the fitting parameters, as well as the Kurtosis, converge towards their Gaussian limits when $t \gg t^*$ in Fig. 4. This is in agreement with Fig. 3 where it is clear that the fits are more Gaussian as t/t^* increases. In Fig. 4 we also see a transition in the behaviour of the fitting parameters α, β and A, namely a change in the sign of the slope at $t^*/t \approx 0.75$. This is consistent with a transition from the anomalous regime to the steady state regime occurring at $t \approx t^*$.[29] Interestingly, the exponent β changes sign roughly at t^*, which also makes parameter A change sign (see eq.—5). Moreover, we notice that the product $(2-\alpha)(1-\beta)-2 \approx -0.05$ is roughly constant for $t < t^*$, implying that the tail of the distribution is $\sim \exp[-(x/x_o)^{1.95}]$ over this entire time period.

Again, our interpolating fit is giving us a lot of information about the distribution function, and in particular information about the changes that occur around the crossover time t^*.

V. CONCLUSION

In this article, we propose a new interpolating function that can conveniently characterize the displacement distribution that contains both Gaussian and non Gaussian exponential components. The key advantage of our function is that it can describe distributions that have core and tail components with different behaviours, and yet it includes only one additional fitting parameter (compared to the Gaussian fit).

We tested our interpolating function using two simple examples. In the first test, the physics of the problem is such that the distribution has to be Gaussian at short distances, but may have non-Gaussian tails. In the second test, the distribution is more general and the fits provided detailed information about its time evolution. We are currently studying how the fit parameters (especially the length scale x_o and tail exponent $(2-\alpha)(1-\beta)$) are connected to fundamental elements of the physics of these two problems such as the local diffusivity gradient (in the case of the first example) and the anomalous exponent γ (the second example).

Appendix A: Diffusion coefficient at different heights

Figure 5 shows the diffusion coefficients $D_\perp$ and $D_\parallel$ measured at different distances z from the wall. Our data are in a good agreement with theory (eqs. 10 and 11), thus validating our simulation approach.

The inset shows that we indeed obtain a Gaussian DispD$_\perp$ for $t = 12.5\,t_o$, with a variance $\sim D_\perp t_o$, for different initial positions z/R.

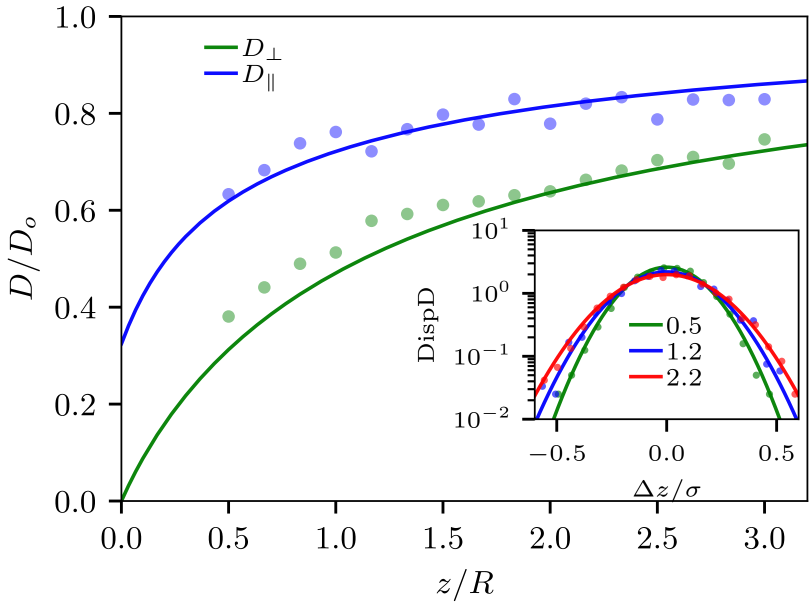

FIG. 5. Reduced diffusion coefficients parallel ($D_\parallel/D_o$) and perpendicular ($D_\perp/D_o$) to the wall *vs* the vertical distance z/R from the closest wall, where D_o is the free solution diffusion coefficient. The data points are obtained by fitting the time dependence of the MSD between $t = 0$ and $t = 20\, t_o$ for different initial positions z/R. The solid lines are from eqs. 10 and 11. Inset: Gaussian fit of the vertical DispD$_\perp$ for three different initial positions z/R=0.5, 1.2 and 2.2

.

---

[1] R. F. Sabiryanov, M. I. Larsson, K. J. Cho, W. D. Nix, and B. M. Clemens, Phys. Rev. B **67**, 125412 (2003).

[2] X. Xu, J.-N. Aqua, and T. Frisch, J. Phys. Condens. Matter **24**, 045002 (2012).

[3] M. Ignacio, Y. Saito, P. Smereka, and O. Pierre-Louis, Phys. Rev. Lett. **112**, 146102 (2014).

[4] C. Mejía-Monasterio, S. Nechaev, G. Oshanin, and O. Vasilyev, New J. Phys. **22**, 033024 (2020).

[5] P. Sharma, S. Ghosh, and S. Bhattacharya, Appl. Phys. Lett. **97**, 104101 (2010).

[6] A. Banerjee and K. D. Kihm, Phys. Rev. E **72**, 042101 (2005).

[7] M. A. Bevan and D. C. Prieve, J. Chem. Phys. **113**, 1228 (2000).

[8] E. R. Dufresne, T. M. Squires, M. P. Brenner, and D. G. Grier, Phys. Rev. Lett. **85**, 3317 (2000).

[9] R. K. Singh, J. Mahato, A. Chowdhury, A. Sain, and A. Nandi, J. Chem. Phys. **152**, 024903 (2020).

[10] J. L. A. Dubbeldam, A. Milchev, V. G. Rostiashvili, and T. A. Vilgis, EPL **79**, 18002 (2007).

[11] R. Metzler and J. Klafter, Biophys. J. **85**, 2776 (2003).

[12] Y. Kantor and M. Kardar, Phys. Rev. E **76**, 061121 (2007).

[13] A. Sabri, X. Xu, D. Krapf, and M. Weiss, Phys. Rev. Lett. **125**, 058101 (2020).

[14] G. Guigas and M. Weiss, Biophys. J. **94**, 90 (2008).

[15] H. Sanabria, Y. Kubota, and M. N. Waxham, Biophys. J. **92**, 313 (2007).

[16] D. S. Banks and C. Fradin, Biophys. J. **89**, 2960 (2005).

[17] B. Wang, S. M. Anthony, S. C. Bae, and S. Granick, PNAS **106**, 15160 (2009).

[18] B. Wang, J. Kuo, S. C. Bae, and S. Granick, Nat. Mater. **11**, 481 (2012).

[19] A. V. Chechkin, F. Seno, R. Metzler, and I. M. Sokolov, Phys. Rev. X **7**, 021002 (2017).

[20] T. Nagai, S. Tsurumaki, R. Urano, K. Fujimoto, W. Shinoda, and S. Okazaki, J. Chem. Theory Comput. **16**, 7239 (2020).

[21] S. Hapca, J. W. Crawford, and I. M. Young, J. R. Soc. Interface. **6**, 111 (2009).

[22] H Faxen, Ark. Mat., Astron. Fys **18**, 29 (1924).

[23] M. Matse, M. V. Chubynsky, and J. Bechhoefer, Phys. Rev. E **96** (2017), 10.1103/PhysRevE.96.042604, arXiv:1706.02039.

[24] F. Weik, R. Weeber, K. Szuttor, K. Breitsprecher, J. de Graaf, M. Kuron, J. Landsgesell, H. Menke, D. Sean, and C. Holm, Eur. Phys. J. Spec. Top. **227**, 1789 (2019).

[25] L. P. Fischer, T. Peter, C. Holm, and J. de Graaf, J. Chem. Phys. **143**, 084107 (2015), arXiv:1503.02671.

[26] J. de Graaf, T. Peter, L. P. Fischer, and C. Holm, J. Chem. Phys. **143**, 084108 (2015), arXiv:1503.02681.

[27] J. D. Weeks, D. Chandler, and H. C. Andersen, J. Chem. Phys. **54**, 5237 (1971).

[28] M. V. Chubynsky and G. W. Slater, Phys. Rev. Lett. **113** (2014), 10.1103/PhysRevLett.113.098302.

[29] M. J. Saxton, Biophys. J. **66**, 394 (1994).

[30] G. W. Slater and H. L. Guo, Electrophoresis **17**, 977 (1996).

[31] G. W. Slater and H. L. Guo, Electrophoresis **17**, 1407 (1996).

References

[1] Chenyu Wen and Shi-Li Zhang. *J. Phys. D : Appl. Phys.*, 54(2) :023001, January 2021.

[2] Liang Xue, Hirohito Yamazaki, Ren Ren, Meni Wanunu, Aleksandar P. Ivanov, and Joshua B. Edel. *Nat. Rev. Mater.*, 5(12) :931–951, December 2020.

[3] Lucile Reynaud, Aurélie Bouchet-Spinelli, Camille Raillon, and Arnaud Buhot. *Sensors*, 20(16) :4495, August 2020.

[4] Mirza Jawad Ul Hasnain. *PAB*, 9(1) :154–161, March 2020.

[5] Yusuke Goto, Rena Akahori, Itaru Yanagi, and Ken-ichi Takeda. *J. Hum. Genet.*, 65(1) :69–77, January 2020.

[6] Anuj Nehra, Sweeti Ahlawat, and Krishna Pal Singh. *Sens. Actuators B Chem.*, 284 :595–622, April 2019.

[7] Nitinun Varongchayakul, Jiaxi Song, Amit Meller, and Mark W. Grinstaff. *Chem. Soc. Rev.*, 47(23) :8512–8524, July 2018.

[8] Pradeep Waduge, Rui Hu, Prasad Bandarkar, Hirohito Yamazaki, Benjamin Cressiot, Qing Zhao, Paul C. Whitford, and Meni Wanunu. *ACS Nano*, May 2017.

[9] Meni Wanunu. *Phys. Life Rev.*, 9(2) :125–158, June 2012.

[10] David Deamer, Mark Akeson, and Daniel Branton. *Nat. Biotechnol.*, 34(5) :518–524, May 2016.

[11] John J. Kasianowicz, Eric Brandin, Daniel Branton, and David W. Deamer. *Proc. Natl. Acad. Sci. USA*, 93(24) :13770–13773, November 1996.

[12] Mark Akeson, Daniel Branton, John J. Kasianowicz, Eric Brandin, and David W. Deamer. *Biophysical Journal*, 77(6) :3227–3233, December 1999.

[13] A. Meller, L. Nivon, E. Brandin, J. Golovchenko, and D. Branton. *Proceedings of the National Academy of Sciences*, 97(3) :1079–1084, February 2000.

[14] Amit Meller, Lucas Nivon, and Daniel Branton. *Phys. Rev. Lett.*, 86(15) :3435–3438, April 2001.

[15] N. Ashkenasy, J. Sánchez-Quesada, M. R. Ghadiri, and H. Bayley. *Angew. Chem., Int. Ed. Engl.*, 44(9) :1401–1404, February 2005.

[16] Elizabeth A Manrao, Ian M Derrington, Andrew H Laszlo, Kyle W Langford, Matthew K Hopper, Nathaniel Gillgren, Mikhail Pavlenok, Michael Niederweis, and Jens H Gundlach. *Nat Biotechnol*, 30(4) :349–353, April 2012.

[17] Zhishan Yuan, Youming Liu, Min Dai, Xin Yi, and Chengyong Wang. *Nanoscale Res Lett*, 15(1) :80, December 2020.

[18] Benjamin N. Miles, Aleksandar P. Ivanov, Kerry A. Wilson, Fatma Doğan, Deanpen Japrung, and Joshua B. Edel. *Chem. Soc. Rev.*, 42(1) :15–28, 2013.

[19] Farzin Haque, Jinghong Li, Hai-Chen Wu, Xing-Jie Liang, and Peixuan Guo. *Nano Today*, 8(1) :56–74, February 2013.

[20] Murugappan Muthukumar. Taylor & Francis, Boca Raton, 2011.

[21] Vladimir V. Palyulin, Tapio Ala-Nissila, and Ralf Metzler. *Soft Matter*, 10(45) :9016–9037, 2014.

[22] Sahin Buyukdagli, Jalal Sarabadani, and Tapio Ala-Nissila. *Polymers*, 11(1) :118, January 2019.

[23] Takahiro Sakaue. *Phys. Rev. E*, 76(2) :021803, August 2007.

[24] Takahiro Sakaue. *Phys. Rev. E*, 81(4) :041808, April 2010.

[25] Jalal Sarabadani, Timo Ikonen, Harri Mökkönen, Tapio Ala-Nissila, Spencer Carson, and Meni Wanunu. *Sci. Rep.*, 7(1) :7423, December 2017.

[26] T. Ikonen, A. Bhattacharya, T. Ala-Nissila, and W. Sung. *Phys. Rev. E*, 85(5), May 2012.

[27] Marc Gershow and J. A. Golovchenko. *Nature Nanotechnology*, 2(12) :775–779, December 2007.

[28] Sarah E. Henrickson, Martin Misakian, Baldwin Robertson, and John J. Kasianowicz. *Phys. Rev. Lett.*, 85(14) :3057–3060, 2000.

[29] Jonathan Nakane, Mark Akeson, and Andre Marziali. *Electrophoresis*, 23(16) :2592–2601, August 2002.

[30] Howard C. Berg. Princeton University Press, Princeton, September 1993.

[31] Peng Chen, Jiajun Gu, Eric Brandin, Young-Rok Kim, Qiao Wang, and Daniel Branton. *Nano Lett.*, 4(11) :2293–2298, November 2004.

[32] C. T. A. Wong and M. Muthukumar. *J. Chem. Phys.*, 126(16) :164903, April 2007.

[33] Tom Chou. *The Journal of Chemical Physics*, 131(3) :034703, July 2009.

[34] Meni Wanunu, Will Morrison, Yitzhak Rabin, Alexander Y. Grosberg, and Amit Meller. *Nat. Nanotechnol.*, 5(2) :160–165, February 2010.

[35] M. Muthukumar. *J. Chem. Phys.*, 132(19) :195101, May 2010.

[36] Alexander Y. Grosberg and Yitzhak Rabin. *J. Chem. Phys.*, 133(16) :165102, October 2010.

[37] Martin Charron, Kyle Briggs, Simon King, Matthew Waugh, and Vincent Tabard-Cossa. *Anal. Chem.*, 91(19) :12228–12237, October 2019.

[38] Payam Rowghanian and Alexander Y. Grosberg. *Phys. Rev. E*, 87(4) :042723, April 2013.

[39] Byoung-jin Jeon and Murugappan Muthukumar. *Macromolecules*, 49(23) :9132–9138, December 2016.

[40] Sahin Buyukdagli and T. Ala-Nissila. *J. Chem. Phys.*, 147(11) :114904, September 2017.

[41] Payam Rowghanian and Alexander Y. Grosberg. *Phys. Rev. E*, 87(4) :042722, April 2013.

[42] Byoung-jin Jeon and Murugappan Muthukumar. *J. Chem. Phys.*, 140(1) :015101, January 2014.

[43] Marius M. Hatlo, Debabrata Panja, and René van Roij. *Phys. Rev. Lett.*, 107(6) :068101, August 2011.

[44] Sahin Buyukdagli. *Soft Matter*, 14(18) :3541–3549, 2018.

[45] Yin Zhang, Jiabin Zhao, Wei Si, Yajing Kan, Zheng Xu, Jingjie Sha, and Yunfei Chen. *Small Methods*, page 1900893, April 2020.

[46] Mauro Chinappi, Misa Yamaji, Ryuji Kawano, and Fabio Cecconi. *ACS Nano*, page acsnano.0c06981, November 2020.

[47] Stefanos K. Nomidis, Jef Hooyberghs, Giovanni Maglia, and Enrico Carlon. *J. Phys. : Condens. Matter*, 30(30) :304001, June 2018.

[48] Farnoush Farahpour, Azadeh Maleknejad, Fathollah Varnik, and Mohammad Reza Ejtehadi. *Soft Matter*, 9(9) :2750, 2013.

[49] Stefan W. Kowalczyk, Alexander Y. Grosberg, Yitzhak Rabin, and Cees Dekker. *Nanotechnology*, 22(31) :315101, 2011.

[50] Sarah C. Vollmer and Hendrick W. de Haan. *J. Chem. Phys.*, 145(15) :154902, October 2016.

[51] J. Rudnick and G. Gaspari. *Science*, 237(4813) :384–389, July 1987.

[52] Iwao Teraoka. Wiley, New York, 2010.

[53] Paul J. Flory. Cornell University Press, 1953.

[54] Masao Doi and Samuel F. Edwards. Number 73 in International Series of Monographs on Physics. Clarendon Press, Oxford, reprinted edition, 2007.

[55] N. G. van Kampen. North-Holland Personal Library. Elsevier, Amsterdam, Boston, 3rd ed edition, 2007.

[56] William T. Coffey, Yuri P. Kalmykov, and John T. Waldron. Number 14 in World Scientific Series in Contemporary Chemical Physics. World Scientific, Hackensack, NJ, 2. ed., reprinted edition, 2005.

[57] Brian J. Kirby. Cambridge University Press, July 2010.

[58] Jean-Louis Viovy. *Reviews of Modern Physics*, 72(3) :813–872, July 2000.

[59] Ronald F Probstein. Wiley-Interscience, Hoboken, N.J., 2003.

[60] Gary W. Slater, Christian Holm, Mykyta V. Chubynsky, Hendrick W. de Haan, Antoine Dubé, Kai Grass, Owen A. Hickey, Christine Kingsburry, David Sean, Tyler N. Shendruk, and Lixin Zhan. *Electrophoresis*, 30(5) :792–818, March 2009.

[61] Michel G. Gauthier and Gary W. Slater. *Phys. Rev. E*, 70(1) :015103, July 2004.

[62] Mykyta V. Chubynsky and Gary W. Slater. *Phys. Rev. E*, 85(1) :016709, January 2012.

[63] Sylvain Hubert. Thesis, University of Ottawa (Canada), 2004.

[64] Florian Weik, Rudolf Weeber, Kai Szuttor, Konrad Breitsprecher, Joost de Graaf, Michael Kuron, Jonas Landsgesell, Henri Menke, David Sean, and Christian Holm. *Eur. Phys. J. Spec. Top.*, 227(14) :1789–1816, March 2019.

[65] John D. Weeks, David Chandler, and Hans C. Andersen. *J. Chem. Phys.*, 54(12) :5237–5247, June 1971.

[66] David Sean-Fortin. Thesis, Université d'Ottawa / University of Ottawa, 2017.

[67] Burkhard Duenweg and Anthony J. C. Ladd. *arXiv :0803.2826 [cond-mat]*, pages 89–166, 2009.

[68] Apratim Chatterji and Juergen Horbach. *J. Chem. Phys.*, 122(18) :184903, May 2005.

[69] Burkhard Dünweg, Ulf D. Schiller, and Anthony J. C. Ladd. *Phys. Rev. E*, 76(3) :036704, September 2007.

[70] Patrick Ahlrichs and Burkhard Dünweg. *J. Chem. Phys.*, 111(17) :8225–8239, November 1999.

[71] Markus Deserno and Christian Holm. *J. Chem. Phys.*, 109(18) :7694–7701, November 1998.

[72] Markus Deserno and Christian Holm. *J. Chem. Phys.*, 109(18) :7678–7693, November 1998.